

Wilfrid Laurier University

Scholars Commons @ Laurier

Theses and Dissertations (Comprehensive)

2019

Heterogeneous Chemistry of Iron at the Liquid/Solid and Air/Solid Interfaces

Mohammad Aminur Rahman

Wilfrid Laurier University, rahm5560@mylaurier.ca

Follow this and additional works at: <https://scholars.wlu.ca/etd>

Recommended Citation

Rahman, Mohammad Aminur, "Heterogeneous Chemistry of Iron at the Liquid/Solid and Air/Solid Interfaces" (2019). *Theses and Dissertations (Comprehensive)*. 2200.

<https://scholars.wlu.ca/etd/2200>

This Dissertation is brought to you for free and open access by Scholars Commons @ Laurier. It has been accepted for inclusion in Theses and Dissertations (Comprehensive) by an authorized administrator of Scholars Commons @ Laurier. For more information, please contact scholarscommons@wlu.ca.

Heterogeneous Chemistry of Iron at the Liquid/Solid
and Air/Solid Interfaces

by

Mohammad Aminur Rahman

Bachelor of Science, Honors in Chemistry, Jahangirnagar University, 2004

Master of Science, Chemistry, Memorial University of NL, 2014

DISSERTATION

Submitted to the Biological and Chemical Sciences Program

Faculty of Science

In partial fulfilment of the requirements for the
Doctor of Philosophy in Biological and Chemical Sciences

Wilfrid Laurier University

2019

Mohammad Aminur Rahman 2019 ©

Abstract

Hematite (α -Fe₂O₃) is one of the common and stable phases of iron oxide that is ubiquitous in nature. It is involved in many heterogeneous reactions through liquid-solid and gas-solid interfacial interactions in aquatic geochemical systems. Moreover, the interfacial chemistry of metal-oxide and organic matter plays a significant role in the mobility and bioavailability of iron and other components such as arsenic in the soil and aquatic systems. The interactions of organic matter with metal oxide surfaces occur through several mechanisms in aquatic environment. Chapter 2 of this thesis describes the interactions of low molecular weight model organics that include citric acid (CA), oxalic acid (OA) and pyrocatechol (PC) on hematite nanoparticles that have been investigated and characterized by *in situ* attenuated total internal reflectance Fourier transform infrared spectroscopy (ATR-FTIR) measurements. H₂O/D₂O (H/D) exchange experiments were performed to observe the effect of hydration. It was found that strong hydration influenced the spectra for both CA and OA whereas less in the case of PC. Chapter 3 illustrates the initial binding kinetics of arsenicals such as dimethyl arsenate (DMA) onto hematite nanoparticles pre-exposed to low molecular weight organics such as OA and PC. These kinetic experiments were conducted using ATR-FTIR with an emphasis on the role that electrolytes (KCl, NaCl, and KBr) play in the adsorption process. It was concluded that the rate of adsorption for the arsenical onto pre-exposed model organic-hematite surface was found greater in the presence of electrolytes, based on the initial kinetic rate of adsorption for arsenical. Chapter 4 focuses on the investigation of the hygroscopic properties of organic and organometallic polymeric particles, namely polycatechol, polyguaiacol, Fe-polyfumarte, and Fe-polymuconate. These particles are efficiently formed in iron-catalyzed reactions with aromatic and aliphatic dicarboxylic acid compounds detected in field-collected Secondary Organic Aerosol (SOA). The structure of surface water was studied using diffuse reflectance infrared Fourier transform spectroscopy (DRIFTS), and the uptake of

gas water was quantified using quartz crystal microbalance (QCM) as a function of relative humidity. Spectroscopic data show that water bonding with organic functional groups acting as hydrogen bond acceptors causes shifts in their vibrational modes. Analysis of the hydroxyl group stretching region revealed weak and strong hydrogen bonding networks that suggest cluster formation reflecting water-water and water-organics interactions, respectively. A modified Type II multilayer Brunauer-Emmett-Teller (BET) adsorption model described the adsorption isotherm on the nonporous materials, polycatechol, polyguaiacol, and Fe-polymuconate. However, water adsorption on porous Fe-polyfumarate was best described using a Type V adsorption model, namely the Langmuir-Sips model that accounts for condensation in pores. It was found that the organic polymers are more hydrophobic than the Fe-containing organometallic polymers. In Chapter 5, the efficiency of iron-containing materials such as Fe-BTC (BTC = 1,3,5-benzenetricarboxylate) metal-organic frameworks (MOFs) and CoFe₂O₄ nanomaterials were examined to explore their performance in reducing NO_x in NH₃-SCR (Selective Catalytic Reduction) by DRIFTS. Urea was used as an *in situ* production of NH₃(g) as a reductant agent for NO(g). It appeared that the rate of conversion of NO(g) in the presence of CoFe₂O₄ nanomaterials (2.3±0.03 ppm·meter⁻²·min⁻¹) is better than that of Fe-BTC MOFs (0.22±0.04 ppm·meter⁻²·min⁻¹).

Declaration of Co-authorship

Chapter 2

This chapter contains my contribution to the paper that was published in *Environmental Science: Nano*, by Royal Society of Chemistry (RSC) and can be found online at the following link:

<https://pubs.rsc.org/en/content/articlelanding/2016/en/c6en00132g#!divAbstract>.

DOI:10.1039/C6EN00132G

Spectral Characterization and Surface Complexation Modeling of Organics on Hematite Nanoparticles: Role of Electrolytes in the Binding Mechanism. Situm, A.; Rahman, M. A. and Al-Abadleh, H. A. *Environmental Science: Nano*, **2016**, *3*, 910-926. I am the second author of this paper and contributed through running experiments, analyzing data and writing.

Chapter 3

This chapter describes my contribution to the paper that was published in the *Journal of Physical Chemistry A*, by American Chemical Society (ACS) and can be found online at the following link:

<https://pubs.acs.org/doi/abs/10.1021/acs.jpca.7b03426>.

DOI: 10.1021/acs.jpca.7b03426

ATR-FTIR and Flow Microcalorimetry Studies on the Initial Binding Kinetics of Arsenicals at the Organic-Hematite Interface. Situm, A.; Rahman, M. A.; Allen, N.; Kabengi, N. and Al-Abadleh, H. A. *Journal of Physical Chemistry A*, **2017**, *121*, 5569-5579. I am the second author of this paper and contributed through running experiments, analyzing data and writing.

Chapter 4

This chapter has been reproduced from entire paper that was published in *ACS Omega*, by American Chemical Society (ACS) and can be found online at the following link:

<https://pubs.acs.org/doi/10.1021/acsomega.8b02066>

DOI: 10.1021/acsomega.8b02066

Surface Water Structure and Hygroscopic Properties from Gas Phase Water Uptake on Light Absorbing Secondary Organic Polymers of Atmospheric Relevance. Rahman, M. A. and Al-Abadleh, H. A. *ACS Omega*, **2018**, 3, 15519-15529. I am the first author of this paper and contributed through running experiments, analyzing data and writing.

Acknowledgements

I would like to express my heartiest thanks to Dr. Hind A. Al-Abadleh, my supervisor for giving me the opportunity to join her research group and for her constant guidance, supervision, encouragements and thoughtful input provided throughout the duration of this research work.

I would like to thank Dr. Vladimir Kitaev and Dr. Scott Smith, for being my committee member and for all their guidance, direction and advice with regards to all aspects of my research.

Thanks to all the group members from the Dr. Al-Abadleh's lab for their help and cooperation. Special thanks to Arthur Situm, for his time spent in introducing me with the lab experiments and other related activities. Thanks to Sabur for his valuable suggestions every now and then during my entire program. I would also like to thank Sara, Antony, and Aseel for their support.

I would like to thank the Graduate and Postdoctoral Studies and Department of Chemistry and Biochemistry, Wilfrid Laurier University, for their financial support. Also, thanks to Ontario Government for OGS scholarship and MS2Discovery for the financial award.

I want to express my heartiest thanks to my wife, Lubna for her encouragement, patience and care she has shown during the course of my study. I am also grateful to my family members specially, to my parents and mother-in-law for their moral support during my study. I would like to express deepest gratitude to my sisters, sister-in-law, brothers-in-law and all the family members for their inspiration, support and encouragement throughout my whole journey.

Finally, thanks to Allah for his blessing.

Table of Contents

	Page No
List of Tables	xi
List of Figures and Illustrations.....	xii
List of Abbreviations.....	xx
Chapter 1 General Introduction	
1.1 Introduction.....	1
1.2 Iron in soil and water.....	2
1.3 Iron in the atmosphere.....	4
1.4 Iron as a remedial material in heterogeneous catalysis.....	6
1.5 Surface Sensitive Techniques	8
1.6 Research questions and objectives.....	10
1.7 Thesis organization.....	11
1.8 References.....	14
Chapter 2 Spectral Characterization of Surface Organics on Hematite Nanoparticles, H/D Exchange Experiments	
2.1 Abstract.....	19
2.2 Introduction.....	19
2.3 Objectives.....	25
2.4 Experimental.....	25
2.3.1 Chemicals.....	25
2.3.2 Electrode preparation and calibration of pD meter.....	26
2.3.3 Preparation of film on ZnSe ATR crystal.....	27
2.3.4 ATR-FTIR spectroscopy experiments.....	28
2.3.5 H/D exchange experiments.....	28

2.5 Results and discussion.....	29
2.5.1 Spectral characterization of surface organics as a function of pD.....	29
2.6 Conclusions.....	34
2.7 References.....	34
Chapter 3 ATR-FTIR Studies on the Initial Binding Kinetics of Arsenicals at the Organic-Hematite Interface	
3.1 Abstract.....	37
3.2 Introduction.....	37
3.3 Objectives.....	44
3.4 Experimental.....	46
3.4.1 Chemicals.....	46
3.4.2 Preparation of film on ZnSe ATR crystal.....	46
3.4.3 ATR-FTIR spectroscopy experiments.....	46
3.4.4 Adsorption kinetics.....	47
3.4.5 Kinetic modeling (Adsorption).....	47
3.4.6 Desorption kinetics.....	49
3.4.7 Kinetic modeling (Desorption).....	49
3.5 Results and discussion.....	50
3.5.1 Adsorption kinetics.....	50
(a) Adsorption kinetics of model organics on hematite nanoparticle.....	50
(b) Adsorption kinetics of arsenicals on hematite nanoparticle.....	57
(c) Adsorption of arsenicals on hematite containing model organics.....	60
3.5.2 Desorption Kinetics of model organic matter on hematite.....	63

3.6 Conclusions.....	65
3.7 References.....	66
Chapter 4 Surface Water Structure and Hygroscopic Properties of Light Absorbing Secondary Organic Polymers of Atmospheric Relevance	
4.1 Abstract.....	71
4.2 Introduction.....	72
4.3 Objectives.....	74
4.4 Experimental.....	74
4.4.1 DRIFT experiments.....	76
4.4.2 QCM experiments.....	77
4.5 Results and discussion	78
4.5.1 Structure of surface water on polycatechol and polyguaiacol.....	78
4.5.2 Structure of surface water on Fe-polyfumarate and Fe-polymuconate.....	85
4.5.3 Adsorption thermodynamics.....	88
4.6 Conclusions.....	95
4.7 References.....	97
Chapter 5 Iron-containing Metal-Organic Frameworks (MOFs) in Enhancing the Selective Catalytic Reduction (SCR) of NO _x to Nitrogen Gas	
5.1 Abstract.....	105
5.2 Introduction.....	105
5.3 Objectives.....	112
5.4 Experimental.....	112
5.4.1 Chemicals.....	112
5.4.2 DRIFTS experiments.....	113

5.5 Results and discussion.....	115
5.5.1 <i>In situ</i> production of ammonia (NH ₃) from urea (NH ₂ CONH ₂).....	115
5.5.2 Thermal decomposition of Fe-BTC under dry conditions.....	118
5.5.3 Thermal decomposition of Fe-BTC/8%urea mixture under dry conditions.....	119
5.5.4 Thermal decomposition of Fe-BTC/8%urea mixture under humid conditions.....	121
5.5.5 Reaction of NO with either Fe-BTC or 8%urea under dry conditions.....	122
5.5.6 Reaction of NO with Fe-BTC/8%urea mixture under dry conditions.....	125
5.5.7 Reaction of NO with Fe-BTC/8%urea mixture under humid conditions.....	126
5.5.8 Reaction of NO with CoFe ₂ O ₄ under dry conditions.	127
5.5.9 Reaction of NO with CoFe ₂ O ₄ /8%urea mixture under dry conditions.....	128
5.6 Conclusions.....	130
5.7 References.....	130
Chapter 6 Conclusions and Significance.....	135
Appendix 1 Data analysis using Macros and OMNIC Software.....	139
Appendix 2 Procedure for BET instrument.....	147
Appendix 3 United State Environmental Protection Agency data Base (EPA).....	158

List of Tables

	Page No
Table 2.1 Amount of buffer powder in each capsule.....	27
Table 2.2 Amount of buffer power taken for preparation of buffer solution.....	27
Table 3.1 Types of arsenic compounds.....	38
Table 3.2 Linearized first order observed adsorption rates (min^{-1}) at various ionic strength conditions of model organics (oxalate and pyrocatechol) on hematite film.....	56
Table 3.3 DMA initial adsorption rate on different surfaces, with and without electrolytes at pH 7 at 2 mL/min flow rate.....	62
Table 4.1 Assignment of features observed in the DRIFTS normalized difference absorbance spectra during gas phase water adsorption on organic polymers/diamond samples.....	82
Table 4.2 Best Fit Parameters for Gas Phase Water Adsorption on Polymeric Organic Films at 298 K Shown in Figure 4.9a...	92
Table 5.1 Properties of Fe-BTC.....	111
Table 6.1 Molar absorptivity obtained for NO, NO ₂ , N ₂ O, NH ₃ and HNCO from EPA database.....	159

List of Figure and Illustrations

		Page No
Figure 1.1	Structure of (a) hematite and (b) magnetite.....	1
Figure 1.2	Pictorial presentation of environmental processes (both natural and anthropogenic sources of gases and particles in the atmosphere and their consequence) that occurs on the earth.....	5
Figure 1.3	Organic linkers and metal ions or cluster combine to synthesize metal-organic framework materials.....	7
Figure 1.4	Surface sensitive techniques normally used to study environmental interfaces.....	8
Figure 2.1	Mechanisms for the interaction of organics with metal oxide or mineral surfaces.....	20
Figure 2.2	Outer-sphere and inner-sphere complexes for citrate with goethite.....	23
Figure 2.3	Citrate complexes on goethite surface (Outer-sphere and inner-sphere)	23
Figure 2.4	ATR-FTIR absorption spectra of adsorbed citrate on hematite nanoparticles after flowing 10^{-4} M solutions prepared in D_2O after 10 min flow as a function of decreasing pD from 8 to 4. The electrolyte concentration was 0.01 M KCl.....	29
Figure 2.5	Possible structures for the surface complexation of citrate (CA) (out-sphere and inner-sphere) onto hematite nanoparticles. Arrow shows the direction of decreasing pH or pD and the corresponding surface complexes under acidic (right) versus basic (left) conditions.....	30
Figure 2.6	ATR-FTIR absorption spectra of adsorbed oxalate on hematite nanoparticles after flowing 10^{-4} M solutions prepared in D_2O after 10 min flow as a function of decreasing pD from 8 to 4. The electrolyte concentration was 0.01 M KCl.....	31
Figure 2.7	Possible structures for the surface complexation of oxalate (OA) (out-sphere and inner-sphere) onto hematite nanoparticles. Arrow shows the direction of decreasing pH	32

	or pD and the corresponding surface complexes under acidic (right) versus basic (left) conditions.....	
Figure 2.8	ATR-FTIR absorption spectra of adsorbed pyrocatechol on hematite nanoparticles after flowing 10^{-4} M solutions prepared in D_2O after 10 min flow as a function of decreasing pD from 9 to 6. The electrolyte concentration was 0.01 M KCl.....	33
Figure 2.9	Possible structures for the surface complexation of pyrocatechol (PC) (inner-sphere) onto hematite nanoparticles. Arrow shows the direction of decreasing pH or pD and the corresponding surface complexes under acidic (right) versus basic (left) conditions.....	33
Figure 3.1	Flow diagram of As in the global cycle.....	39
Figure 3.2	The Challenger pathway for biomethylation, followed by sequential reduction and oxidative methylation of arsenic.	40
Figure 3.3	Influence of dissolved natural organic matter (DOM) on oxidation and hydrolysis of contaminants by mineral surfaces.....	41
Figure 3.4	Hypothetical molecular structure of humic acid, showing important functional groups.....	42
Figure 3.5	Schematic diagram of arsenicals (arsenate or DMA) adsorption onto hematite nano particles pre-exposed to model organics citrate (CA), oxalate (OA) and pyrocatechol (PC).....	44
Figure 3.6	Absorbance spectra of oxalate (1.0 mM) onto a clean hematite (6 mg) film at pH 7, I = 10 mM (a) NaCl (b) KCl (c) KBr and (d) H_2O at room temperature. ATR-FTIR absorbance spectra of adsorbed oxalate were collected as a function of time.....	51
Figure 3.7	Adsorption kinetic curves generated from the baseline-corrected ATR-FTIR absorbances for oxalate adsorbed on to a clean hematite (6 mg) film at pH 7 with H_2O and three different electrolytes (I = 10 mM for KCl, NaCl and KBr) and a 2 mL/min flow rate at room temperature.....	52
Figure 3.8	Linearized adsorption kinetics curves of oxalate on 6 mg hematite film with at pH 7 with H_2O and three different electrolytes (I = 10 mM for KCl, NaCl and KBr). $\ln(1-$	52

	Abs(Org)/Abs(OrgMax) with Abs(Org) corresponding the band measured for oxalate.....	
Figure 3.9	Adsorption kinetic curves (left) generated from the baseline-corrected ATR-FTIR absorbances for oxalate adsorbed on to a clean hematite (6 mg) film at pH 7, I = 10 mM NaCl, and a 2 mL/min flow rate at room temperature. Linearized adsorption kinetic curve of oxalate (right).....	53
Figure 3.10	Adsorption of pyrocatechol (1.0 mM) onto a clean hematite (6 mg) film at pH 7, I = 10 mM H ₂ O (left) and KCl (right) at room temperature. ATR-FTIR absorbance spectra of adsorbed oxalate were collected as a function of time.....	54
Figure 3.11	Adsorption kinetic curves generated from the baseline-corrected ATR-FTIR absorbances for pyrocatechol adsorbed on to a clean hematite (6 mg) film at pH 7 with a 2 mL/min flow rate at room temperature.....	55
Figure 3.12	Linearized adsorption kinetics of pyrocatechol on 6 mg hematite film with at pH 7. $\ln(1-\text{Abs}(\text{Org})/\text{Abs}(\text{OrgMax}))$ with Abs(Org) corresponding the band measured for pyrocatechol.....	55
Figure 3.13	ATR-FTIR absorbance spectra of 1.0 mM DMA on to a clean, hematite (6 mg) film at pH 7, I = 10 mM (a) NaCl (b) KBr and (c) H ₂ O with a 2 mL/min flow rate at room temperature.....	57
Figure 3.14	Baseline-corrected adsorption kinetics of 1.0 mM DMA onto to a clean, hematite (6 mg) film at pH 7 with a 2 mL/min flow rate at room temperature.....	58
Figure 3.15	Linearized adsorption kinetics of DMA on 6 mg hematite film with at pH 7. $\ln(1-\text{Abs}(\text{As})/\text{Abs}(\text{AsMax}))$ with Abs(As) corresponding the band measured for DMA.....	58
Figure 3.16	Baseline-corrected adsorption kinetics of 1.0 mM DMA onto to a clean, hematite (6 mg) film at pH 7 with a 2 mL/min flow rate at room temperature. Data points represent the average of two experiments.....	59
Figure 3.17	Linearized adsorption kinetics of 1.0 mM DMA on 6 mg hematite film with at pH 7 in NaCl (0.01 M). $\ln(1-\text{Abs}(\text{As}))$	59

	/Abs(AsMax) with Abs(As) corresponding the band measured for DMA.....	
Figure 3.18	ATR-FTIR absorbance spectra of 1.0 mM DMA on to hematite (6 mg) film pre-exposed to oxalate at pH 7, I = 10 Mm (a) NaCl (b) KBr and (c) H ₂ O and (d) 1.0 mM PC onto hematite in KCl solution with a 2 mL/min flow rate at room temperature.....	60
Figure 3.19	Kinetic curve of 1.0 mM DMA on to hematite (6 mg) film pre-exposed to OA at pH 7, I = 10 Mm (a) NaCl (b) KBr and (c) H ₂ O with a 2 mL/min flow rate at room temperature.....	61
Figure 3.20	Linearized adsorption kinetics of 1.0 mM DMA on 6 mg hematite film with at pH 7. $\ln(1-Abs(As)/Abs(AsMax))$ with Abs(As) corresponding the band measured for DMA.....	62
Figure 3.21	ATR-FTIR absorbance spectra correspond to the oxalate desorption from hematite (6 mg) film at pH 7 in 10 mM (a) NaCl (b) KBr and (c) H ₂ O at room temperature, by the flowing of 1.0 mM DMA.....	63
Figure 3.22	Desorption kinetic curve generated from the baseline-corrected ATR-FTIR absorbances of oxalate from hematite (6 mg) nanoparticles at pH 7 in H ₂ O and a 2 mL/min flow rate at room temperature, by 1.0 mM DMA.....	64
Figure 3.23	Linearized desorption kinetic curve for oxalate on the hematite film at pH 7 in H ₂ O. The figure shows $\ln(A(organic)/Amax(Organic))$ with A(Organic) corresponds to absorbance at 1658 cm ⁻¹ for oxalate.....	65
Figure 4.1	Represents the interactions of H ₂ O molecules with model organic and organometallic particles.....	74
Figure 4.2	Representative DRIFTS absorbance spectra of solid organic polymers mixed with diamond powder after overnight drying at a flow of dry air: (a) 2% wt/wt polycatechol, (b) 2% wt/wt polyguaiacol, (c) 6% wt/wt Fe-polyfumurate, and (d) 7% wt/wt Fe-polymuconate. A spectrum of dry diamond powder only was used as the reference to generate these absorbance spectra. See reference 46 in main manuscript for assignment.....	79
Figure 4.3	Selected DRIFTS absorbance spectra of surface water collected as a function of increasing % RH on (a) polycatechol and (b) polyguaiacol (solid lines) in ca. 2% w/w	81

organic material/diamond powder. The dotted lines are control spectra collected on diamond particles only (no organic material) at the same % RH values. Data in (c,d) show the difference in normalized absorbance spectra as a function of RH obtained by subtracting the normalized diamond spectrum from that collected with organic materials at each % RH with a factor 1. The normalization of all spectra was done relative to the peak at 3421 cm⁻¹. The “*” denotes residual features observed only in the control spectra.....

- Figure 4.4 Selected DRIFTS absorbance spectra of surface water collected as a function of increasing % RH on a 2% w/w polyguaiacol/diamond sample. The solid lines are spectra collected using gas phase D₂O. The dotted lines are the same spectra shown in Figure 4.3b collected using gas phase H₂O at 5.5, 25, 41, and 86% RH..... 83
- Figure 4.5 Selected DRIFTS absorbance spectra of surface water collected as a function of increasing %RH on a 2% wt/wt polyguaiacol/diamond sample. The solid lines are spectra collected using gas phase D₂O. The dashed lines are the same spectra shown in Figure 1b collected using gas phase H₂O at 5.5, 25, 41 and 86% RH. The “*” donates incomplete subtraction of gas phase water lines..... 84
- Figure 4.6 Selected DRIFTS absorbance spectra of surface water collected as a function of increasing % RH on (a) Fe-polyfumarate and (b) Fe-polymuconate (solid lines) in ca. 7% w/w organic material/diamond particles. The dotted lines are control spectra collected on diamond particles only (no organic material) at the same % RH values. Data in (c,d) show the difference in normalized absorbance spectra as a function of RH obtained by subtracting the normalized diamond spectrum from that collected with organic materials at each RH with a factor of 1. The normalization of all spectra was done relative to the peak at 3421 cm⁻¹. The “*” denotes residual features observed only in the control spectra..... 86
- Figure 4.7 Raw QCM data showing change in frequency, ΔF, as a function of increasing relative humidity (%RH, numbers between vertical dashed lines) relative to signal recorded while flowing dry air on (a) polycatechol (0.3 mg), and (b) polyguaiacol (0.1 mg) thin films. Photos to the right show representative samples prior to starting the water uptake experiments..... 89

Figure 4.8	Raw QCM data showing change in frequency, ΔF , as a function of increasing relative humidity (%RH, numbers between vertical dashed lines) relative to signal recorded while flowing dry air on (a) Fe-polyfumarate (0.037 mg), and (b) Fe-polymuconate (0.11 mg) thin films. Photos to the right show representative samples prior to starting the water uptake experiments.....	90
Figure 4.9	Water adsorption isotherms at 298 K constructed from the data shown in Figures 4.7 and 4.8 for (a) polycatechol (0.3 mg), (b) polyguaiacol (0.1 mg), (c) Fe-polyfumarate (0.037 mg), and (d) Fe-polymuconate (0.1 mg) using the equation $\Delta m = -\Delta F/C_f$, where Δm is the change in mass due to adsorbed water (left axis). ΔF was multiplied by the geometrical area of the deposited films. The right axes were calculated by converting Δm to water mass (g) per surface area (m^2) of the organic film deposited. The lines through the data represent least squares best fits to the experimental data. The best fit parameters are listed in Table 4.2. The outermost right axis was obtained by dividing water coverage in gm^{-2} by that at the monolayer coverage obtained from the best-fit parameters. The error bars represent the standard deviation ($\pm\sigma$) from the average data of 3–4 water isotherm experiments, each on a freshly prepared organic film.....	91
Figure 4.10	Adsorption isotherm of N_2 gas on Fe-polyfumarate at 77 °K confirming the porous structure of this organometallic material.....	94
Figure 4.11	High resolution transmission electron microscopy (HR-TEM) images for Fe-polyfumarate showing the pore structure of this material.....	94
Figure 5.1	Mechanism of NO conversion to N_2 on the surface of $Fe_xCo_yCe_zO_m$ supported on activated carbon.....	108
Figure 5.2	The structure of Fe-BTC (carbon atoms gray, oxygen atoms red, and iron atoms light-blue).....	110
Figure 5.3	Structure of $CoFe_2O_4$ ($43 m^2/g$).....	112
Figure 5.4	Experimental setup for DRIFTS experiments. a) for surface species characterization b) for gas phase species characterization.....	113

Figure 5.5	Thermal decomposition of urea only under dry and humid conditions (a) Gas phase spectra as a function of time (t) 8% urea/diamond, dry air, at 115 °C, then with heating to 180 °C. (b) Gas phase spectra as function of time (t) 8% urea/diamond, humid air (%RH 10-12), at 115 °C, then with heating to 180 °C.....	116
Figure 5.6	(a) Kinetic curve of [NH ₃] vs time (min) for data in figure 5.5(a). (b) Kinetic curve of [NH ₃] versus time (min) for data in figure 5.5(b).....	117
Figure 5.7	Thermal decomposition of Fe-BTC only under dry conditions (a) Gas phase spectra as a function of time and temperature, dry condition. (b) DRIFTS spectra of Fe-BTC only as a function of time and temperature-dry (brown) and humid (blue) conditions.....	118
Figure 5.8	Thermal decomposition of Fe-BTC/8%urea mixture under dry conditions and quantification of gas phase products. (a) Gas phase spectra as a function of time (min) and temperature (°C) under dry air. (b) Kinetic curve of [NH ₃] vs time (min) for data in figure 5.8(a).....	120
Figure 5.9	Thermal decomposition of Fe-BTC/8%urea mixture under humid conditions and quantification of gas phase products (a) Gas phase spectra as a function of time (min) and temperature (°C) under humid condition, (%RH 10-12). (b) Kinetic curve of [NH ₃] vs time (min) for data in figure 5.9(a)..	121
Figure 5.10	Reaction of NO with either Fe-BTC or 8%urea under dry conditions. (a) Gas phase spectra of reaction between NO and Fe-BTC only as a function of time (min) and temperature (°C) under dry air. (b) Kinetic curve of [NO] vs time (min) for data in figure 5.10(a). (c) Gas phase spectra of reaction between NO and diamond/8%urea as a function of time (min) and temperature (°C) under dry condition. (d) Kinetic curve of [NO]/[NH ₃]/[HNCO] vs time (min) for data in figure5.10(c).....	123
Figure 5.11	Reaction of NO with Fe-BTC/8%urea mixture under dry conditions. (a) Gas phase spectra of reaction between NO and Fe-BTC/8%urea as a function of time (min) and temperature (°C) under dry air. (b) Kinetic curve of [NO]/[NH ₃]/[HNCO] vs time (min) for data in figure 5.11(a)....	125
Figure 5.12	Reaction of NO with Fe-BTC/8%urea mixture under humid conditions. (a) Gas phase spectra of reaction between NO	126

and Fe-BTC/8%urea as a function of time (min) and temperature (°C) under humid condition (%RH 10-12). (b) Kinetic curve of [NO]/[NH₃] vs time (min) for data in figure 5.12(a).....

Figure 5.13	(a) Gas phase spectra of reaction between NO and CoFe ₂ O ₄ only as a function of time (min) and temperature (°C) under dry air. (b) Kinetic curve of [NO] vs time (min) for data in figure 5.13(a).....	127
Figure 5.14	(a) Gas phase spectra of reaction between NO and CoFe ₂ O ₄ /8%urea as a function of time (min) and temperature (°C) under dry air. (b) Kinetic curve of [NO]/[NH ₃]/[HNCO] vs time (min) for data in figure 5.14(a)...	128
Figure 5.15	Proposed mechanism for the reaction of urea and Fe-BTC/CoFe ₂ O ₄ with NO(g) under dry condition.....	129

List of Abbreviations

ATR-FTIR	Attenuated Total Reflectance Fourier Transform Infrared Spectroscopy
As	Arsenic
ALW	Aerosol Liquid Water
ACF	Actual Carbon Filter
BET	Brunauer-Emmett-Teller
BTC	1,3,5-benzenetricarboxylate
CA	Citric Acid
CCN	Cloud Condensation Nuclei
DMA	Dimethyl Arsiniate
DRIFT	Diffuse Reflectance Infrared Fourier Transform Spectroscopy
HVC	High Vacuum Chamber
HULIS	Humic-Like Substance
H/D	H ₂ O/D ₂ O
ICN	Ice Condensation Nuclei
I	Ionic Strength
MCT	Mercury Cadmium Telluride
MOFs	Metal-Organic Frame Works
MFC	Mass Flow Controller
MFCR	Mass Flow Channel Reader
OA	Oxalic Acid
POA	Primary Organic Aerosol
PC	Pyrocatechol

QCM	Quartz Crystal Microbalance
RH	Relative Humidity
SOA	Secondary Organic Aerosol
SCR	Selective Catalytic Reduction
TC	Thermocouple
VOC	Volatile Organic Carbon
WB	Water Bubbler

Chapter 1 General Introduction

1.1 Introduction

Iron (Fe) is one of the most important elements in our natural environment and plays a significant role in many chemical reactions. It is an indispensable element for entire living forms.¹ It is placed as the 4th most abundant element in the Earth's crust after oxygen, silicon and aluminum. However, the 10th in the universe and the most in building up the earth (34.5% by mass). It is a very reactive transition-metal and exists as two major series of compounds such as the ferrous, containing Fe^{2+} and the ferric, containing iron (III) Fe^{3+} .²

In the natural environment, most of the iron exists in oxide form and is found in four different polymorphs such as FeO , Fe_3O_4 , $\alpha\text{-Fe}_2\text{O}_3$ and $\gamma\text{-Fe}_2\text{O}_3$. However, $\alpha\text{-Fe}_2\text{O}_3$ (hematite) and Fe_3O_4 (magnetite) are known to be the most common and stable forms of iron oxides (Figure 1.1).³ A metastable form of iron oxide, known as maghemite ($\gamma\text{-Fe}_2\text{O}_3$), has a structure similar to rock salt and is unstable below 843 K. These iron oxides have unique biochemical and catalytic properties that are suitable for application in the field of environmental and biomedical sciences.

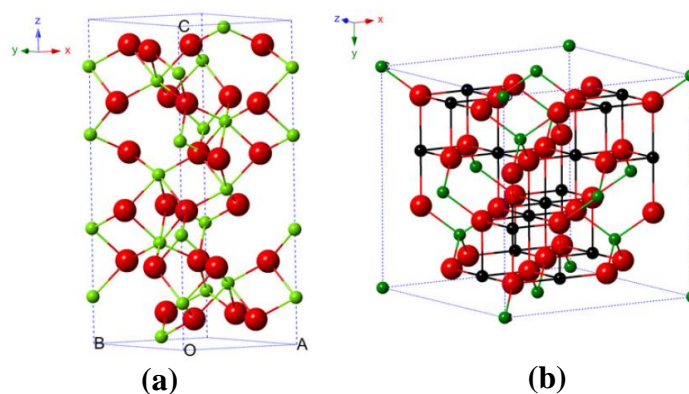


Figure 1.1 Structure of (a) hematite and (b) magnetite. (*re-printed with permission from Ref 3*).

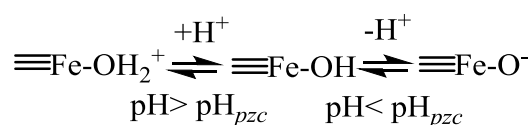
Iron can be also found in oxide hydroxide form. The formation of iron oxide and hydroxide occurs by protonation and release of iron ions from primary or secondary minerals or oxidation.

Ferrihydrite ($5\text{Fe}_2\text{O}_3 \cdot 9\text{H}_2\text{O}$) is a common iron oxide found in soils. It has poorly ordered structure not like crystalline hematite and is considered an amorphous iron hydroxide.⁴

Iron is naturally introduced into the aquatic systems through many processes such as weathering, water-rock interactions, biodegradation of organic matters, atmospheric deposition and volcanic eruption. Anthropogenic addition of iron into surface water and the Earth's atmosphere is also significant.⁵ The presence of iron in mineral dust, rocks and soils emphasizes its involvement in various environmental processes such as heterogeneous atmospheric chemistry, aqueous geochemistry and environmental catalysis and remediation. As detailed below, our goal is to explore the chemistry of iron that is involved at the liquid-solid and gas-solid interface in environmental systems. For liquid-solid interfacial studies, hematite ($\alpha\text{-Fe}_2\text{O}_3$) nanoparticles have been chosen for the solid phase along with organic molecules (such as citrate, oxalate and pyrocatechol) and arsenic compounds as a liquid phase. In the case of the air-solid interfacial investigation, iron 1,3,5 benzenetricarboxylate, (Fe-BTC) has been chosen as a solid phase with nitrogen oxides (NO_x , $x = 1$ or 2) in the gaseous phase.

1.2 Iron in soil and water

The form of iron oxide surface in bulk aqueous environments or in surface water is reliant on pH of the solution as shown in Scheme 1.1.



Scheme 1.1 Change the surface of iron oxide charge as a function of pH.

Surface charge in aqueous environments is a vital factor in determining the chemistry at the interface. The surface possesses charge depending on the pH of the aqueous media. The pH point at the which the surface possess zero ionic charge is defined as the point of zero charge (pH_{pzc}). This pH_{pzc} is equivalent to the solution isoelectric point (pH_{isep}), when the concentration of positively charged species equals that of negatively charged ones. However,

actual values of pH_{pzc} and pH_{isep} for the same metal cation are different due to differences in the solvation of surface species contrasted with those in solution and differences in the coordination shell around the metal in each case. Typically, the adsorption of the anion occurs at pH equal or below the pH_{pzc} while cation adsorption is more favored at or above the pH_{pzc} . Also, dissolution rates of oxides increase below pH_{pzc} with decreasing pH and increase with increasing pH in alkaline media. The interactions of organic matter with iron oxides surfaces are important and have an influence over the degradation and photochemical decay rate of iron.⁶ In aqueous geochemistry, these interactions occur via several mechanisms that alter the charge and functional groups of the metal oxide surface. In addition, there are changes in water structure and hydrophobic behavior at the interface. The adhesion strength and dissolution of metal oxide is also influenced by the interactions of organic matter and the metal oxide surface. Thus, dissolution due to interaction of the iron oxide surface with organic matter leads to the enhancement of bioavailable iron as a nutrient and turns to the food source for microbes. These molecular-level changes play a vital role in the mobility and bioavailability of iron and other pollutants in soil and aqueous environment.⁷ Among these pollutants are arsenic (As) compounds, which are the species of focus of this thesis.

As is known as a lethal element and considered a carcinogenic for the human being.⁸ It can be found in rocks and minerals in the form of arsenopyrite (FeAsS). Also, it can be often found as an associate member with the transition metals Cd, Pb, Ag, Au, Sb, P, W and Mo.^{8,9} Two types of arsenical compounds are found in the environment: inorganic arsenic and organic arsenic compounds. Inorganic arsenic includes arsenite [As (III)] and arsenate [As (V)]. These arsenic compounds are more toxic than organic arsenic such as methylated ones such as, monomethylarsonate [MMA] or dimethylarsinate [DMA]. As has been spotted into the atmosphere and the source of As release includes anthropogenic activities as well as natural processes. Anthropogenic sources of As (mostly arsine gas, AsH_3) into the atmosphere include

industrial smelting, combustion fossil fuel, and mining, followed by their discharged waste products that include fly ash and mine wastes. Volcanic eruption is known as the main natural source of As.¹⁰ Also, As exists as arsenic trioxide (As_2O_3) in the atmosphere. Strong oxidizing agents such O_3 and HNO_3 can oxidize As_2O_3 to yield arsenic pentoxide (As_2O_5) or the corresponding triprotic arsenic acid (H_3AsO_4). After several chemical processes in the atmosphere As is transported into the aquatic system through wet deposition as arsenic H_3AsO_4 . It has been found that under neutral soil and water condition inorganic arsenite As(III), exists as a neutral species (pK_a : 9.23, 12.1) while arsenate [As (V)] exists as an anion (pK_a 2.22, 6.98 and 11.53).¹¹ The mobility of As in soil can be influenced by mineral and organic matter contents in soil and occurs in three different ways. Firstly, reductive dissolution of iron-oxide or direct oxidation-reduction reactions that result in the formation of As(III) and As(V) species. Secondly, competition may take place between organic matter and arsenical for binding sites on metal-oxide/mineral surface. Thirdly, a ternary iron bridged complex (As-Fe-Org) can be formed where iron is bridged between As and organic matter. Thus, organic matter in soil and water play a vital role in the mobility of As species as well as iron as nutrient.¹²⁻¹⁵ Considering the importance of organic-metal oxide interfacial interactions, their consequence on the mobility of As in environment, investigations are needed to mimic real systems and conditions. Knowledge is required to explore the kinetics of adsorption and desorption of organic matter to or from metal oxides and how the surface complexation impacts the adsorption kinetics of inorganic and organic arsenical compounds.

1.3 Iron in the atmosphere

Hematite ($\alpha\text{-Fe}_2\text{O}_3$) is one of the common oxides in mineral dust aerosols in the atmosphere.¹⁶ These iron-containing aerosols can provide reactive adsorption sites for a variety of trace gases and plays a dynamic role in numerous chemical transformations in heterogeneous atmospheric chemistry. Moreover, surface water plays an important role in several

heterogeneous reactions of mineral dust particles with gas phase species (For examples: OH, O₃, SO₂, NO₂, and HNO₃).¹⁶ Mineral dust is one of the primary types of aerosols that are directly emitted into the atmosphere by natural processes like dust storms or other wind-driven processes. After several chemical transformations in the atmosphere, iron is added to the ocean surface through deposition of mineral dust. As a result, iron undergoes dissolution in aqueous solution and forms complexes with organic matter. On the other hand, secondary organic aerosols (SOA) originating from the photochemical reactions of gas-phases organic species, directly emitted into the atmosphere. These gas-phase organics can go through an oxidation processes and narrow down in volatility and thus can create new particles or can be condensed on a particle surface that already exist (Figure 1.2).^{17,18}

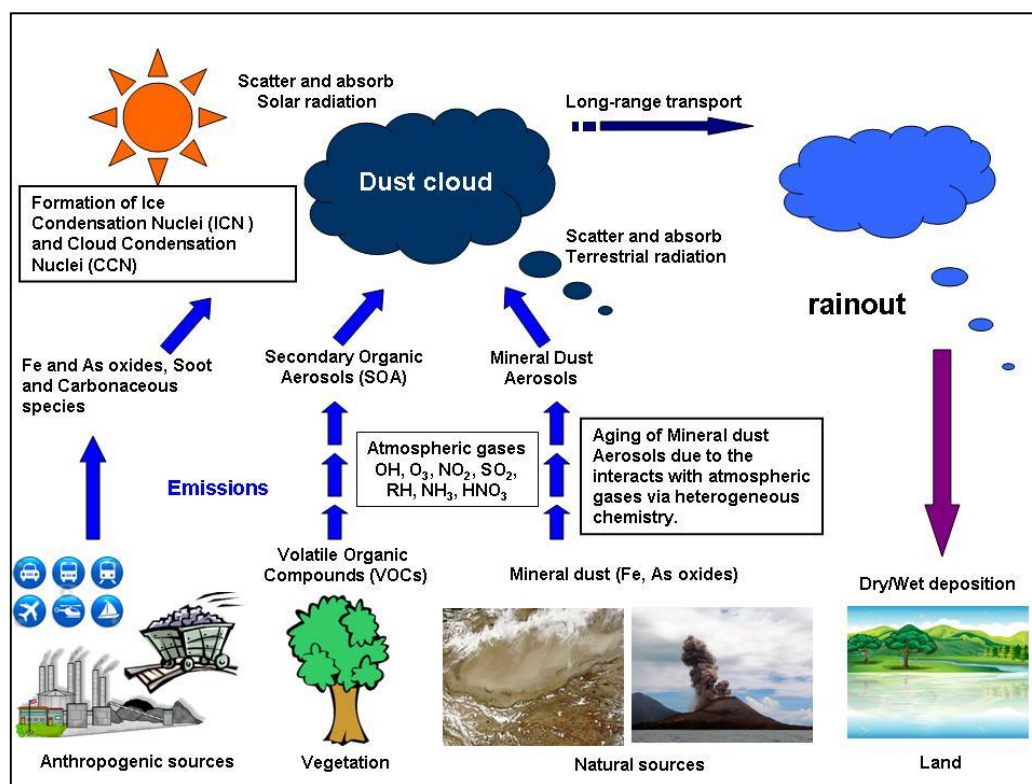


Figure 1.2 Pictorial presentation of environmental processes (both natural and anthropogenic sources of gases and particles in the atmosphere and their consequence) that occurs on the earth.

The phase of the mineral dust particles in aerosol can change with time due to chemical aging and relative humidity (RH).¹⁹ Moreover, photochemical reactions can play a significant

role in changing the composition of dust aerosols due to the presence of chromophores (For example: humic-like substances (HULIS), nitrite, nitrate etc.) and transition-metals such as iron (Fe).²⁰ Aerosol particles that include mineral dust and SOA can perform as a cloud condensation nuclei (CCN) as well as ice condensation nuclei (ICN), followed by the formation of cloud droplets and atmospheric ice particles, respectively. Consequently, these particles can exert a considerable effect on the microphysical properties of water and ice clouds that eventually allows the formation of precipitations such as rain, snow, and storm. Mineral dust aerosols can change the energy balance of the earth as well as influence climate both directly and indirectly.²¹⁻²³ This occurs directly through light absorption, scattering and terrestrial radiation and indirectly by providing surfaces for reaction and modifying cloud formation and lifetime. Thus, dust particles can reduce visibility and cause harmful effect on human health.¹⁵ However, the role of iron in the transformation of organic species in atmospherically related surfaces is still unexplored and a subject of further investigation.¹⁷ Moreover, little is known about the chemistry involved in multicomponent atmospheric aerosol systems containing surface water, organic matter, iron and halides.

1.4 Iron as a remedial material in heterogeneous catalysis

Heterogeneous reactions that occur in the atmosphere due to the presence of particles and gases, have a harmful effect on the local and global environment. For a better and more sustainable environment, it is important to remove or reduce the harmful atmospheric gases to minimum concentration level such as nitrogen oxides (NO_x , $x = 1$ or 2). NO_x is generated by anthropogenic activities (such as diesel engine, coal combustion, and incineration power plants) and are involved in the processes that produce photochemical smog and acid rain. Moreover, NO_x has a rich chemistry in the atmosphere due to its high reactivity.¹⁶ Considering the harmful effect of NO_x , it has become an important environmental concern to control and remove NO_x from the air.¹⁶ The technology that is currently used in the removal of NO_x is

selective catalytic reduction (SCR) that facilitate conversion NO_x into nitrogen and water.²⁴ The materials that have been used so far for the removal of NO_x are activated carbon, activated carbon fiber (ACFs), slugged derived adsorbent and zeolites. Nevertheless, the selective catalytic reduction (SCR) of NO_x with NH_3 has been documented as one of the most effective methods that converts NO into N_2 .²⁵ Catalysts play an important role in this conversion that determine the NO removal efficiency. $\text{V}_2\text{O}_5\text{-WO}_3/\text{TiO}_2$ or $\text{V}_2\text{O}_5\text{-MoO}_3/\text{TiO}_2$ honeycomb monolith catalyst are commonly used in industrial applications. However, these catalysts have shown some drawbacks and found to be deactivated during application mainly due to high temperature and large quantity of dust.²⁶ Various approaches have been taken to overcome these problems while several groups investigating with other materials to develop efficient catalyst for $\text{NH}_3\text{-SCR}$ for NO_x removal.²⁷ Recently, metal-organic frameworks (MOFs) have emerged as a new class of useful materials.^{28,29} They are unique materials having metal building unit together with coordinated organic linkers to form extended regular one, two- or three-dimensional structure (Figure 1.3).³⁰

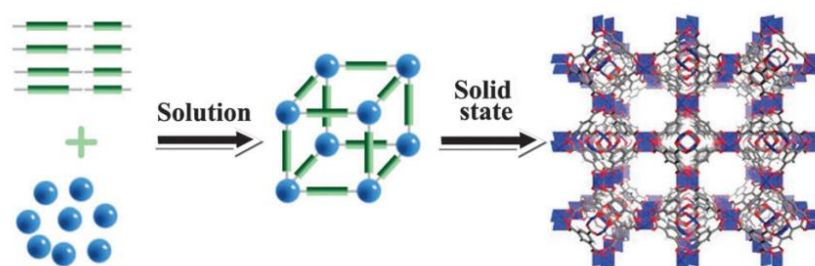


Figure 1.3 Organic linkers and metal ions or clusters combine to synthesize metal-organic framework materials (*re-printed with permission from Ref 30*).

Iron-containing materials have been used as environmental catalyst and for remediation on a number of occasions due to their stability, low cost and environment-friendly.³¹ Iron-containing MOF can be employed in this regard. Fe-based structures are known as the most promising type of MOFs due to their high thermal stability, low cost, high biocompatibility

and low toxicity.³² Fe-BTC (BTC: 1,3,5-benzenetricarboxy- late) is one of the MOFs that has been commercialized by BASF under the name of Basolite.³³

1.5 Surface Sensitive Techniques

Numerous surface sensitive techniques have been exploited to characterize oxide surfaces. Typically, electron-based spectroscopy, vibrational spectroscopy, non-linear spectroscopy, scanning probe microscopy (SPM) and synchrotron-based X-ray techniques are among the methods currently been used to probe environmental processes on oxide surfaces (Figure 1.4).²

Techniques Used to Study Environmental Interfaces			
<i>1. Electron Based</i>	<i>2. Vibrational Spectroscopy</i>	<i>3. Scanning Probe Microscopy and Spectroscopy</i>	<i>4. X-ray Absorption</i>
X-ray Photoemission Spectroscopy (XPS)	Attenuated Total Reflection (ATR)	Scanning Tunneling Microscopy (STM)	Surface Extended X-ray Absorption Spectroscopy (SEXAFS)
Ultraviolet Photoemission Spectroscopy (UPS)	Reflection Absorption Infrared Spectroscopy (RAIRS)	Scanning Tunneling Spectroscopy (STS)	Near-edge Extended X-ray Absorption Spectroscopy (NEXAFS)
Electron Energy Loss Spectroscopy (EELS)	Sum Frequency Generation (SFG)	Atomic Force Microscopy (AFM)	Florescence Yield X-ray Absorption Spectroscopy (FYXAS)
	Second Harmonic Generation (SHG)		X-ray Standing Wave (XSW)

Figure 1.4 Surface sensitive techniques normally used to study environmental interfaces.

Infrared spectroscopy is one of the potential methods for measuring the vibrational spectra of adsorbates on surfaces that has been extensively used for studying systems of environmental importance. The technique provides useful information about surface species that are formed upon adsorption or surface reaction. Infrared spectroscopy can be in different

forms such as reflection absorption infrared spectroscopy (RAIRS), diffuse reflectance infrared spectroscopy (DRIFTS), transmission Fourier transform infrared (FT-IR) spectroscopy, and multiple internal reflection (MIR) spectroscopy. These techniques are based on the linear optics where the bulk signal is much more intense than the signal derived from the interface. Surface reactions are mainly monitored by proper subtraction of the bulk contribution that can often cause anomalous errors. Another infrared-based technique developed for *in situ* investigations of liquid/solid interfaces is attenuated total reflection Fourier transform infrared (ATR FT-IR) spectroscopy. This technique differs from traditional transmission IR techniques in that very short effective path lengths on the order of tens microns can be achieved. This criterion makes ATR techniques powerful tools for measuring IR spectra of liquid solutions with strong IR absorber solvents such as water. The internal reflection element (IRE) is usually a high refractive index crystal such as Ge and ZeSe. When the IR beam enters the crystals, it is internally reflected several times until it exits. The probe radiation at the reflection point is an exponentially decaying wave (evanescent wave) on the order of a micron and less. Here, the reflectivity is a measure of the interaction of the evanescent wave with the sample, thus the resulting spectrum is characteristic of the sample. The penetration depth of the evanescent wave, d_p , is defined as the distance required for the amplitude of the electric field to fall to e^{-1} of its value at the surface. It depends on the refractive index of the IRE, n_1 , the sample, n_2 , angle of incidence, θ , and the wavelength of the incident light according to the following equation 1.1.

$$d_p = \frac{\lambda}{2\pi n_1 \sqrt{\sin^2 \theta - (n_2/n_1)^2}} \dots \dots \dots 1.1$$

The absorbance spectra obtained by ATR means differ from those obtained using conventional transmission methods in that correction for varying depth of penetration with wavelength is necessary. Upon proper subtraction of spectra due to the solvent and the clean surface, spectra

due to the interfacial region can be easily obtained. ATR techniques have been employed for studying different environmental systems at the molecular level such as surface complexation and dissolution of minerals and water structure in many aqueous environments. In this PhD research both ATR-FTIR and DRIFTS, have been extensively applied to characterized surface species for both solid-liquid and air-solid interaction reactions.

1.6 Research questions and objectives

Currently, the environmental problems and concerns are increasing gradually. Therefore, it is important to study and understand the environmental processes on a molecular level. As mentioned earlier, iron plays a vital role in numerous environmental processes such as aqueous geochemistry, heterogeneous atmospheric chemistry and environmental catalysis and remediation, it requires high level of investigation in these three distinctly separated areas. In these studies, we set our goal on finding the answers to the following questions in these three distinct areas:

- a. How organic matter (particularly -OH and -COOH containing organic matter) interacts with iron oxide surfaces in water?
- b. What types of surface complexes are formed during these interactions of organic matter and iron oxide surface? How are these interactions effected by the changes in pH and electrolytic conditions?
- c. In aquatic systems, how does organic matter on oxide surface, affects the binding kinetics of pollutants such as Arsenic (As)?
- d. How does gas-phase water interact with iron-containing secondary organic polymers that exist in the atmosphere? And last but not the least,
- e. How can iron containing materials be used as a useful remediation material to reduce NO_x , one of the main pollutants in the air?

In these studies, the above questions have been covered and described one by one, on a molecular level under different environmental conditions. However, the main purposes of this thesis are as follows:

1. Investigate the role of iron oxide in mobility and bioavailability of arsenic and effect of organic matter in soil and water.
2. Explore the role of iron oxide in the secondary formation due to interactions with model organic compounds containing C2-C6 dicarboxylic acids and
3. Study the effectiveness of Fe-MOF materials in the catalytic reaction of nitrogen oxides (NO_x , $x = 1$ or 2).

1.7 Thesis organization

This thesis contains six different chapters. Chapter 1 highlights the introductory description on iron and its role in different environmental processes. Chapter 2 to Chapter 5 come up with four distinct projects. Each of these chapters has been divided into six parts such as introduction; objectives; experiments; results and discussion; conclusion and references. Finally, Chapter 6 contains the overall conclusions and significance followed by appendices. The content for each chapter of my thesis is stated below:

Chapter 1 *General Introduction*

Chapter 1 describes the general introduction of my thesis and sets the tone for the remaining chapters. This chapter talks about the iron (Fe), how it exists in the natural environment; its introduction to the soil and water; its role in the atmospheric chemistry and finally usefulness of iron as a remediation material in a concise manner. In addition, this chapter contains the research questions and objectives together with the organization of overall thesis.

Chapter 2 *Spectral Characterization of Organics on Hematite Nanoparticles, H/D Exchange Experiments*

Chapter 2 illustrates the H/D exchange experiments that were completed to address the questions raised during publishing the paper in “Environmental Nano, 2016, 3, (4), 910-926”. This paper highlights the spectral characterization of low molecular weight organics on hematite nanoparticles and the role of electrolytes in the binding mechanisms. In order to complement the experiments completed by Arthur Situm, a former student member from our group, H/D exchange experiments were performed. He completed the experiments that were associated with spectral characterization of surface organics (citrate, oxalate and pyrocatechol) as a function of pH onto hematite nanoparticle in H₂O. However, my contribution to the paper are the experiments associated with spectral characterization of surface organics (citrate, oxalate and pyrocatechol) as a function of pD onto hematite nanoparticles in D₂O. These experiments were performed to study the effect of H/D exchange on the structure of organic complexes on hematite nanoparticles, particularly to investigate the possible association of protons with the organics surface complex by Attenuated total internal reflectance Fourier transform infrared spectroscopy (ATR-FTIR).

Chapter 3 *ATR-FTIR Studies on the Initial Binding Kinetics of Arsenicals at the Organic-Hematite Interface*

Chapter 3 describes the initial binding kinetics of arsenicals at the organic-hematite interface by ATR-FTIR. These experiments were done to complement the experiments completed by Arthur Situm, a former student member from our group, in order to publish “Journal of Physical Chemistry (A), 2017, 121, 5569-5579”. Here, the adsorption kinetics of dimethyl arsenic acid (DMA) and arsenate with hematite nanoparticles, preloaded to three different types of organics such as citrate, oxalate and pyrocatechol, were studied by *in situ*

ATR-FTIR. As mentioned earlier, Arthur completed the experiments of arsenate and DMA with hematite pre-exposed to citrate, in different electrolytes such as NaCl, KCl and KBr. My contribution to the paper is the experiments of arsenate and DMA with hematite pre-exposed to oxalate and pyrocatechol, in different electrolytes such as NaCl, KCl and KBr. Chapter 3 contains an in detail study of the experiments that I contributed to the JPC (A) paper.

Chapter 4 *Surface Water Structure and Hygroscopic Properties of Light Absorbing Secondary Organic Polymers of Atmospheric Relevance*

Chapter 4 demonstrates the structure of surface water onto light absorbing organic and organometallic polymeric particles, such as polycatechol, polyguaiacol, Fe-polyfumarte, and Fe-polymuconate. Also, the hygroscopic properties of these organic and organometallic polymeric particles were investigated. This work was published in “ACS Omega, 2018, 3, 15519-15529”. I am the first author of this paper and contributed by all the experiments, trouble shooting and data analysis, associated with this paper. It has been found that these particles are formed in iron-catalyzed reactions that contain aromatic and aliphatic dicarboxylic acid compounds and spotted in field-collected SOA. The structural characterization of surface water was done by diffuse reflectance infrared Fourier transform spectroscopy (DRIFTS). In addition, the gas-phase water uptake behavior of the particles was quantified using quartz crystal microbalance (QCM) as a function of relative humidity.

Chapter 5 *Application of Metal-Organic Frameworks (MOFs) to Enhance the Selective Catalytic Reduction of NO_x to Nitrogen Gas*

Chapter 5 focuses on the elucidation of the performance of the metal-organic frameworks (MOFs) for the selective catalytic reduction of NO_x by NH₃ as a reductant. Here, Fe-BTC MOFs and CoFe₂O₄ nanomaterials have been chosen for the NH₃-SCR to examine their performance as catalysts. I am the first author of this work and did all the experiments,

trouble shooting and data analysis, associated with this project. The surface and gas phase species were characterized and quantified separately by DRIFTS and gas flow IR, respectively.

Chapter 6 *Conclusions and Significance*

Chapter 6 highlights the overall concluding remarks and significance that is related to the three distinct areas of our environment. In these studies, we reported the interactions of organic matter with iron oxide surface accompanied by the initial binding kinetics of arsenicals with hematite nanoparticles preloaded to the organics, which are ubiquitous in nature and represents the environmental processes associated to the aquatic geochemistry. On the other hand, study of the characterization of surface water structure onto organic and organometallic polymeric particles, reflects the chemical processes that occur in the atmospheric system. Moreover, iron-containing MOFs as a catalyst can be useful to purify our environment and remove harmful gases, have been discussed to highlight the role iron plays as a remediation material. Chapter 6 has extended discussion on the conclusion and significance of this thesis followed by appendices.

1.8 References

- (1) Xing, W.; Liu, G. Iron Biogeochemistry and Its Environmental Impacts in Freshwater Lakes. *Fresenius Environ. Bull.* **2011**, *20* (6), 1339–1345.
- (2) Al-Abadleh, H. A.; Grassian, V. H. Oxide Surfaces as Environmental Interfaces. *Surf. Sci. Rep.* **2003**, *52* (3–4), 63–161.
- (3) Wu, W.; Wu, Z.; Yu, T.; Jiang, C.; Kim, W. S. Recent Progress on Magnetic Iron Oxide Nanoparticles: Synthesis, Surface Functional Strategies and Biomedical Applications. *Sci. Technol. Adv. Mater.* **2015**, *16* (2), 23501.
- (4) Das, S.; Hendry, J. M.; Essilfie-Dughan, J. Supplementary Information For: The Transformation Of 2-Line Ferrihydrite To Goethite And Hematite As A Function of pH

- And Temperature. *Environ. Sci. Technol.* **2011**, *45* (1), 268–275.
- (5) Matsui, H.; Mahowald, N. M.; Moteki, N.; Hamilton, D. S.; Ohata, S.; Yoshida, A.; Koike, M.; Scanza, R. A.; Flanner, M. G. Anthropogenic Combustion Iron as a Complex Climate Forcer. *Nat. Commun.* **2018**, *9* (1), 1–10.
- (6) Situm, A.; Rahman, M. A.; Goldberg, S.; Al-Abadleh, H. A. Spectral Characterization and Surface Complexation Modeling of Low Molecular Weight Organics on Hematite Nanoparticles: Role of Electrolytes in the Binding Mechanism. *Environ. Sci. Nano* **2016**, *3* (4), 910–926.
- (7) Kleinert, S.; Muehe, E. M.; Posth, N. R.; Dippon, U.; Daus, B.; Kappler, A. Biogenic Fe(III) Minerals Lower the Efficiency of Iron-Mineral-Based Commercial Filter Systems for Arsenic Removal. *Environ. Sci. Technol.* **2011**, *45* (17), 7533–7541.
- (8) Mudhoo, A.; Sharma, S. K.; Garg, V. K.; Tseng, C.-H. Arsenic: An Overview of Applications, Health, and Environmental Concerns and Removal Processes. *Crit. Rev. Environ. Sci. Technol.* **2011**, *41* (5), 435–519.
- (9) Sánchez-Rodas, D.; Sánchez de la Campa, A. M.; de la Rosa, J. D.; Oliveira, V.; Gómez-Ariza, J. L.; Querol, X.; Alastuey, A. Arsenic Speciation of Atmospheric Particulate Matter (PM₁₀) in an Industrialised Urban Site in Southwestern Spain. *Chemosphere* **2007**, *66* (8), 1485–1493.
- (10) Wai, K. M.; Wu, S.; Li, X.; Jaffe, D. A.; Perry, K. D. Global Atmospheric Transport and Source-Receptor Relationships for Arsenic. *Environ. Sci. Technol.* **2016**, *50* (7), 3714–3720.
- (11) Mikutta, C.; Kretzschmar, R. Spectroscopic Evidence for Ternary Complex Formation between Arsenate and Ferric Iron Complexes of Humic Substances. *Environ. Sci.*

- Technol.* **2011**, *45*, 9550–9557.
- (12) Redman, A. D.; Macalady, D.; Ahmann, D. Natural Organic Matter Affects Arsenic Speciation and Sorption onto Hematite. *Environ. Sci. Technol.* **2002**, *36* (13), 2889–2896.
- (13) Bauer, M.; Blodau, C. Mobilization of Arsenic by Dissolved Organic Matter from Iron Oxides, Soils and Sediments. *Sci. Total Environ.* **2006**, *354* (2–3), 179–190.
- (14) Ko, I.; Kim, J. Y.; Kim, K. W. Arsenic Speciation and Sorption Kinetics in the As-Hematite-Humic Acid System. *Colloids Surfaces A Physicochem. Eng. Asp.* **2004**, *234* (1–3), 43–50.
- (15) Weng, L.; Van Riemsdijk, W. H.; Hiemstra, T. Effects of Fulvic and Humic Acids on Arsenate Adsorption to Goethite: Experiments and Modeling. *Environ. Sci. Technol.* **2009**, *43* (19), 7198–7204.
- (16) Hixson, B. C.; Jordan, J. W.; Wagner, E. L.; Bevsek, H. M. Reaction Products and Kinetics of the Reaction of NO₂ with γ -Fe₂O₃. *J. Phys. Chem. A* **2011**, *115* (46), 13364–13369.
- (17) Prather, K. A.; Hatch, C. D.; Grassian, V. H. Analysis of Atmospheric Aerosols. *Annu. Rev. Anal. Chem.* **2008**, *1* (1), 485–514.
- (18) Goldstein, A. H.; Galbally, I. E. Known and Unexplored Organic Constituents in the Earth's Atmosphere. *Environ. Sci. Technol.* **2007**, *41* (5), 1514–1521.
- (19) Benner, R. Loose Ligands and Available Iron in the Ocean. *Proc. Natl. Acad. Sci.* **2011**, *108* (3), 893–894.
- (20) Tofan-Lazar, J.; Al-Abadleh, H. A. Surface Water Enhances the Uptake and Photoreactivity of Gaseous Catechol on Solid Iron(III) Chloride. *Environ. Sci. Technol.*

- 2014**, 48 (1), 394–402.
- (21) Stevens, B.; Feingold, G. Untangling Aerosol Effects on Clouds and Precipitation in a Buffered System. *Nature* **2009**, 461 (7264), 607–613.
- (22) Carslaw, K. S.; Lee, L. A.; Reddington, C. L.; Pringle, K. J.; Rap, A.; Forster, P. M.; Mann, G. W.; Spracklen, D. V.; Woodhouse, M. T.; Regayre, L. A.; et al. Large Contribution of Natural Aerosols to Uncertainty in Indirect Forcing. *Nature* **2013**, 503 (7474), 67–71.
- (23) Madl, A. K.; Plummer, L. E.; Carosino, C.; Pinkerton, K. E. Nanoparticles, Lung Injury, and the Role of Oxidant Stress. *Annu. Rev. Physiol.* **2013**, 76 (1), 447–465.
- (24) Dhakshinamoorthy, A.; Alvaro, M.; Horcajada, P.; Gibson, E.; Vishnuvarthan, M.; Vimont, A.; Grenèche, J. M.; Serre, C.; Daturi, M.; Garcia, H. Comparison of Porous Iron Trimesates Basolite F300 and MIL-100(Fe) as Heterogeneous Catalysts for Lewis Acid and Oxidation Reactions: Roles of Structural Defects and Stability. *ACS Catal.* **2012**, 2 (10), 2060–2065.
- (25) Roy, S.; Hegde, M. S.; Madras, G. Catalysis for NO_x Abatement. *Appl. Energy* **2009**, 86 (11), 2283–2297.
- (26) Shang, X.; Hu, G.; He, C.; Zhao, J.; Zhang, F.; Xu, Y.; Zhang, Y.; Li, J.; Chen, J. Regeneration of Full-Scale Commercial Honeycomb Monolith Catalyst (V₂O₅ - WO₃/TiO₂) Used in Coal-Fired Power Plant. *J. Ind. Eng. Chem.* **2012**, 18 (1), 513–519.
- (27) Cheng, X.; Bi, X. T. A Review of Recent Advances in Selective Catalytic NO_x Reduction Reactor Technologies. *Particuology* **2014**, 16, 1–18.
- (28) Zhou, H.-C. “Joe”; Kitagawa, S. Metal–Organic Frameworks (MOFs). *Chem. Soc. Rev.* **2014**, 43 (16), 5415–5418.

- (29) Czaja, A. U.; Trukhan, N.; Müller, U. Industrial Applications of Metal–organic Frameworks. *Chem. Soc. Rev.* **2009**, *38* (5), 1284.
- (30) Furukawa, H.; Ko, N.; Go, Y. B.; Aratani, N.; Choi, S. B.; Choi, E.; Yazaydin, a O.; Snurr, R. Q.; O’Keeffe, M.; Kim, J.; et al. Ultrahigh Porosity in Meta-Organic Frameworks. *Science*. **2010**, *329* (5990), 424.
- (31) Youn, H. K.; Kim, J.; Ahn, W. S. MWCNT Synthesis over Fe-BTC as a Catalyst/Carbon Source via CVD. *Mater. Lett.* **2011**, *65* (19–20), 3055–3057.
- (32) Chaemchuen, S.; Kabir, N. A.; Zhou, K.; Verpoort, F. Metal–organic Frameworks for Upgrading Biogas via CO₂ Adsorption to Biogas Green Energy. *Chem. Soc. Rev.* **2013**, *42* (24), 9304.
- (33) Hu, X.; Lou, X.; Li, C.; Ning, Y.; Liao, Y.; Chen, Q.; Mananga, E. S.; Shen, M.; Hu, B. Facile Synthesis of the Basolite F300-like Nanoscale Fe-BTC Framework and Its Lithium Storage Properties. *RSC Adv.* **2016**, *6* (115), 114483–114490.

Chapter 2 Spectral Characterization of Surface Organics on Hematite**Nanoparticles, H/D Exchange Experiments****2.1 Abstract**

This chapter describes the spectral characterization of model organics such as CA, OA and PC onto hematite nanoparticles. ATR-FTIR absorption spectra of adsorbed CA, OA and PC were collected in D₂O as a function of pD from 9-5. These experiments were performed in D₂O in order to interpret the results obtained from the pH envelope experiments for those model organics on hematite nanoparticles. The results from pD experiment show that the existence of a higher degree of outer-sphere complexation for OA than CA, whereas for PC bidentate-binuclear complexes dominates.

2.2 Introduction

Understanding the interactions of organic matter (OM) with metal oxide or minerals at the interfaces of solid-water and surface-controlled reactions is a pre-condition to preserve the organic matter (OM) as well as the stability and transport of both organic and inorganic species in the subsurface soil environments.¹ Interactions between organics and metal oxides/mineral interface are a subject of current interest as they have many important applications in environmental, biological and medical systems.^{2,3} However, due to the complex nature of both organic matters and metal oxides/mineral surfaces, multiple interaction mechanisms have been proposed in the literature. There are several mechanisms through which the interactions of organic matters and metal oxides/mineral interface may take place (Figure 2.1). These interaction mechanisms are well recognized and can be attributed to the characteristic nature of the heterogeneous OM and metal oxides surfaces, their interfacial properties, and the surrounding environmental conditions, particularly, pH and ionic strength. The most common mechanisms involved are ligand exchange, electrostatic interaction, H-bonding, cation bridging, chelation, hydrophobic and van der Waals interactions. All these interactions result

in change on the surface charge and functional groups, hydrophobicity, interfacial water structure, adhesion strength, and dissolution of the metal oxide/mineral phase.³

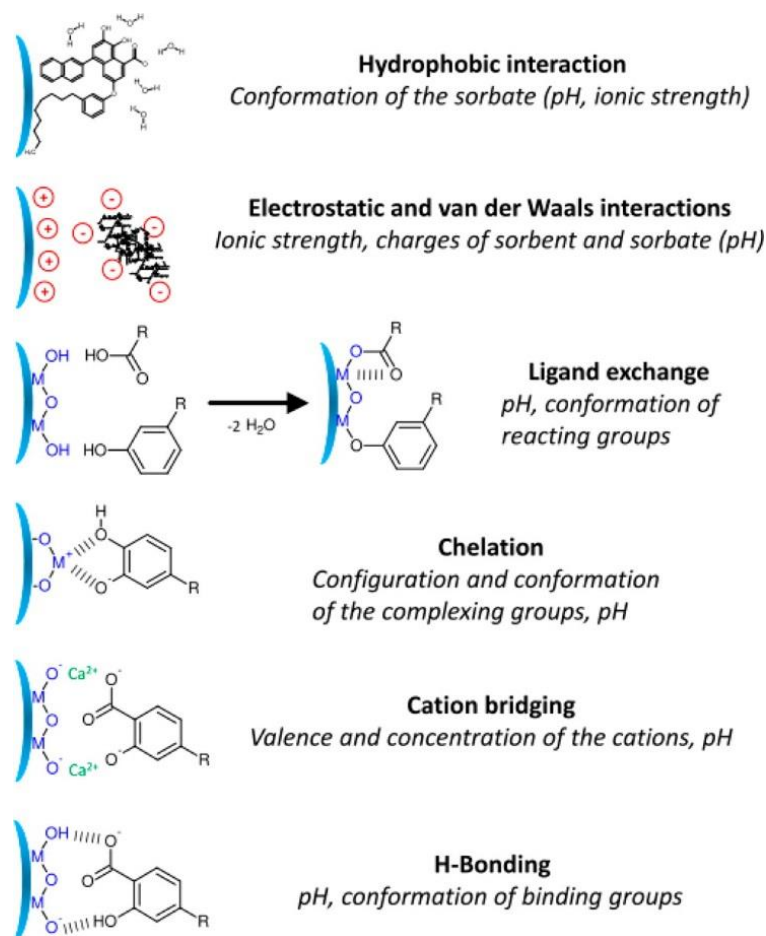


Figure 2.1 Mechanisms for the interaction of organics with metal oxide or mineral surfaces.³ (Reprinted with permission from reference 3)

Ligand exchange is known to be the prevailing mechanism for organic matters sorption on metal oxides surface. The acidic functional groups (-COOH) of OM and hydroxyls (-OH) on the metal oxides surface are liable for this reaction.⁴ There are three steps in the ligand exchange mechanism. In the first step, the protonation of surface hydroxyl of metal oxides occurs. In the second step, the outer-sphere complex may be formed with the protonated hydroxyl groups via -COOH groups or phenolic -OH groups of OM. Otherwise, ligand exchange or condensation reaction between these groups may end up with an inner-sphere complexation. Inner-sphere complexes represent those molecules that are formed by a direct covalent bond or bonds with surface sites via chemisorption, whereas outer-sphere complexes

are formed through electrostatic or weak van der Waals interactions with the surface, typically known as physisorption.⁵

Electrostatic interaction is considered as a vital sorption mechanism, particularly for metal oxides with the point of zero charge (PZC). At this point the pH remains higher than the environmental pH. It is well documented that most of organic matter is negatively charged under typical ambient conditions in the natural environment, and the net charge increases with higher pH due to the protonation of carboxylic and phenolic groups of OM. On the other hand, the solvated metal oxide surfaces or the addition of electrolytes can make the surface charged. Thus, electrostatic interaction between OM and metal oxide surfaces are expected. As the metal oxide surface is positively charged, it can react with negatively charged OM by electrostatic attraction. However, it has been reported that negatively charged surface can also adsorb negatively charged OM through other interactions.⁵

Hydrogen bonding is most likely to be formed in presence of organic adsorbate and metal oxide surface containing the functional groups like -COOH, -OH and -NH₂. In such a system, the polar functional groups like -COOH and -OH in OM act as a hydrogen bonding donor, whereas benzene rings serve as a hydrogen bonding acceptor. However, hydrogen bonding is usually not considered as a driving force of a reaction due to the weakness of the bonding. Moreover, the reduction of hydrogen bonding donors is found to be responsible for the much weaker hydrogen-bond interaction.

Cation bridging is another kind of interaction that occurs through divalent or multivalent metal ions (such as Ca²⁺ or Mg²⁺) to the oxygen-containing functional groups (e.g., -COOH and -OH groups) of metal oxides surface and OM, which facilitates the OM sorption. Cation bridging has influence over the interactions between OM and the metal oxides surface. In addition, this effect can be extended to the adjacent OM interfaces that may form multilayer adsorption of OM onto metal oxides surfaces. However, hydrophobicity of OM and

compression of the electric double layer can enhance the adsorption of OM on the surface. Hydrophobic or van der Waals force interactions are mostly favored by surfaces containing hydrophobic materials such as carbon nanomaterials. It has been found that, the aromatic moieties of OM, having -COOH or OH, are more hydrophobic, relative to that of aliphatic OM and found to strongly bound on surfaces by hydrophobic effects.⁶ Ionization of functional groups can higher the solubility of OM and thus decreases hydrophobic effects. The hydrophobic interactions in related to pH and found to be decreased with higher pH. Hydrophobic interaction between OM and metal oxide surface exist at pH above the PZC of metal oxide. However, hydrophobic and van der Waals force interactions are relatively weak and not worthy to report for the adsorption of OM on metal oxides surface.

Several studied have been reported on the interaction of organic matters and metal oxide and mineral particulates which are *ex-situ* batch measurements. However, *in-situ* experiments are rare and still needed to be addressed with importance to understand the molecular-level details.⁷ In this study, hematite nanoparticles have been choose as metal oxide surface whereas citric (CA) and oxalic (OA) acids and pyrocatechol (PC) as organics. In the literature, the structure of surface organic molecules on iron-(oxyhydr)oxides and iron containing clays and oxides (mostly goethite and ferrihydrite) has been examine by using of transmission and ATR-FTIR spectroscopy. Kubicki *et al.*⁸ studied that chemisorption of OA and CA onto clays. However, the chemisorption of OA and CA onto clays was limited without the presence of Fe-hydroxides within the clay matrix. Wells and co-workers⁹ investigated the spectra of adsorbed citrate on goethite as a function of pH and compared to those collected in aqueous phase species. They examine and proposed the formation of inner-sphere complexes at pH 4.6 and 7 via carboxyl groups, and outer-sphere complexes at pH 8.8 (Figure 2.2).

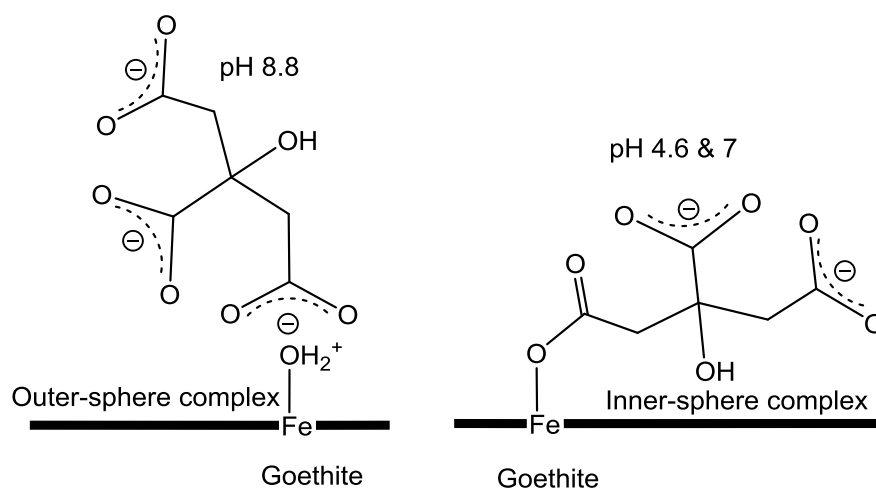


Figure 2.2 Outer-sphere and inner-sphere complexes for citrate with goethite

In another study, the adsorption of citric acid on goethite aqueous suspensions was carried out by Persson and co-workers¹⁰ using 2D infrared correlation spectroscopy formalism. From the spectral analysis they found a protonated adsorbed citrate complex involving only carboxylate coordination at low pH, and an inner-sphere complex at higher pH coordinated via a combination of hydroxyl and carboxylate groups. At pH close to 7, an outer-sphere complex was also identified (Figure 2.3).

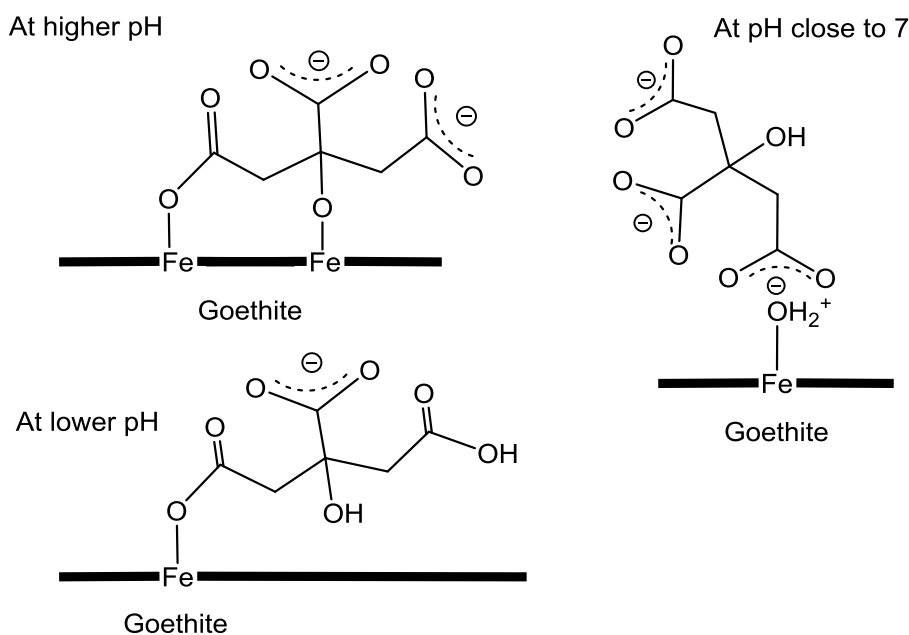


Figure 2.3 Citrate complexes on goethite surface (Outer-sphere and inner-sphere).¹⁰

Filius *et al.*¹¹ reported inner-sphere bidentate binuclear for oxalate on goethite. However, the amounts adsorbed were found to be suppressed upon increasing ionic strength by Mesuere and Fish.¹²

In another investigation, Persson and co-workers,¹³ coupled ATR-FTIR with extended x-ray absorption fine structure spectroscopy (EXAFS) to examine the water-goethite interface upon oxalate complexation as a function of pH. Similar conclusions were made by Cwiertny *et al.*¹⁴ for the adsorption of oxalic acid on goethite micro- and nanorods at pH 3. The adsorption of aqueous phase pyrocatechol on hematite and goethite particles at neutral to basic pH was studied using ATR-FTIR and batch experiments.

Gulley-Stahl *et al.*¹⁵ found that adsorbed pyrocatechol promoted dissolution of Fe₂O₃ under neutral and basic conditions, compared to proton-driven dissolution that is significant under acidic conditions (pH<5). As mentioned earlier organic matters are important considering their role in many types of chemical and biological reactions. They are involved in many types of interaction with metal oxide and mineral surfaces and thus play a vital role in changing the surface properties.

Recently, we published a paper that reports¹⁶ *in situ* spectral characterization of low molecular weight organics complexes on hematite nanoparticle and the role of electrolytes in their binding mechanism. The organics that were investigated are citric (CA) and oxalic (OA) acids and pyrocatechol (PC). These organics were chosen as they are the representative of modest aliphatic and aromatic compounds that may influence the charge and hydrophilicity of the interface significantly upon adsorption. The structure of the surface organics on iron-(oxyhydr) oxides was investigated using *in situ* attenuated total internal reflectance Fourier transform infrared spectroscopy (ATR-FTIR). Two types of experiments were performed using ATR-FTIR such as the adsorption pH envelopes experiments (range 9-5) and H/D exchange experiments (range 9-4). The adsorption pH envelopes experiments were performed by former

group member Arthur Situm whereas I contributed through running the H/D exchange experiments. This chapter will highlight the H/D experiments that were conducted to explore the answer of the questions raised from pH envelopes experiments.

2.3 Objectives

Interaction of organic matter with metal oxide/mineral surface is ubiquitous in natural environment. It is importance to understand the molecular level details and reaction pathways for organic matter and metal oxide surface that exist in nature. In this study, the effect of low molecular weight organic compounds on the charge and hydrophilicity of the interface upon adsorption onto hematite nanoparticles by ATR-FTIR. This chapter will aim to discuss my contribution through performing the experiments for the spectral characterization of surface organics (citrate, oxalate and pyrocatechol) as a function of pD onto hematite nanoparticle.

The purposes of these experiments are as follows:

- i) Spectral characterization of surface organics as a function of pD.
- ii) Study the effect of H/D exchange on the structure of organic complexes on hematite nanoparticles.
- iii) Compare the results obtained by spectral characterization of surface organics as a function of pH.
- iv) To find the answer to the question regarding possible association of protons with the organics surface complex.

2.4 Experimental

2.4.1 Chemicals

Solutions were made by dissolving respective compounds in 0.01 KCl (potassium chloride, ACS grade, 99.0%+, EMD) solution prepared fresh in D₂O (deuterium oxide, 99.9 atom %D, Sigma-Aldrich) and finally adjusted to the desired concentration and pD by using concentrated (40 wt.% solution) NaOD (Sodium deuterioxide, 99.5%, Sigma-Aldrich). Powder of organic

compounds used herein (as received without further purification) include citric acid monohydrate ($C_6H_8O_7 \cdot H_2O$, 99%+, ACS reagent, Alfa Aesar), oxalic acid (Oxalic acid dihydrate, 99%+, ACS reagent, Sigma-Aldrich) and pyrocatechol (99%+, Sigma-Aldrich). All solutions were prepared fresh before the start of each experiment and were covered with parafilm until used. Hematite nanoparticles (α - Fe_2O_3 , 98+%, US Research Nanomaterials, Inc, batch US3180) were characterized for these experiments to obtain BET surface area (N_2 gas, 54 ± 5 m² g⁻¹, Aveka Inc.), isoelectric point (IEP) (zeta potential titration, 8.45, Aveka Inc.), particle shape and size (TEM Philips C12 at 120 keV, spherical, 39 ± 11 nm average spherical diameter, Canadian Centre for Electron Microscopy, McMaster University).

2.4.2 Electrode preparation and calibration of pD meter

23.0 mL of 3M KCl solution was prepared in D_2O . To begin glass electrode was cleaned with milli-pore water and rinsed several times (each time with 1.5-2.0 mL) with freshly prepared 3M KCl/ D_2O . Then, the glass electrode was filled up with 6.0 mL with 3M KCl/ D_2O solution. Buffer solutions were prepared for the calibration of pD meter. The amount of buffer powder in each capsule and amount required for the preparation of buffer solution are given in Table 1 and 2, respectively. Each buffer powder was weighed and placed into a vial. Then, 7.00 mL of D_2O was added into each vial. All the measurements and preparation were performed in the glove box. The pD meter, filled up with glass electrode containing 3M KCl/ D_2O solution, was calibrated with freshly prepared buffers in D_2O (4.00, 7.00 and 10.00). The pD meter was calibrated each time at the start of the experiment.

Table 2.1 Amount of buffer powder in each capsule

pD	Amount (g) 1	Amount(g) 2	Average (g)	Stdv
4.00	1.1102	0.9982	1.0542	0.0792
7.00	1.0327	1.0020	1.0173	0.0217
10.00	1.2038	1.2423	1.2230	0.0272

* Each capsule is used for the preparing 100 mL buffer solution. 7.00 mL of each buffer in D₂O was prepared.

Table 2.2 Amount of buffer power taken for preparation of buffer solution

pD	Amount (g) required for 7.0 mL D₂O	Amount (g) taken for 7.00 mL D₂O
4.00	$1.0542 \times 7 / 100 = 0.0737$	0.0735
7.00	$1.0173 \times 7 / 100 = 0.0712$	0.0713
10.00	$1.2230 \times 7 / 100 = 0.0856$	0.0855

2.4.3 Preparation of film on ZnSe ATR crystal

A film was prepared using 6 mg of hematite nanoparticles in a 1.30 mL water-ethanol [0.91:0.39 (v/v)] mixture. The mixture was ultrasonicated (default power, Fisher Scientific Mechanical Ultrasonic Cleaner FS20) for one hour and the slurry obtained was deposited on a dry ZnSe ATR crystal. The deposited film was allowed to dry for 12-18 hours in air at room temperature (23±2 °C) under an Al-foil tent on the lab bench. The thickness of the hematite

film deposited on the ZnSe ATR crystal was measured by depositing the same amount (6 mg) of the hematite nanoparticles slurry on a glass slide with similar dimensions using an ultra-fast optical profiler (Wyko NT 3300 Series, $7.5 \pm 1.4 \mu\text{m}$, Electrochemical Technology Centre, University of Guelph). This thickness along with the area covered by the film (7.2 cm^2) was used to calculate the bulk density of hematite nanoparticles film ($1.1 \text{ g}\cdot\text{cm}^{-3}$). Aqueous solutions were flowed at a rate of 2 mL min^{-1} across the ATR flow cell using Tygon tubes (0.8 mm I.D., Masterflex) and a compact pump (Masterflex L/S).

2.4.4 ATR-FTIR spectroscopy experiments

ATR-FTIR spectra were collected as a function of time on a freshly prepared hematite nanoparticles film using a HATRPlus accessory (Pike Technologies) installed in a Nicolet 8700 FTIR spectrometer (Thermo Instruments) equipped with a liquid N₂-cooled MCT detector. The ATR flow cell used in the experiments contains 60° ZnSe crystal internal reflection element (IRE, $80 \times 10 \times 4 \text{ mm}$) with volume of $100 \mu\text{L}$. Typically, single beam ATR-FTIR spectra were collected at 8 cm^{-1} resolution with 100 average scans throughout the experiments.

2.4.5 H/D exchange experiments

A single beam spectrum was collected first for the background solution (0.01 M KCl in D₂O at a given pD). This was followed by flowing the standard solution of the compound of interest at a rate of 1 mL min^{-1} for 10 min before collecting a single beam spectrum by averaging 100 scans. Each pD envelope experiment was conducted on a freshly prepared film by first flowing background KCl solution at pD 7 for 10 min followed by KCl at pD 8 or 9 for 10 min and collection of the single beam spectrum. Then, flow of 0.1 mM standard solution of each organic compound started, which was adjusted to the desired pD in the range 5-9 starting with the basic pD and increased nearly 1.0 pD units by concentrated NaOD. Single beam spectra of the surface upon flowing the solutions were collected after 10 min equilibrium time by averaging 100 scans. For each pD experiment, background KCl solution at pD 7 was flowed for 10 min

at a 1 mL/min flow rate, followed by KCl at pD 8 or 9 for 10 min and collection of the single beam spectrum. Then, flow of 0.1 mM standard solution of each organic compound at basic pD 4.02, 3.78 or 6.78 started for 10 min, followed by solutions adjusted to pD ~ 5, 7, 8 or 9, respectively, each for 10 min at a 1 mL/min flow rate.

2.5 Results and discussion

2.5.1 Spectral characterization of surface organics as a function of pD

As stated earlier, ATR-FTIR absorbance spectra of adsorbed citrate, oxalate and pyrocatechol on hematite nanoparticles as a function of decreasing pH in the range 9-5 were obtained by our former group member, Arthur Situm. However, the spectral range reported¹⁷ for these pH experiments (2000-1000 cm^{-1}), contains the band assigned to the bending mode of water, $\delta(\text{H}_2\text{O})$, at 1639 cm^{-1} .

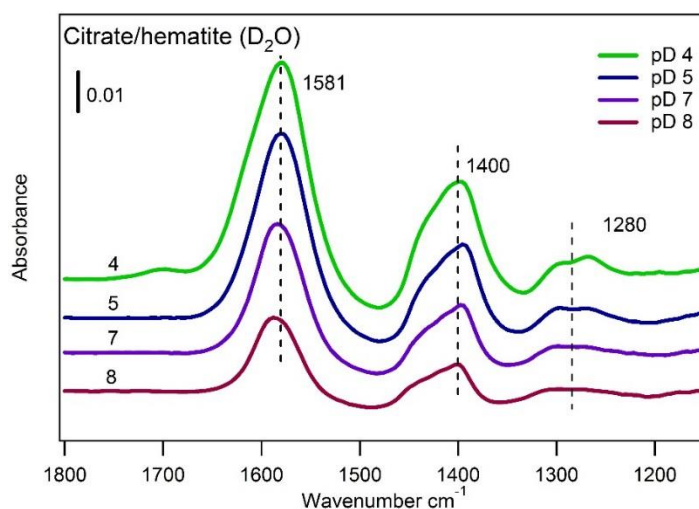


Figure 2.4 ATR-FTIR absorption spectra of adsorbed citrate on hematite nanoparticles after flowing 10^{-4} M solutions prepared in D_2O after 10 min flow as a function of decreasing pD from 8 to 4. The electrolyte concentration was 0.01 M KCl.

This bending mode shifted to 1206 cm^{-1} in liquid D_2O . In order to obtain the actual spectra for the organic complexation, this feature was subtracted by spectral referencing to the background spectrum collected prior to introduce the organic solution. In addition, the spectral range contains $\nu(\text{CO}_2^-)$ and $\nu(\text{CO})$ functional groups, sensitive to protonation and binding to metal oxides. Therefore, to explore the possible association of protons with the organics surface

complexation H/D exchange experiments were performed. For H/D experiments, similar spectra were collected as a function of decreasing pD in the range 9-5 for adsorbed citrate, oxalate and pyrocatechol on hematite nanoparticles. Figure 2.4 shows the ATR-FTIR absorbance spectra of adsorbed citrate on hematite nanoparticles as a function of decreasing pD for solution prepared in liquid D₂O in the range 8-4. Citrate adsorption on hematite nanoparticles in liquid D₂O shows peaks at 1581, 1400 and 1280 cm⁻¹. However, the peaks do not shift with decreasing pD. The peak at 1581 cm⁻¹ is assigned to asymmetric stretching $\nu_a(\text{CO}_2^-)$ whereas peaks at 1400 and 1280 cm⁻¹ are due to symmetric $\nu_s(\text{CO}_2^-)$ and bending mode $\delta(\text{CO}_2^-)$, respectively. Similar type of citrate adsorption took place for pH experiment that shows peaks at 1581 and 1400 cm⁻¹ for symmetric and asymmetric stretching, respectively. While the weak feature at 1257 cm⁻¹ is blue-shifted to 1280 cm⁻¹ in H/D experiment, that implies a strong hydration influence on this mode, which is assigned to $\delta(\text{CO}_2^-)$.

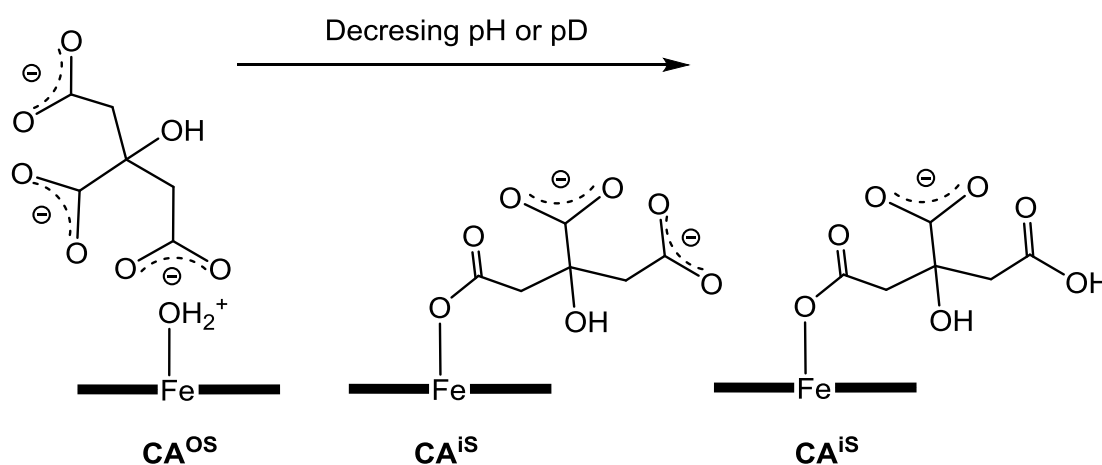


Figure 2.5 Possible structures for the surface complexation of citrate (CA) (out-sphere and inner-sphere) onto hematite nanoparticles. Arrow shows the direction of decreasing pH or pD and the corresponding surface complexes under acidic (right) versus basic (left) conditions.

It has been reported that for both citric and oxalic acids, the location and degree of separation, $\Delta\nu$, between symmetric and asymmetric stretching modes of $-\text{CO}_2$ functional groups, $\nu(\text{CO}_2)$, are sensitive to the degree of protonation and coordination to metal cations.¹⁶ In the case of citrate, for both pH and pD experiments, the value of $\Delta\nu$ among the $\nu(\text{CO}_2)$

features at 181 cm^{-1} , which is in between the 193 cm^{-1} and 178 cm^{-1} calculated for aqueous phase complexed and free citrate species, respectively. Based on the spectral analysis, Figure 2.5 shows a pictorial representation of citrate surface complexes on hematite nanoparticles and possible changes in the structure with decreasing pH or pD.

Figure 2.6 shows the ATR-FTIR absorbance spectra of adsorbed oxalate on hematite nanoparticles as a function of decreasing pD for solution prepared in liquid D_2O in the range 8-4.

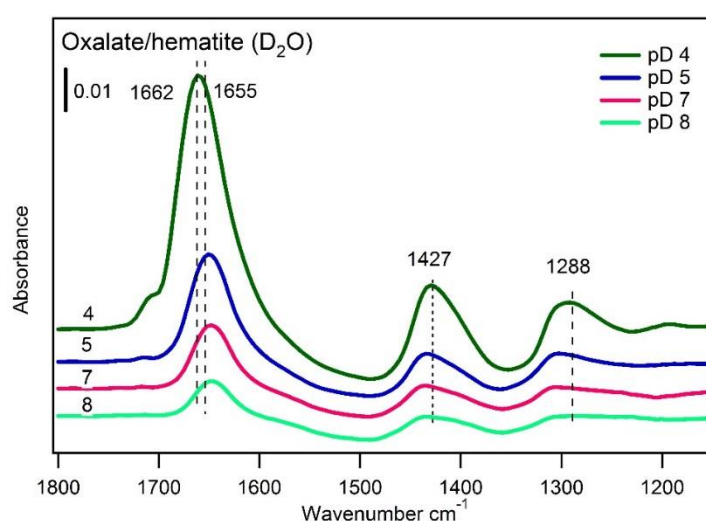


Figure 2.6 ATR-FTIR absorption spectra of adsorbed oxalate on hematite nanoparticles after flowing 10^{-4} M solutions prepared in D_2O after 10 min flow as a function of decreasing pD from 8 to 4. The electrolyte concentration was 0.01 M KCl.

The spectrum of adsorbed oxalate at pD 8 show a feature at 1662 cm^{-1} which blue shifts to 1655 cm^{-1} at pH 4. In addition, an increase in the intensity was observed at 1427 and 1288 cm^{-1} . The value of $\Delta\nu$ among the $\nu(\text{CO}_2)$ increases from 228 to 235 cm^{-1} with decreasing pD. In contrast, the spectra of adsorbed oxalate at pH 9 and 8 shows peak at 1647 cm^{-1} which blue shifts to 1670 cm^{-1} at pH 5. Also, there was an increase in the intensity features at 1427 and 1288 cm^{-1} , similar to that observed in H/D exchange experiments.

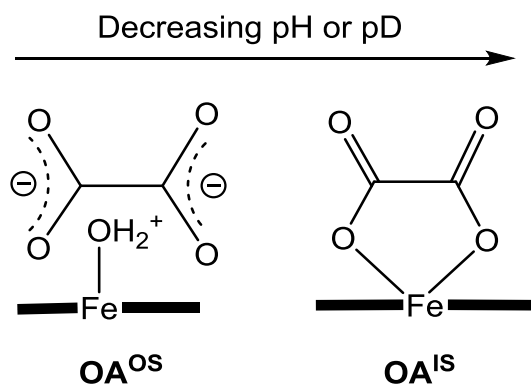


Figure 2.7 Possible structures for the surface complexation of oxalate (OA) (out-sphere and inner-sphere) onto hematite nanoparticles. Arrow shows the direction of decreasing pH or pD and the corresponding surface complexes under acidic (right) versus basic (left) conditions.

However, the value of $\Delta\nu$ among the $\nu(\text{CO}_2)$ features increases from 220 to 243 cm^{-1} with decreasing pH. Thus, these spectra in H_2O compared to those in D_2O highlight the effect of the H/D exchange, shows a relatively narrower width and $\Delta\nu$ of 235 cm^{-1} . This suggests a strong hydration influence on this mode due to outer-sphere complex formation. Based on spectral analysis, Figure 2.7 shows a pictorial representation of oxalate surface complexes on hematite nanoparticles and corresponding change in the structure with decreasing pH or pD.

Figure 2.8 shows the ATR-FTIR absorbance spectra of adsorbed pyrocatechol on hematite nanoparticles as a function of decreasing pD for solution prepared in liquid D_2O in the range 9-6. The adsorption spectra of pyrocatechol show intense peaks at 1481 and 1258 cm^{-1} with a shoulder around 1281 cm^{-1} and weak peaks at 1601 and 1103 cm^{-1} . The spectral features have been proposed to form inner-sphere complex and assigned to $\nu(\text{COFe})$.

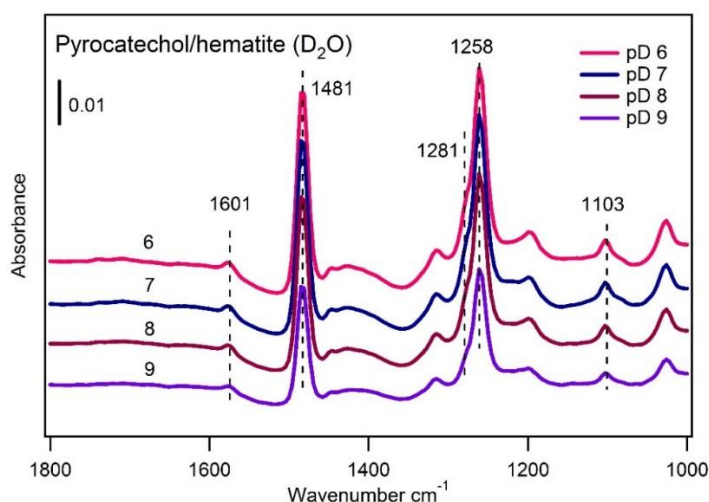


Figure 2.8 ATR-FTIR absorption spectra of adsorbed pyrocatechol on hematite nanoparticles after flowing 10^{-4} M solutions prepared in D_2O after 10 min flow as a function of decreasing pD from 9 to 6. The electrolyte concentration was 0.01 M KCl.

However, comparison of the spectra shows little shifts with decreasing pD and pH, when using D_2O and H_2O as a solvent, respectively.

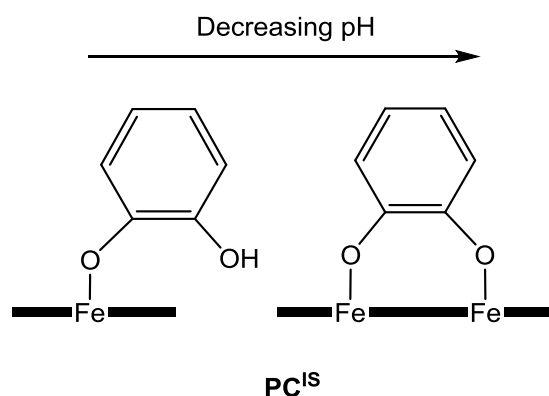


Figure 2.9 Possible structures for the surface complexation of pyrocatechol (PC) (inner-sphere) onto hematite nanoparticles. Arrow shows the direction of decreasing pH or pD and the corresponding surface complexes under acidic (right) versus basic (left) conditions.

These spectral features have been assigned to mostly bidentate inner-sphere complexes with increasing concentration of protonated monodentate inner-sphere complexes (Figure 2.9) with decreasing both pD and pH characterized by the features at 1601 and 1281 cm^{-1} . It has been found that the later features are the most sensitive to H/D exchange as their intensity diminishes considerably when using D_2O as a solvent.

2.6 Conclusions

In summary, *in situ* ATR-FTIR absorption spectra of adsorbed citrate, oxalate, and pyrocatechol on hematite nanoparticles were collected after flowing 10^{-4} M solutions prepared in D₂O as a function of decreasing pD from 9 to 5 in H/D exchange experiments. ATR-FTIR spectroscopy has been known as a powerful surface sensitive technique that is capable of *in situ* characterization of the liquid–solid interface to examine surface adsorption on nanoparticle surfaces in both environmental and biological systems.¹⁸ However, there are some limitations for ATR-FTIR spectroscopy. One of the major challenges is the correct subtraction of the contribution from water. Conducting experiments in D₂O is the best solution to address this limitation. In this study, it was observed that strong hydration influenced the spectra for both citrate and oxalate whereas less in case of pyrocatechol. Thus, spectroscopic data analysis from pH experiments and the results from H/D exchange experiments reveal the existence of a higher degree of outer-sphere complexation for oxalate than citrate, which is dominated by inner-sphere monodentate complexes. Whereas, for pyrocatechol bidentate-binuclear inner-sphere complexes dominates.

2.7 References

- (1) Grillo, R.; Rosa, A. H.; Fraceto, L. F. Engineered Nanoparticles and Organic Matter: A Review of the State-of-the-Art. *Chemosphere* **2015**, *119*, 608–619.
- (2) Mudunkotuwa, I. A.; Grassian, V. H. Biological and Environmental Media Control Oxide Nanoparticle Surface Composition: The Roles of Biological Components (Proteins and Amino Acids), Inorganic Oxyanions and Humic Acid. *Environ. Sci. Nano* **2015**, *2* (5), 429–439.
- (3) Philippe, A.; Schaumann, G. E. Interactions of Dissolved Organic Matter with Natural and Engineered Inorganic Colloids: A Review. *Environ. Sci. Technol.* **2014**, *48* (16), 8946–8962.

- (4) Sun, D. D.; Lee, P. F. TiO₂ Microsphere for the Removal of Humic Acid from Water: Complex Surface Adsorption Mechanisms. *Sep. Purif. Technol.* **2012**, *91*, 30–37.
- (5) Vindedahl, A. M.; Strehlau, J. H.; Arnold, W. A.; Penn, R. L. Organic Matter and Iron Oxide Nanoparticles: Aggregation, Interactions, and Reactivity. *Environ. Sci. Nano* **2016**, *3* (3), 494–505.
- (6) Sun, Q.; Xie, H. Bin; Chen, J.; Li, X.; Wang, Z.; Sheng, L. Molecular Dynamics Simulations on the Interactions of Low Molecular Weight Natural Organic Acids with C₆₀. *Chemosphere* **2013**, *92* (4), 429–434.
- (7) Blesa, M. A.; Weisz, A. D.; Morando, P. J.; Salfity, J. A.; Magaz, G. E.; Regazzoni, A. E. The Interaction of Metal Oxide Surfaces with Complexing Agents Dissolved in Water. *Coord. Chem. Rev.* **2000**, *196* (1), 31–63.
- (8) Kubicki, J. D.; Schroeter, L. M.; Itoh, M. J.; Nguyen, B. N.; Apitz, S. E. Attenuated Total Reflectance Fourier-Transform Infrared Spectroscopy of Carboxylic Acids Adsorbed onto Mineral Surfaces. *Geochim. Cosmochim. Acta* **1999**, *63* (18), 2709–2725.
- (9) Lackovic, K.; Johnson, B. B.; Angove, M. J.; Wells, J. D. Modeling the Adsorption of Citric Acid onto Mulloorina Illite and Related Clay Minerals. *J. Colloid Interface Sci.* **2003**, *267* (1), 49–59.
- (10) Lindegren, M.; Loring, J. S.; Persson, P. Molecular Structures of Citrate and Tricarballylate Adsorbed on α -FeOOH Particles in Aqueous Suspensions. *Langmuir* **2009**, *25* (18), 10639–10647.
- (11) Filius, J. D.; Hiemstra, T.; Van Riemsdijk, W. H. Adsorption of Small Weak Organic Acids on Goethite: Modeling of Mechanisms. *J. Colloid Interface Sci.* **1997**, *195* (2), 368–380.
- (12) Karel, M.; William, F. Chromate and Oxalate Adsorption on Goethite. Calibration of

- Surface Complexation Models. *Environ. Sci. Technol.* **1992**, 26 (12), 2357–2364.
- (13) Karlsson, T.; Persson, P. Complexes with Aquatic Organic Matter Suppress Hydrolysis and Precipitation of Fe(III). *Chem. Geol.* **2012**, 322–323, 19–27.
- (14) Cwiertny, D. M.; Hunter, G. J.; Pettibone, J. M.; Scherer, M. M.; Grassian, V. H. Surface Chemistry and Dissolution of α -FeOOH Nanorods and Microrods: Environmental Implications of Size-Dependent Interactions with Oxalate. *Society* **2009**, No. ii, 2175–2186.
- (15) Gulley-Stahl, H.; Hogan, P. A.; Schmidt, W. L.; Wall, S. J.; Buhrlage, A.; Bullen, H. A. Surface Complexation of Catechol to Metal Oxides: An ATR-FTIR, Adsorption, and Dissolution Study. *Environ. Sci. Technol.* **2010**, 44 (11), 4116–4121.
- (16) Situm, A.; Rahman, M. A.; Goldberg, S.; Al-Abadleh, H. A. Spectral Characterization and Surface Complexation Modeling of Low Molecular Weight Organics on Hematite Nanoparticles: Role of Electrolytes in the Binding Mechanism. *Environ. Sci. Nano* **2016**, 3 (4), 910–926.
- (17) Lappi, S. E.; Smith, B.; Franzen, S. Infrared Spectra of H_2^{16}O , H_2^{18}O and D_2O in the Liquid Phase by Single-Pass Attenuated Total Internal Reflection Spectroscopy. *Spectrochim. Acta - Part A Mol. Biomol. Spectrosc.* **2004**, 60 (11), 2611–2619.
- (18) Mudunkotuwa, I. A.; Minshid, A. Al; Grassian, V. H. ATR-FTIR Spectroscopy as a Tool to Probe Surface Adsorption on Nanoparticles at the Liquid-Solid Interface in Environmentally and Biologically Relevant Media. *Analyst* **2014**, 139 (5), 870–881.

Chapter 3 ATR-FTIR studies on the Initial Binding Kinetics of Arsenicals at the Organic-Hematite Interfaces

3.1 Abstract

This chapter investigates the initial adsorption kinetics of arsenicals binding such as DMA to pre-exposed organics (OA and PC) on the surface of hematite nanoparticles by using ATR-FTIR spectroscopy for real time and *in situ* data collection in the flow mode in different electrolytes such as KCl, NaCl and KBr. The results show that the rate of adsorption of DMA was enhanced in the presence of different electrolytes onto hematite nanoparticles surface.

3.2 Introduction

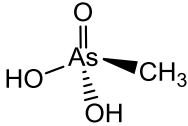
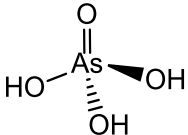
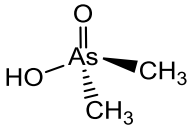
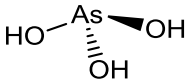
As is a naturally occurring element in our environment and reported as 20th most abundant element in the earth crust.¹ In recent decades, As has drawn much attention due to its contamination of ground, surface and drinking water that has harmful effects on human health.² It is a toxic element and known as a carcinogen.³ In many parts of the world, such as the Gangetic Delta region in Bangladesh and India, As in drinking water is a great concern. Reports on substantial As contamination in these locations have drawn media attention. More than 100 million individual's health were at a health risk due to As contamination in drinking water.^{4,5} Considering the toxicity of As, in 2006, the U.S. Environmental Protection Agency (EPA) dropped the maximum contaminant limit (MCL) of As in drinking water from 50 ppb to 10 ppb.⁶ Hence, it is important to minimize the As levels in the environment.

As compounds can be released from both anthropogenic and natural activities into the environment. Anthropogenic sources of As include the smelting of metals and other industrial processes, the combustion of fossil fuels, and the use of pesticides in agriculture. While, the natural emissions of As include weathering processes (both chemical and physical), biological activity and volcanic emissions. Also, incorporation from soil dust and atmospheric deposition contribute to As exposure. However, human activities are mainly responsible for the emissions

of As to the environment and have been found to be approximately three times higher than natural sources.⁷

Chemically, arsenical compounds can be classified into two different categories. Inorganic and organic As compounds.⁸ In general, inorganic As is more toxic and mobile than organic arsenic species. Trivalent arsenite As^{3+} is found to be more toxic, soluble, and mobile than pentavalent arsenate As^{5+} . Table 3.1 shows the examples and structure of inorganic and organic arsenic compounds.

Table 3.1 Types of arsenic compounds

Organic	Inorganic
 <p>Monomethylarsonic acid As(V) (pKa 3.6, 8.2)</p>	 <p>Arsenic acid As(V) (pKa 2.2, 6.9 & 11.5)</p>
 <p>Dimethylarsinic acid (DMA) As(V) (pKa 6.1)</p>	 <p>Arsenous acid As (III) (pKa 9.29, 12.1)</p>

As is a reactive element and does not exist as a free metal or element in nature. It can form alloys with other elements and undergoes precipitation through oxidation-reduction, methylation-demethylation and acid-base reactions. It is bound in the form of arsenopyrite (FeAsS), realgar (As_4S_4) and orpiment (As_2S_3) in a wide array of rocks and minerals.⁹ These mineralized arsenics are associated with the transition metals Cd, Pb, Ag, Au, Sb, P, W and Mo. Thus, mining and smelting processes produce gases with high concentration of As that eventually oxidize to form arsenic oxide (As_2O_3). Moreover, strong oxidizing agent such O_3

and HNO_3 can oxidize As_2O_3 to yield arsenic pentoxide (As_2O_5) or corresponding triprotic arsenic acid (H_3AsO_4). However, As is more likely to exist as oxide, hydrate, sulfide, arsenate and arsenite in nature.

Figure 3.1 shows the discharge of As into the water, followed by the As cycle on earth in a simplified manner.

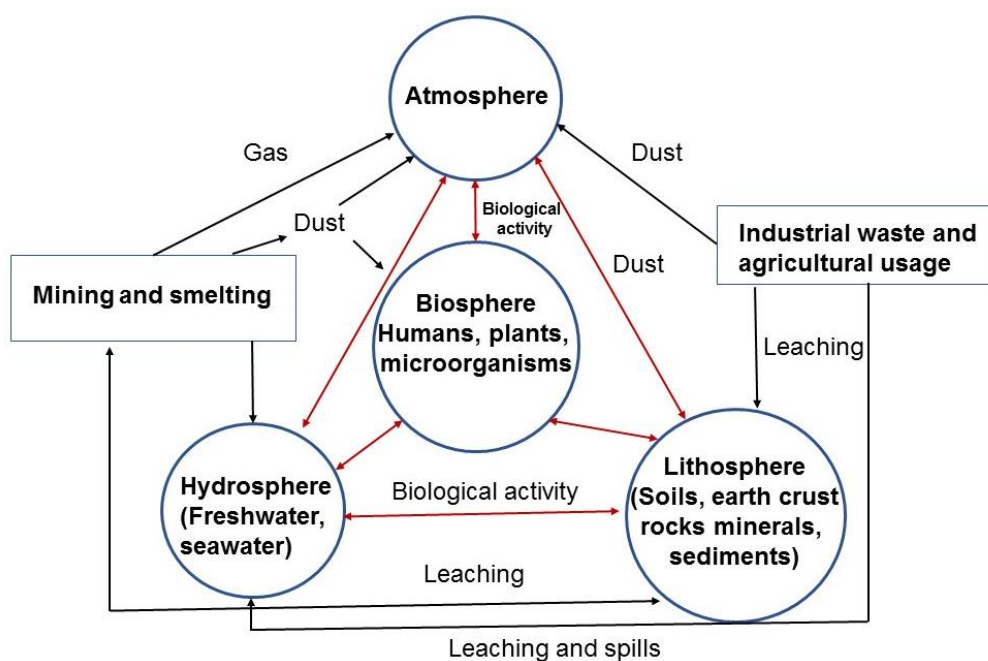


Figure 3.1 Flow diagram of As in the global cycle.⁶

After several chemical steps in the atmosphere As is released into the aquatic system through wet deposition as arsenic H_3AsO_4 . As predominantly exists as either arsenate (V) or arsenite (III) in soil and water, depending on the redox conditions.¹⁰ Also, the toxicity and mobility of As depends on its oxidation state. It has been reported that As(III) is 60 fold more toxic than As(V). As can exist in various oxidation states such as As (-III), As (0), As(+III) and As(+V) oxidation states. Due to having different oxidation states, As can appear in many different chemical states and forms. Under natural soil and neutral water conditions, inorganic As(III), arsenite, exists as a neutral species (pKa: 9.23, 12.1, 12.7). On the other hand, arsenate exists as an anion (pKa: 2.2, 6.9, 11.5) and is predominant under oxidizing conditions. Under environmental conditions, arsenite has high mobility within soils compared to arsenate due to

the lack of charge. Inorganic arsenic can be altered into the organic form through methylation to either monomethylarsonic acid (MMA), dimethylarsinic acid (DMA) or trimethyl arsine TMA. The metabolic pathway of inorganic arsenic involves sequential two-electron reduction of pentavalent species followed by oxidative methylation of trivalent species (Figure 3.2).^{11,12}

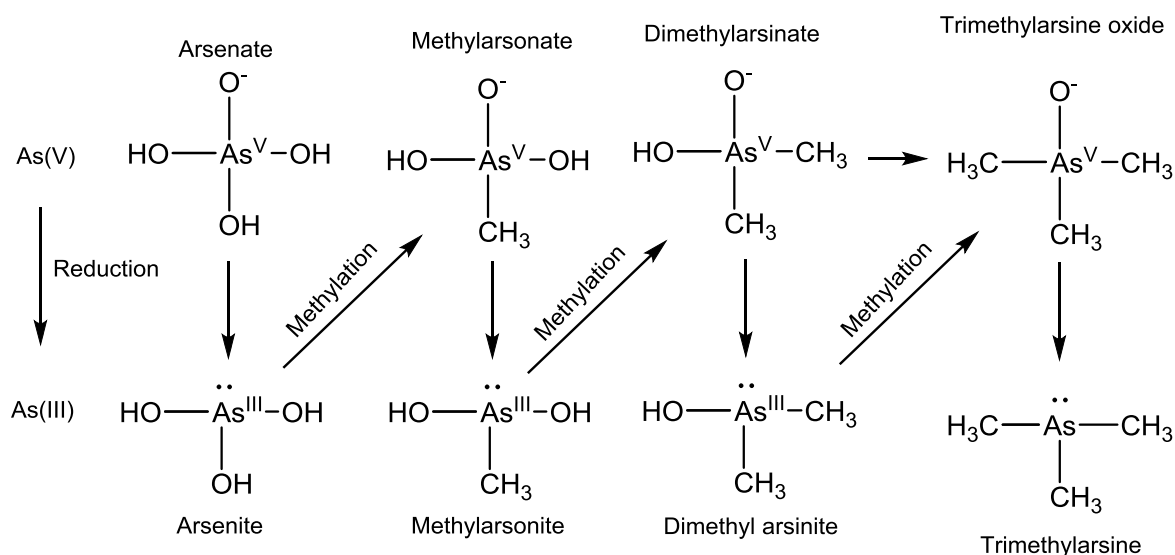


Figure 3.2 The Challenger pathway for biomethylation, followed by sequential reduction and oxidative methylation of arsenic.^{11,12}

The types of As compounds in soil are governed by several factors such as the natures of sorbing materials, pH and the redox potential of the soil. However, it has been suggested that arsenate dominates in the oxidizing conditions of the upper soil layers while arsenite dominates in the reducing conditions of lower soil layers. The anionic charge existing on arsenate results in electrostatic attraction between arsenate and cationic active soil components such as iron oxides, results in adsorption. In soil solution, within the pH range from 4-8, arsenite and arsenate species H_3AsO_3 , H_2AsO_4^- and HAsO_4^{2-} are found to be the most thermodynamically stable.⁶

It is well documented^{13,14} that the mobility of As species is controlled by various processes like precipitation, dissolution, sorption and redox reactions with metal oxides and clay minerals, by competitive adsorption of anions (for example phosphate), and last but not the

least, by redox and complexation reactions with natural organic matter (NOM).¹⁵ NOM is ubiquitous in nature and exists in both aquatic and terrestrial environments as part of the dissolved or solid phase. It is one of the most important components of soil and plays a vital role in several chemical and biological transformations. Figure 3.3 shows the impact of dissolved natural organic matter over the oxidation and hydrolysis processes of contaminants by minerals.

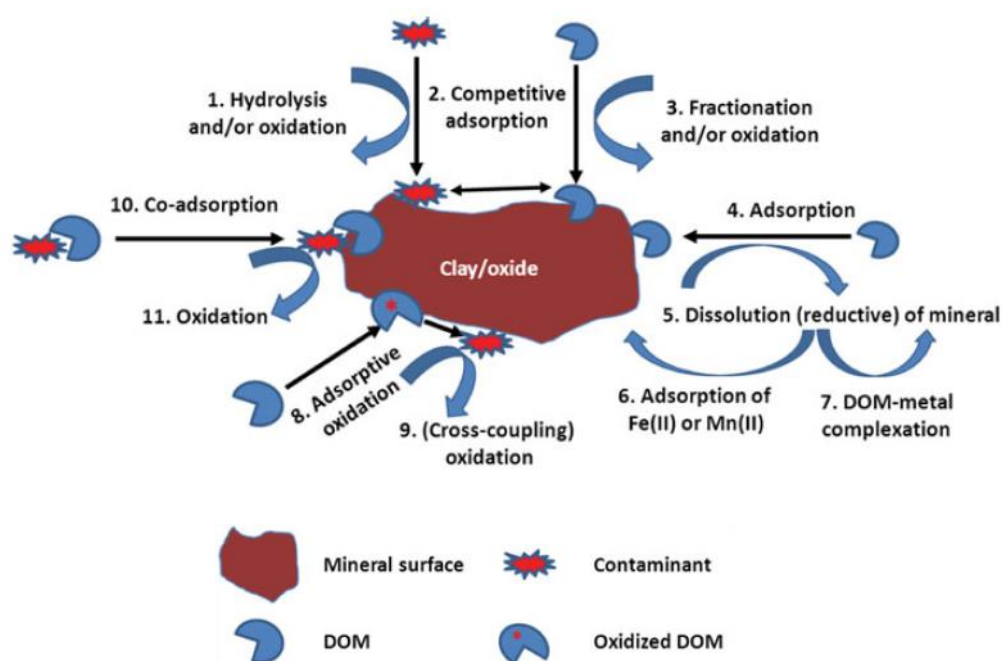


Figure 3.3 Influence of dissolved natural organic matter (DOM) on oxidation and hydrolysis of contaminants by mineral surfaces.¹⁶(Reprinted with permission from Ref 16)

NOM can be involved in competition with contaminants for adsorption sites on mineral surfaces. Besides, it can participate in and/or accelerate mineral dissolution and metal complexation.¹⁶ Thus, these processes can affect the fate and environmental behavior of organic and inorganic pollutants. NOM is a unique combination of different functional groups, such as carboxylic(-COOH), esteric(-RCOOR), phenolic (PhOH), hydroxyl (-OH) etc. Most of these functional groups are negatively charged at neutral pH. The chemical and physical behavior of NOM can vary among the geographical areas, depending on the biomass and active

transformation processes. However, normally, it has been suggested that NOM readily forms both aqueous and surface inner-sphere complexes with minerals or metal oxides.

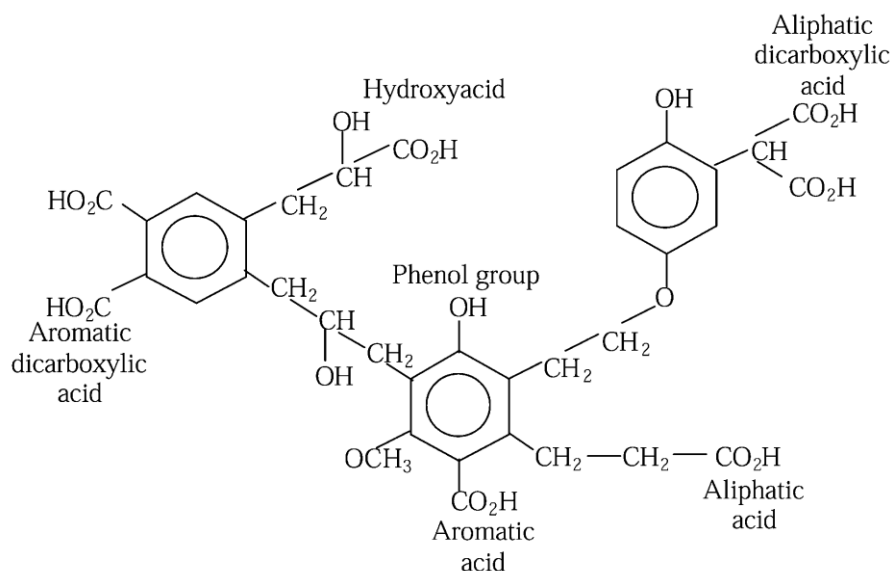


Figure 3.4 Hypothetical molecular structure of humic acid, showing important functional groups.¹⁷

Aqueous NOM-metal complexes can be associated strongly with other dissolved anions through metal-bridging mechanisms, restricting the anions to form surface complexes. NOM is normally discharged from plant roots and microbes,¹⁸ as well as introduced by the decay of biological matter that can be used as agricultural supplements.¹⁹ It can enhance the bioavailability of nutrients like iron (Fe) and phosphorus (P), that is considered as a source of food for microscopic organisms, and thus helps in water retention, that favors soil fertility. It has been suggested that NOM retention in soils is deeply correlated with iron and aluminum oxide content. Consequently, NOM can change the surface properties of the metal oxide/water interface associated with surface charge and functional groups, hydrophobicity, interfacial water structure, adhesion strength, and dissolution rate of the metal oxide (Figure 3.3). Thus, the molecular-level changes have direct effect on the mobility and bioavailability of pollutants

such as arsenic (As).²⁰ NOM has been considered an important factor that can impact As biogeochemistry.

It has been reported^{4,15} that NOM can influence As mobility through three main mechanisms: i) reductive dissolution of iron minerals, or direct redox reactions leading to cycling between arsenite As(III) and arsenate As(V), ii) competition for binding sites at metal oxide/mineral surfaces,^{21,22} and iii) formation of colloidal or dissolved metal bridging complexes with As, which has been described as ternary As-Fe-OM complexes/colloids.^{2,10,23} Thus, NOM plays an important role in influencing As sorption behavior by interacting with metal oxides or mineral surfaces or with As itself, to release As from soils and sediments into the groundwater.

Considering the importance of NOM in the mobility of As, several groups studied the interactions of As with metal oxides, particularly iron oxides, in presence of organic matter. Kinetic batch studies showed that a reduction in the adsorption rates for As(V) and As (III) on hematite-,¹⁵ goethite-,²¹ and ferrihydrite-NOM²⁴ systems accompanied by displacement of sorbed NOM in significant quantities. Redman et al., investigated the effect of NOM on As speciation and sorption on hematite and found direct evidence for the formation of ternary As-Fe-OM complexes/colloids with attenuated total internal reflectance Fourier transform infrared spectroscopy (ATR-FTIR).¹⁵ Batch experiments by Ritter et al.,² investigated the linear associations between the amount of complexed arsenate and the Fe(III) content of the NOM in the dissolved and colloidal phases. The stability of these complexes was found to depend on the pH, relative size of NOM, and ratio of Fe to OM. Silva et al.²⁵ explored the type of functional groups responsible for iron binding in NOM and found that esterification of carboxyl groups reduced iron loading by 84%.

From the above discussion and literature reviews, it is clear that NOM effects As mobility in soils and aquatic environments. Therefore, further study is needed to investigate the

interaction of As onto metal oxide surfaces in the presence and absence of NOM to gain a molecular level understanding. However, given the structural complexity of NOM, it is challenging to establish structure-reactivity relationships that will reflect into how different functional groups react with As compounds. Moreover, there are very few studies investigated the binding of organo-arsenicals to NOM compared to metal(oxyhydr)-oxides. Methylated and aromatic organo-arsenicals have As-O bonds, substituted methyl and phenyl functional groups, and hence can interact with NOM through additional pathways compared to arsenate.

3.3 Objectives

In this work, structure-reactivity relationships from the initial adsorption kinetics upon arsenicals binding to organics on the surface of hematite nanoparticles were established and these measurements were obtained using ATR-FTIR spectroscopy. This technique allows real time and *in situ* data collection in the flow mode. Model organic compounds, namely, oxalate, citrate, and pyrocatechol, were employed, as a representative of most of the reactive functional groups in NOM that will modify the charge and hydrophobicity of the hematite/water interface (Figure 3.5). In order to investigate the effect of organic substituents on arsenate binding to the organic-hematite/ water interface, experiments were conducted with dimethyl arsenate (DMA).²⁰

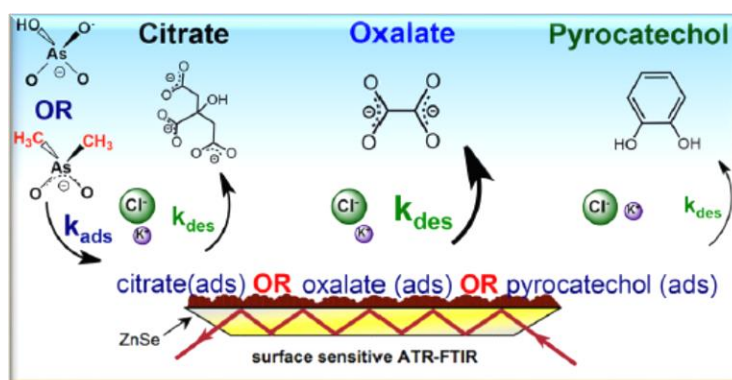
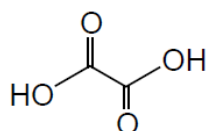


Figure 3.5 Schematic diagram of arsenicals (arsinate or DMA) adsorption onto hematite nanoparticles pre-exposed to model organics citrate (CA), oxalate (OA) and pyrocatechol (PC).²⁰

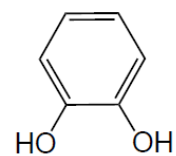
This chapter of the thesis will highlight the experiments that I carried out and contributed to the paper published in 2017 as a co-author (*Journal of Physical Chemistry A*, 2017, 121 (30), 5569–5579). Here, the experiments associated with the adsorption of DMA onto clean or pre-exposed to organics (OA and PC) hematite nanoparticles as a function of different electrolyte such as KCl, KBr and NaBr have been discussed.

The main objective of these experiments are as follows:

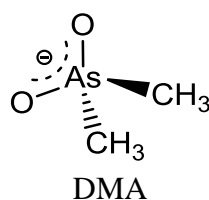
- i) To establish the structure-reactivity relationships from the initial adsorption kinetics upon DMA binding to organics onto the surface of hematite nanoparticles by *in situ* ATR-FTIR.
- ii) Investigate the effect of model organic substituents (such as OA and PC) on Dimethyl arsinate (DMA) binding kinetic onto organic-hematite interface.
- iii) Explore the effect of different electrolyte on DMA binding onto hematite nanoparticles.
- iv) Compare the results that were obtained from the experiments performed by Arthur Situm, a former group member.



Oxalic acid



Pyrocatechol



DMA

3.4 Experimental

3.4.1 Chemicals

The solutions were prepared by dissolving the desired organic compound in 0.01 M KCl (ACS grade, 99.0%+, EMD) solution prepared fresh in 18 M Ω -cm Millipore water and adjusted to pH 7 by using dilute and concentrated HCl (6 N, Ricca Chemical Company) and NaOH (GR ACS, 99.0-100%, EMD) solutions. The concentration of KCl varied for ionic-strength-dependent studies. 0.01 M NaCl and KBr were also used for the ionic-strength-dependent studies. Powder of organic compounds used herein (as received without further purification) include oxalic acid (Oxalic acid dihydrate, 99%+, ACS reagent, Sigma-Aldrich), catechol (99%+, Sigma-Aldrich), and DMA (sodium cacodylate trihydrate, C₂H₆AsO₂Na.3H₂O, 98%, Sigma-Aldrich, used as received). All the solutions were prepared freshly before the start of each experiment and were covered with parafilm until used. Hematite nanoparticles (α -Fe₂O₃, 98%+, US Research Nanomaterials, Inc, batch US3180) were characterized for these experiments to obtain BET surface area (N₂ gas, 54 \pm 5 m²/g, Aveka Inc.), isoelectric point (IEP) (zeta potential titration, 8.45, Aveka Inc.), particle shape and size (TEM Philips C12 at 120 keV, spherical, 39 \pm 11 nm average diameter, Canadian Centre for Electron Microscopy, McMaster University).

3.4.2 Preparation of film on ZnSe ATR crystal

The film on ZnSe ATR crystal was prepared according to the procedure mentioned in section 2.3.3 of Chapter 2, page 11.

3.4.3 ATR-FTIR spectroscopy experiments

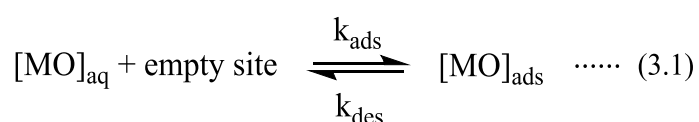
The ATR-FTIR spectroscopy experiments were performed according to the procedure mentioned in section 2.3.4 of Chapter 2, page 11.

3.4.4 Adsorption kinetics

All solutions were flowed at a rate of 2 mL/min through the hematite film using Tygon tubes (0.8 mm I.D., Masterflex) and a compact pump (Masterflex L/S). Single beam ATR-FTIR spectra were collected at 8 cm⁻¹ resolution all through the experiments. Background spectra were collected with 100 average scans by running 0.01 M KCl/KBr/NaCl solutions or Mili-Q H₂O for 90 minutes at pH 7. Then, solutions of OA or PC of known concentrations were passed through the film at the same pH for 80 min. Data were collected as soon as the solution entered the ATR flow cell with spectral averaging of 5 scans for 5 minutes with 0.1 min interval. The adsorption spectra were collected automatically by using a custom-written macros in OMNIC for first 5 min. For rest of the time data were collected manually at 5 min interval with 100 average scans up to 80 min. The software was installed on a PC computer with the following specifications: Dell Optiplex GX620, Intel, ACPI Multiprocessor, and Premium 4 CPU 3.20 GHz with 1 GB RAM. The collection acquisition times were calculated from the time saved by the computer in the file names. Each single beam spectrum was referenced to the last recorded background solution to obtain the absorbance spectrum reported herein. To determine the uncertainty in the measurements, the experiments were repeated at least two times on freshly prepared films under identical conditions

3.4.5 Kinetic modeling (Adsorption)

Macros Basic software was used to obtain a base-line corrected peak height of ATR absorbance spectra. Baseline-corrected peak height measurements were performed to surface complexes, at the wavenumber of specific spectral features, were used as an accurate measurement of surface coverage. The reaction to be analyzed was between aqueous analyte species and empty reactive sites on the surface of the geosorbent film, shown in reaction 3.1.



where [MO] is the concentration of the model organics, k_{ads} is the adsorption rate constant, and k_{des} is the desorption rate constant. The Langmuir adsorption model can be employed to analyze the kinetics and thermodynamics of reaction 3.1. The assumptions within the Langmuir adsorption model describes that a homogeneous surface that is formed is identical with the reactive surface sites. The Langmuir model for adsorption kinetics, shown in equation 3.2, was used to analyze the collected peak heights in order to generate time dependent adsorption kinetic curves.

$$\theta(t) = b(1 - e^{-r_{obs}.t}) \dots \dots \dots (3.2)$$

$$\text{where, } b = k_{ads1}[MO]_{aq}/r_{obs1}$$

$$\text{and, } r_{obs} = k_{ads}[MO] + k_{des}$$

Here, $\theta(t)$ is the measure of surface coverage which is related to the absorbance as equation 3.3. Expansion of θ term in equation 3.3 can be obtained by using the measurements of surface coverage that produces equation 4 that provides a measurement of baseline-corrected peak height absorbance.

$$\theta = A/A_{max} \dots \dots \dots (3.3)$$

$$A = b'(1 - e^{-r_{obs}.t}) \dots \dots \dots (3.4)$$

$$\text{where, } b' = A_{max}.b$$

Equation 3.4 can be obtained then linearized to produce equation 3.5 with b' being a collection of constants equal to the absorbance in the plateau region of the adsorption kinetic curve.

$$\ln(1-A/b') = -r_{obs}.t \dots \dots \dots (3.5)$$

By using equation 3.5, r_{obs} is equal to the slope of the least-squared fit of $\ln(1- A/b')$ plotted against time (min) of adsorption. Thus, the Langmuir adsorption kinetic model allows for the plotting of r_{obs} against aqueous analyte concentration to extract k_{ads} using equation 3.6.

$$r_{obs} = k_{ads}[MO]_{aq} + k_{des} \dots\dots(3.6)$$

However, using equation 3.2, some of the experimental data resulted in poor fit. In order to get better fit, the following equation 3.7, a two-exponential, 2-site model was used that suggested the best fit for two kinetic regions for the adsorption of DMA.³¹

$$\theta_{(total)t} = b_1(1 - e^{-r_{obs1} \cdot t}) + b_2(1 - e^{-r_{obs2} \cdot t}) \dots \dots\dots (3.7)$$

3.4.6 Desorption kinetics

DMA and Sodium Arsenate were used as a desorbing agent for all the desorption part of the experiments. Collection of spectra started as the solution of the desorbing agent entered the ATR flow all containing the same hematite film previously exposed to OA or PC solutions for 80 min. Initially, spectra were collected automatically by using a custom written macros in OMNIC for 10 min with 0.25 min interval and 25 scans. Then the data were collected manually at 5 min interval with 100 average scans up to 80 min. Single beam ATR spectra were collected and reprocessed against the last spectrum collected for the background solution for obtaining the absorbance spectra as described in the previous section for the adsorption experiments. Since desorption of surface arsenicals due to flowing aqueous hydrogen phosphate would occur concurrently with the adsorption of phosphate species, the control experiments were carried out for the adsorption of aqueous hydrogen phosphate on freshly prepared films at pH 7.

3.4.7 Kinetic modeling (Desorption)

Desorption of model organics from the surface by the adsorption of aqueous arsenic species can be shown as reaction 3.8 and described by the Langmuir kinetic desorption model shown in equation 3.9.



$\theta(t)$ and θ_o are converted to absorbance values and linearized to obtained equation 3.10.

$$\theta(t) = \theta_o e^{-k'_{des} \cdot t} \dots\dots (3.9)$$

Where, $\theta = A/A_{\max}$ and $\theta_o = A_o/A_{\max}$

and, $k'_{des} = k_{des} \cdot [As]_{aq}$

$$\ln(A/A_o) = -k'_{des} \cdot t \quad \dots\dots(3.10)$$

Here, A_o is the initial absorbance before the start of desorption. The initial observed desorption rate can be extracted by plotting $\ln(A/A_o)$ vs desorption time (min) with the initial observed desorption being equal to the slope of the least-squared fit.

Using equation 3.9, the experimental data resulted in poor fit for desorption kinetics since the equation does not consider the possibility of readsorption of DMA. However, when the possibility for readsorption is involved in the derivation, the modified Langmuir desorption model becomes as equation 3.11.³¹

$$\theta_{(t)} = \frac{(k'_{des} \cdot \theta_o - k'_{ads}) \cdot e^{-k'_{des} \cdot t} + k'_{ads}}{k'_{des}} \dots \dots \dots (3.11)$$

where $k'_{des} = k_{des} \cdot [A(aq)]$ and $k'_{ads} = k_{ads} \cdot [DMA(aq)]$

3.5 Results and discussion

The results discussed herein have been divided into two categories: Adsorption and Desorption Kinetics. Section 3.4.1 focuses on adsorption kinetics of three different types of experiments. (a) Adsorption kinetics of model organics on hematite nanoparticle; (b) Adsorption kinetics of arsenicals on hematite nanoparticle; and (c) Adsorption of arsenicals on hematite containing model organics. Section 3.4.2 will be highlighting desorption kinetics of model organics by arsenicals.

3.5.1 Adsorption kinetics

(a) Adsorption kinetics of model organics on hematite nanoparticle

Adsorption kinetic experiments were performed using oxalate (OA) and pyrocatechol (PC) onto unreacted hematite films at pH 7 in H₂O, as well as with three different electrolytes such

as KCl, NaCl and KBr. Spectra obtained from the experiments with oxalate as a model organic compound in different electrolytes are shown in Figure 3.6.

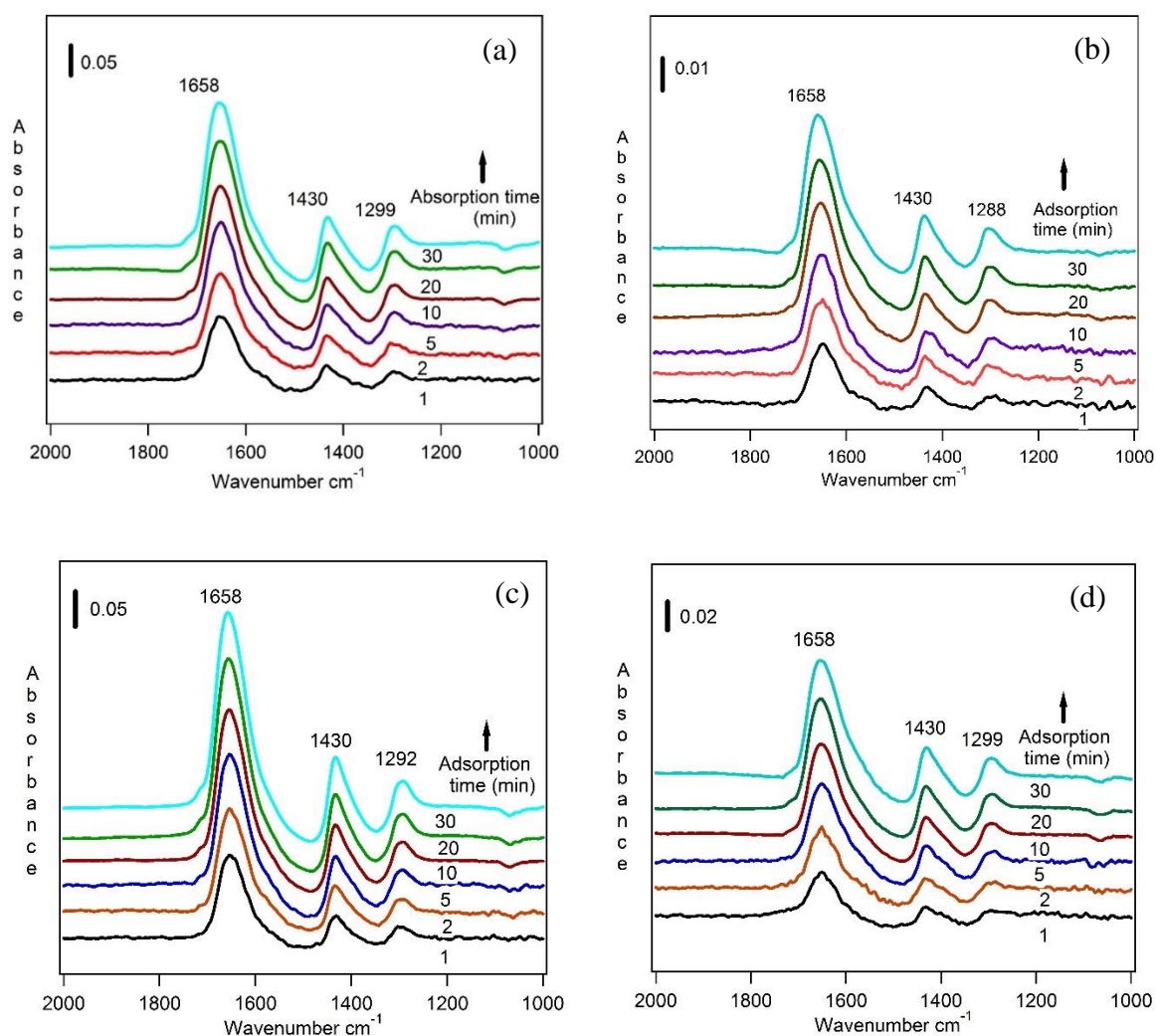


Figure 3.6 Absorbance spectra of oxalate (1.0 mM) onto a clean hematite (6 mg) film at pH 7, $I = 10$ mM (a) NaCl (b) KCl (c) KBr and (d) H_2O at room temperature. ATR-FTIR absorbance spectra of adsorbed oxalate were collected as a function of time.

Oxalate adsorption spectra onto hematite shows band at 1658, 1430 and 1288 cm^{-1} . Peak at 1658 and 1430 cm^{-1} are assigned to asymmetric and symmetric stretching modes of $-CO_2$ functional groups, whereas peak at 1288 cm^{-1} assigned to bending mode $\nu(CO_2)$ as previously reported by Situm *et al.*²⁶ The peak heights at 1658 cm^{-1} for oxalate were used to obtain baseline corrected adsorption kinetic curves as a function of time for each experiment. The baseline corrected adsorption kinetic curves for oxalate on unreacted hematite nanoparticle H_2O

and three different electrolytes ($I = 10$ mM for KCl, NaCl and KBr) are shown in Figure 3.7. Lines through the data represent 2-site Langmuir adsorption kinetic model using equation 3.7. The equilibrium between the aqueous phase organics and the surface of hematite nanoparticles is reached by the 80 min adsorption time.

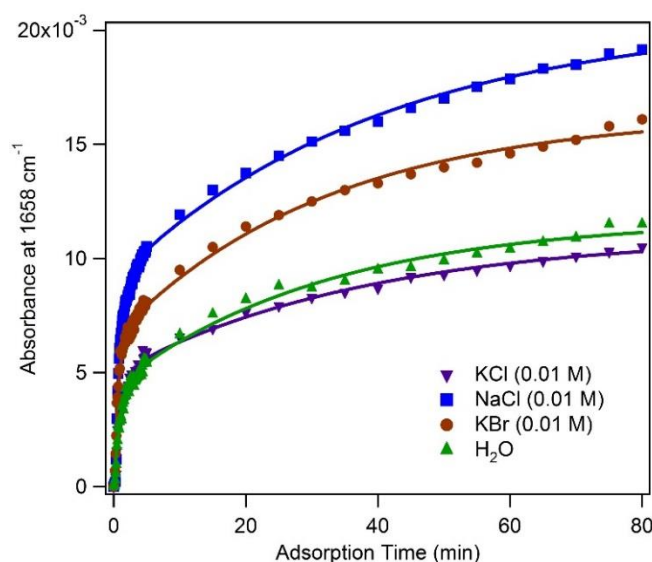


Figure 3.7 Adsorption kinetic curves generated from the baseline-corrected ATR-FTIR absorbances for oxalate adsorbed on to a clean hematite (6 mg) film at pH 7 with H₂O and three different electrolytes ($I = 10$ mM for KCl, NaCl and KBr) and a 2 mL/min flow rate at room temperature. (Data points represent the average of four experiments. Error bars have been removed for clarity).

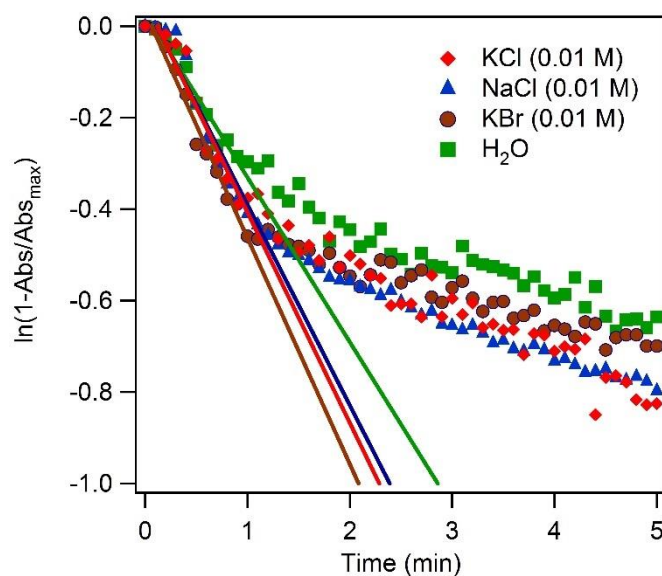


Figure 3.8 Linearized adsorption kinetics curves of oxalate on 6 mg hematite film with at pH 7 with H₂O and three different electrolytes ($I = 10$ mM for KCl, NaCl and KBr). $\ln(1 - \text{Abs}(\text{Org})/\text{Abs}(\text{OrgMax}))$ with $\text{Abs}(\text{Org})$ corresponding the band measured for oxalate. (Data

points represent the average of two to four experiments and error bars have been removed for clarity.)

Linearization of adsorption kinetic curves (Figure 3.7) of oxalate was done and shown in Figure 3.8. The linearization shown in Figure 3.8 was obtained by taking a natural log of oxalate, a model organic peak heights absorbances normalized against the maximum peak height absorbance measured at 80 minutes adsorption time (equation 4).

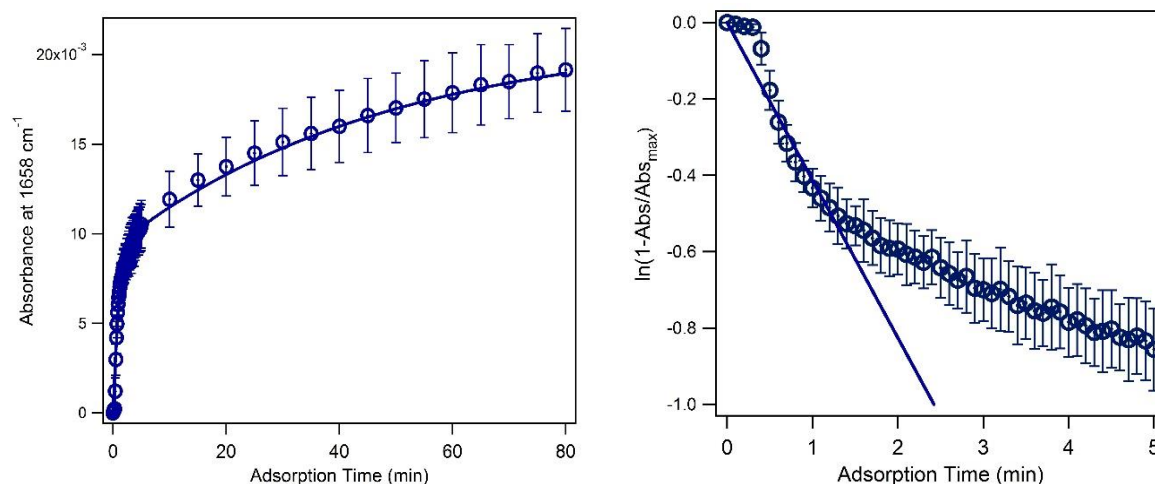


Figure 3.9 Adsorption kinetic curves (left) generated from the baseline-corrected ATR-FTIR absorbances for oxalate (1.0 mM) adsorbed onto a clean hematite (6 mg) film at pH 7, $I = 10$ mM NaCl, and a 2 mL/min flow rate at room temperature. Linearized adsorption kinetic curve of oxalate (right). Data points represent the average of four experiments. Error bars are $\pm\sigma$

Figure 3.9 shows an example of the least-squared fits added to linearized oxalate, a model organic adsorption kinetics in Figure 3.9 are predicted to have slopes equal to the observed initial rates of adsorption (r_{obs1}) according to the kinetic form of the Langmuir adsorption 2-site model described in section 3.3.5 in equation 3.7. Similar types of data were collected for model organic pyrocatechol (PC) on unreacted hematite films at pH 7 in H₂O and KCl (0.01 M). Spectra obtained from the experiments with pyrocatechol as a model organic compound are shown in Figure 3.10.

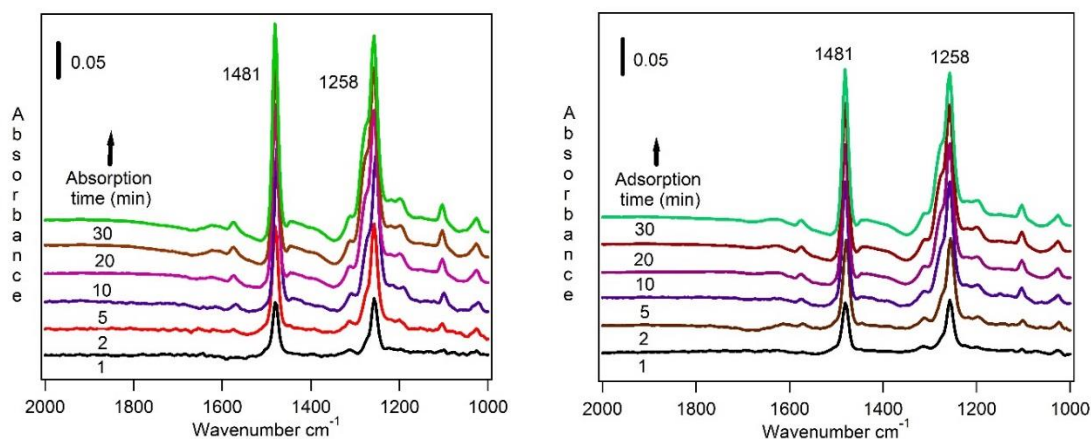


Figure 3.10 Adsorption of pyrocatechol (1.0 mM) onto a clean hematite (6 mg) film at pH 7, $I = 10$ mM, H_2O (left) and KCl (right) at room temperature. ATR-FTIR absorbance spectra of adsorbed oxalate were collected as a function of time.

Pyrocatechol adsorption spectra onto hematite shows intense band at 1481 and 1258 cm^{-1} , along with giving rise to a shoulder around 1281 cm^{-1} . It has been reported²⁶ as an inner-sphere complex formation, and the spectral features are assigned to $\nu(COFe)$. The peak heights at 1258 cm^{-1} for pyrocatechol were used to generate base-lined corrected adsorption kinetic curves as a function of time for each experiment. The base-line corrected adsorption kinetic curves for pyrocatechol on unreacted hematite nanoparticle H_2O and KCl (0.01 M) are shown in Figure 3.11. Lines through the data represent 2-site Langmuir adsorption kinetic model using equation 3.7. The equilibrium between the aqueous phase organics and the surface of hematite nanoparticle reached by the 80 min adsorption time.

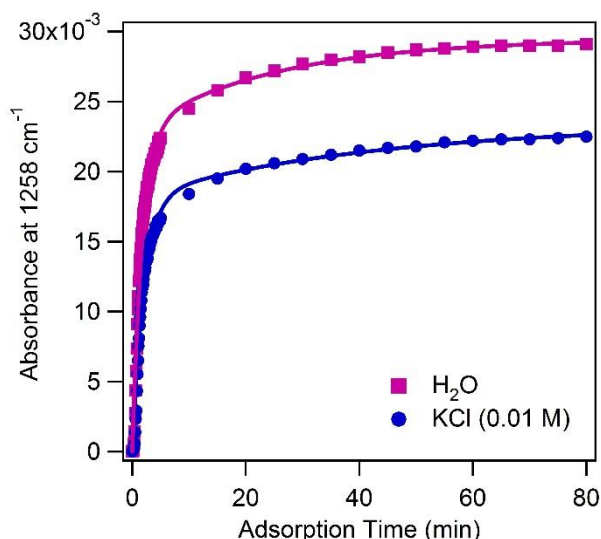


Figure 3.11 Adsorption kinetic curves generated from the baseline-corrected ATR-FTIR absorbances for pyrocatechol adsorbed on to a clean hematite (6 mg) film at pH 7 with a 2 mL/min flow rate at room temperature. (Data points represent the average of four experiments. Error bars have been removed for clarity)

Linearization of adsorption kinetic curves (Figure 3.10) of pyrocatechol was obtained and shown in Figure 3.12.

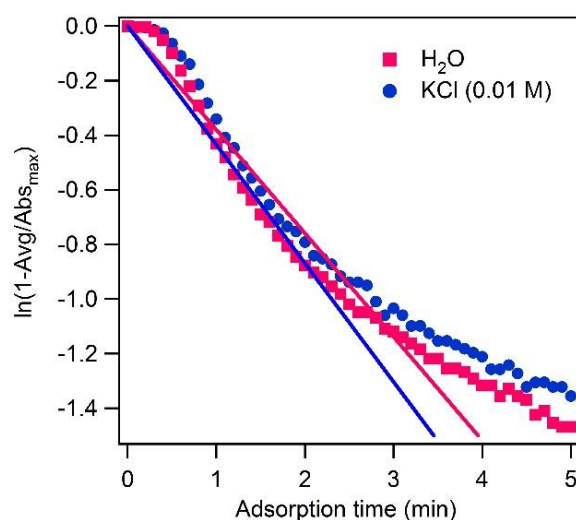


Figure 3.12 Linearized adsorption kinetics of pyrocatechol on 6 mg hematite film with at pH 7. $\ln(1-\text{Abs}(\text{Org})/\text{Abs}(\text{OrgMax}))$ with $\text{Abs}(\text{Org})$ corresponding the band measured for pyrocatechol. (Data points represent the average of two experiments and error bars have been removed for clarity.)

The linearized adsorption kinetic curves in Figure 3.12 was obtained by taking a natural log of pyrocatechol, a model organic peak heights absorbances normalized against the maximum peak

height absorbance measured at 80 minutes adsorption time (equation 4). Initial observed rates of model organic adsorption to unreacted hematite nanoparticles are summarized in Table 3.2.

Table 3.2 Linearized first-order observed adsorption rates (min^{-1}) at various ionic strength conditions of model organics (oxalate and pyrocatechol) on hematite film.

Surface	[Organics] (mM)	Adsorption rates ($\text{mM}^{-1}.\text{min}^{-1}$)			
		No electrolyte	0.01M NaCl	0.01 M KCl	0.01 M KBr
OA/hematite	1.0	0.12 (± 0.002)	0.17 (± 0.01)	0.19 (± 0.01)	0.23 (± 0.005)
PC/hematite	1.0	0.32 (± 0.03)		0.39 (± 0.01)	

The observed initial rates of model organic adsorption shown in Table 3.2 show increase in initial rates for absorbance of oxalate in presence of electrolyte. However, the effect of electrolyte on the initial rates of adsorption of pyrocatechol is insignificant. This increase in adsorption rates for the charged oxalate species is attributed to the presence of electrolytes and the surface of hematite. A charged double layer of electrolytes the surface of hematite should increase the adsorption of the negatively charged species because of electrostatic attraction to sodium and potassium ions. These results agree with the formation of surface complexes of model organics on hematite nanoparticles. The adsorption rate of pyrocatechol on hematite nanoparticles supports the assignment of a neutral inner-sphere complex as shown in figure 2.11 while the enhancing effect of oxalate adsorption supports the assignment of charged surface complexes.

(b) Adsorption kinetics of arsenicals on hematite nanoparticle

Adsorption kinetics experiments of arsenical compounds were performed on clean hematite nanoparticle. Figure 3.13 shows the adsorption spectra of DMA onto clean hematite surface in NaCl, KBr and H₂O.

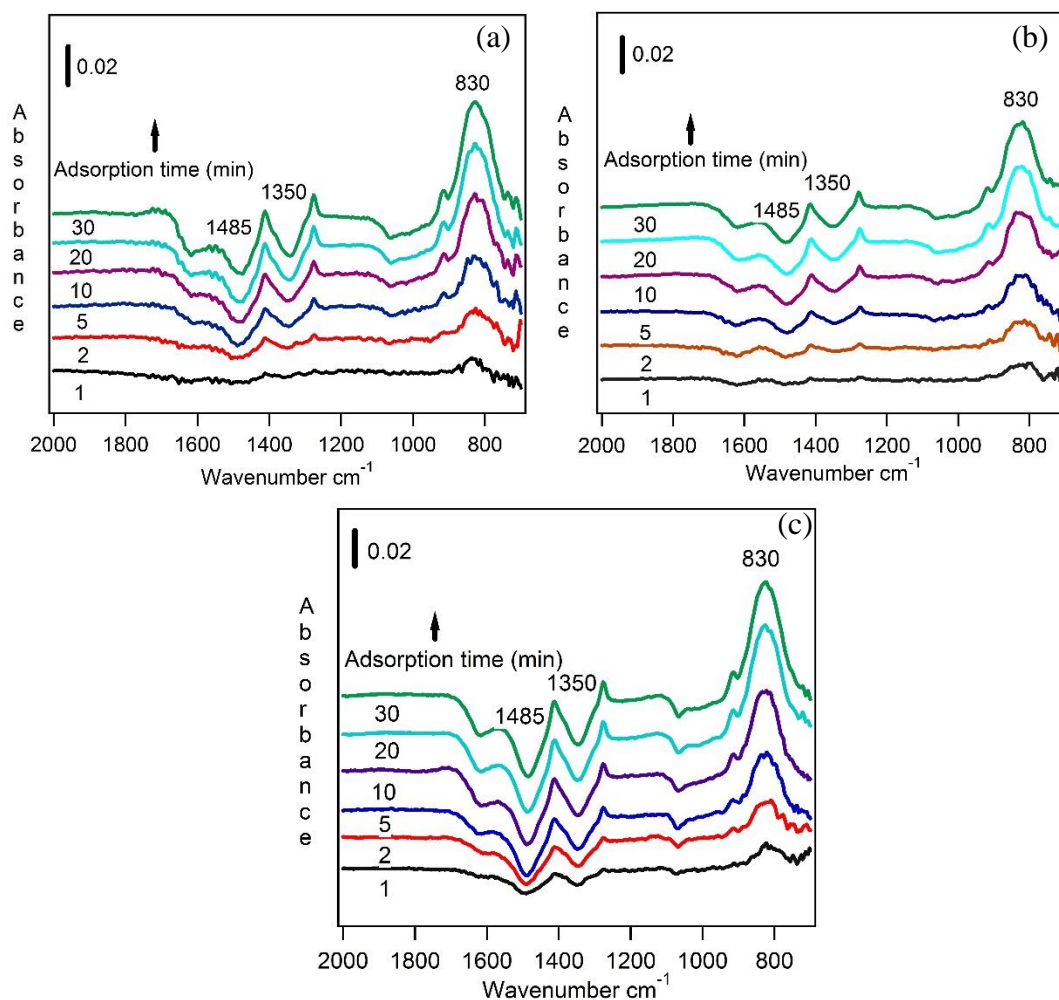


Figure 3.13 ATR-FTIR absorbance spectra of 1.0 mM DMA on to a clean, hematite (6 mg) film at pH 7, I = 10 mM (a) NaCl (b) KBr and (c) H₂O with a 2 mL/min flow rate at room temperature.

DMA adsorption spectra onto hematite shows band at 830 cm⁻¹ and two negative features at 1485 and 1350 cm⁻¹. The band at 830 cm⁻¹ is assigned to the As-O vibrations as reported previously by Sabur *et al.*²⁷ and associated with the outer-sphere complexation of DMA with the surface hematite. The negative features at 1485 and 1350 cm⁻¹ are associated with the loss of carbonate from the hematite surface.²⁸ The adsorption of DMA to the surface of hematite causes the loss of carbonate as carbonate competes with reactive sites on the surface of

hematite. The peak heights at 830 cm^{-1} for DMA were used to obtain base-lined corrected adsorption kinetic curves as a function of time for each experiment. The base-line corrected adsorption kinetic curves for oxalate on unreacted hematite nanoparticle H_2O and two different electrolytes NaCl and KBr are shown in Figure 3.14. Lines through the data represent 2-site Langmuir adsorption kinetic model using equation 3.7. The equilibrium between the aqueous phase DMA and the surface of hematite nanoparticle was reached by the 80 min adsorption time.

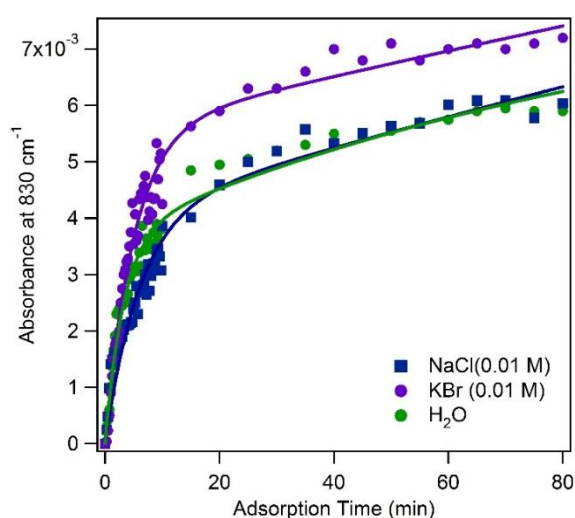


Figure 3.14 Baseline-corrected adsorption kinetics of 1.0 mM DMA onto to a clean, hematite (6 mg) film at pH 7 with a 2 mL/min flow rate at room temperature. (Data points represent the average of two experiments. Error bars have been removed for clarity).

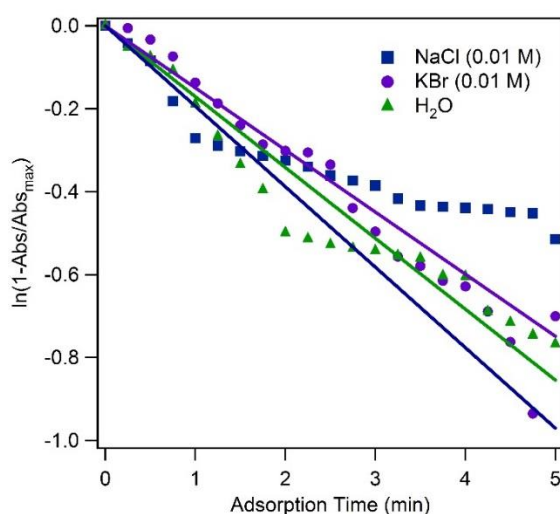


Figure 3.15 Linearized adsorption kinetics of DMA on 6 mg hematite film with at pH 7. $\ln(1 - \text{Abs}(A_s)/\text{Abs}(A_{s_{\text{max}}}))$ with $\text{Abs}(A_s)$ corresponding the band measured for DMA. (Data points represent the average of two experiments and error bars have been removed for clarity).

The use of these kinetic curves comes from their ability to be analyzed by a kinetic model such as the kinetic form of the Langmuir adsorption kinetic model to extract rates of adsorption as shown (Figure 3.16). Figure 3.17 shows an example of the least-squared fits added to linearized DMA, a model organic adsorption kinetics in Figure 3.16 are predicted to have slopes equal to the observed initial rates of adsorption (robs1) according to the kinetic form of the Langmuir adsorption kinetic model described in section 3.3.5.

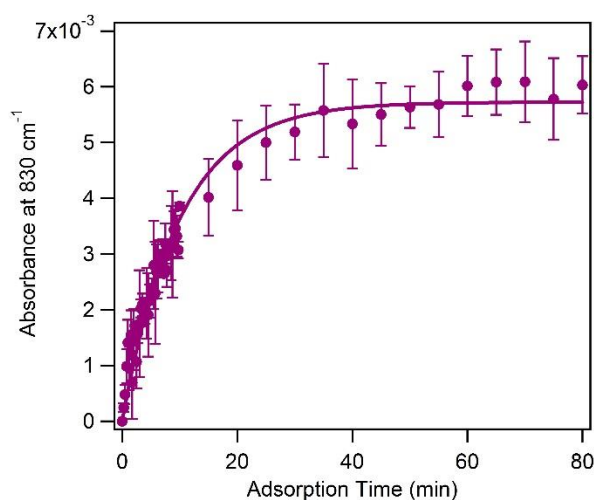


Figure 3.16 Baseline-corrected adsorption kinetics of 1.0 mM DMA onto a clean, hematite (6 mg) film at pH 7 with a 2 mL/min flow rate at room temperature. Data points represent the average of two experiments. Error bars are $\pm\sigma$.

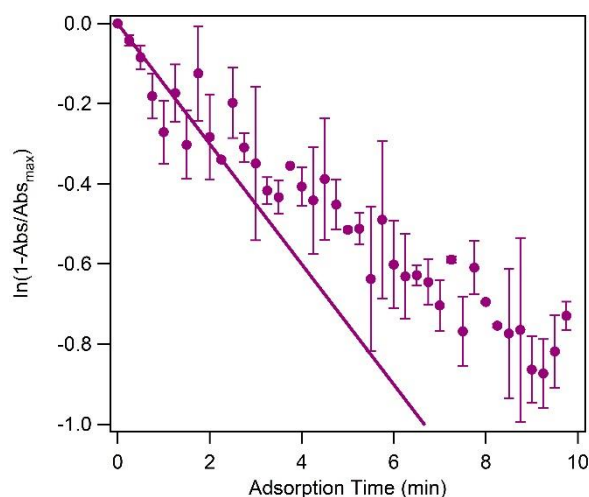


Figure 3.17 Linearized adsorption kinetics of 1.0 mM DMA on 6 mg hematite film with at pH 7 in NaCl (0.01 M). $\ln(1 - \text{Abs}(A_s)/\text{Abs}(A_{s_{\max}}))$ with $\text{Abs}(A_s)$ corresponding the band measured for DMA. (Data points represent the average of two to experiments and error bars $\pm\sigma$.)

(c) Adsorption of arsenicals on hematite containing model organics

Experiments were performed to study the adsorption kinetics of arsenicals onto hematite pre-exposed to the model organics. Figure 3.18 shows ATR-FTIR absorbance spectra of DMA onto a saturated oxalate and pyrocatechol model organics hematite film at pH 7 in H₂O, NaCl, KBr and KCl, respectively.

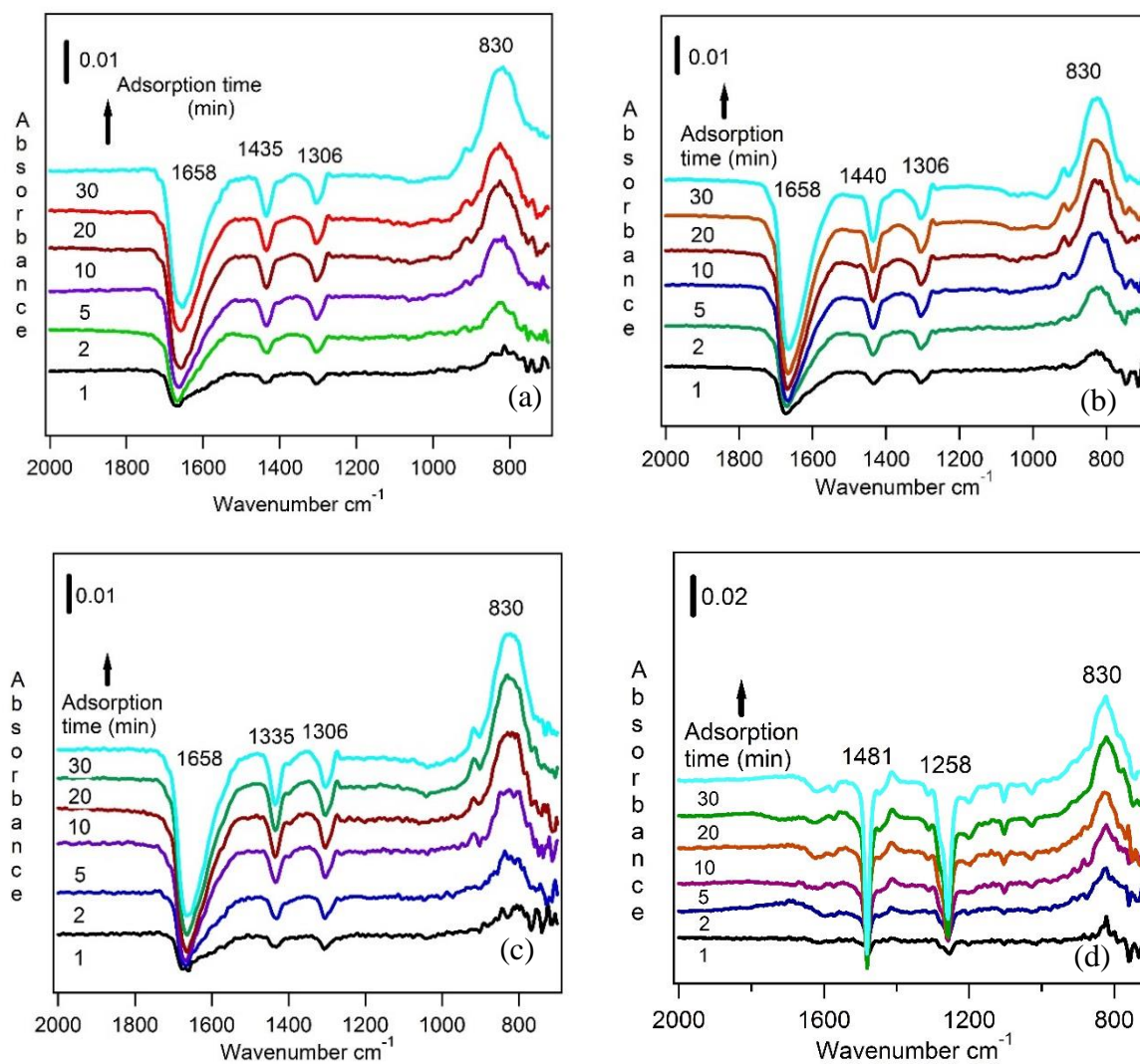


Figure 3.18 ATR-FTIR absorbance spectra of 1.0 mM DMA on to hematite (6 mg) film pre-exposed to oxalate at pH 7, I = 10 Mm (a) NaCl (b) KBr and (c) H₂O and (d) 1.0 mM PC onto hematite in KCl solution with a 2 mL/min flow rate at room temperature.

The spectral range between 1000 and 750 cm⁻¹ contains positive absorbance features assigned to the stretching vibrations of As-O bonds in adsorbed DMA. According to Sabur *et al.*,²⁹ this spectral features shown in Figure 3.18 are attributed to the formation of a mix of monodentate

and outer-sphere DMA complexes. The ATR-FTIR spectra were collected as a function of time (1, 2, 5, 10, 20, 30 min) upon flowing 1 mM DMA in on the hematite nanoparticles with adsorbed oxalate (OA) and pyrocatechol. Solutions were prepared in NaCl (10 mM), KBr (10 mM) and H₂O at pH 7 for oxalate and KCl (10 mM) for pyrocatechol. The spectra were obtained by referencing to the spectrum collected after 80 min of flowing the oxalate and pyrocatechol compounds, respectively.

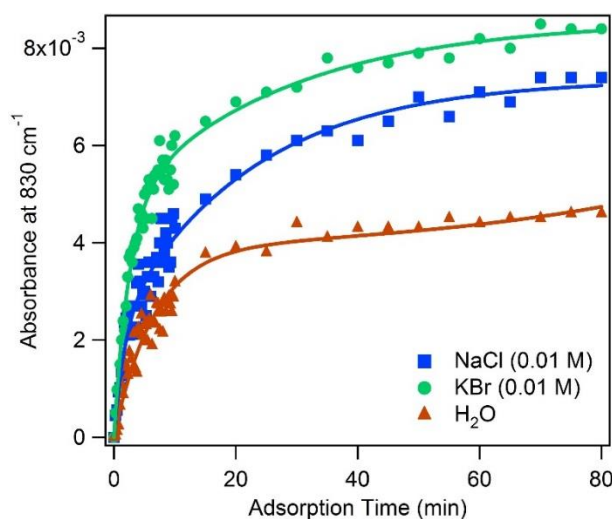


Figure 3.19 Kinetic curve of 1.0 mM DMA on to hematite (6 mg) film pre-exposed to OA at pH 7, I = 10 Mm (a) NaCl (b) KBr and (c) H₂O with a 2 mL/min flow rate at room temperature. (Data points represent the average of two experiments and error bars have been removed for clarity).

The spectral range between 1800 and 1000 cm⁻¹ contains negative absorbance features assigned to the symmetric and asymmetric stretching vibration of -CO₂ functional groups, $\nu(\text{CO}_2)$, and $\nu(\text{CO}_2\text{Fe})$ in oxalate and $\nu(\text{COFe})$ in pyrocatechol. Band at 830 cm⁻¹ were used to create baseline-corrected kinetic curves for DMA adsorption on hematite surface as a function of adsorption time and shown in Figure 3.19. Lines through the data represent 2-site Langmuir adsorption kinetic model using equation 3.7.

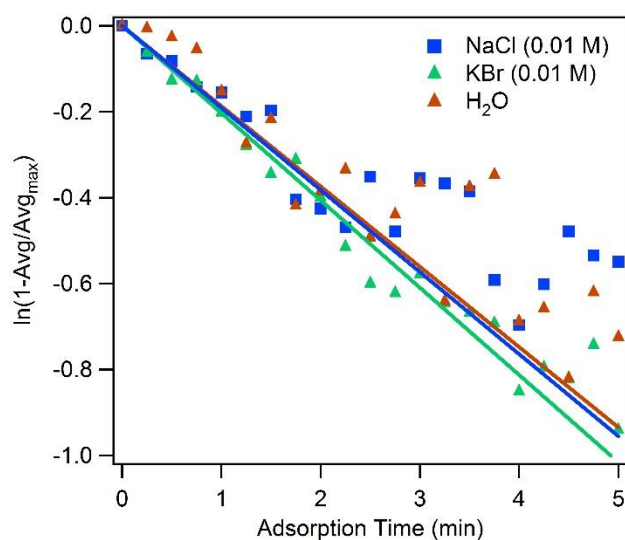


Figure 3.20 Linearized adsorption kinetics of 1.0 mM DMA on 6 mg hematite film with at pH 7. $\ln(1-\text{Abs}(\text{As})/\text{Abs}(\text{As}_{\text{Max}}))$ with $\text{Abs}(\text{As})$ corresponding the band measured for DMA. (Data points represent the average of two experiments and error bars have been removed for clarity)

Linearization of adsorption kinetic curves (Figure 3.18) of DMA was done and shown in Figure 3.20. The linearization shown in Figure 3.20 was obtained by taking a natural log of DMA peak heights absorbances normalized against the maximum peak height absorbance measured at 80 minutes adsorption time (equation 4). Similar types of analysis were performed for pyrocatechol to obtain initial adsorption kinetic for DMA. Table 3.3 contains the initial adsorption kinetics of DMA onto hematite clean and pre-exposed to model organics (OA and PC).

Table 3.3 DMA initial adsorption rate on different surfaces, with and without electrolytes at pH 7 at 2 mL/min flow rate

Surface	DMA initial Adsorption Kinetics			
	No electrolyte	0.01M KCl	0.01 M NaCl	0.01 M KBr
Clean hematite	0.03 (± 0.002)	0.06 (± 0.01)	0.035 (± 0.005)	0.015 (± 0.002)
OA/hematite	0.02 (± 0.002)	0.11 (± 0.01)	0.056 (± 0.01)	0.04 (± 0.005)
PC/hematite	0.10 (± 0.01)

3.5.2 Desorption Kinetics of model organic matter on hematite

Arsenicals were treated with hematite nanoparticles, pre-exposed to model organics, in order to study the effect that organic functional groups have on the kinetics of arsenical adsorption. Information obtained from model organic desorption from hematite nanoparticles can be utilized to support the assigned surface complexes of model organics on hematite. It has been reported by previous studies that arsenate forms a strong inner-sphere bidentate binuclear complex with the surface of hematite nanoparticles, whereas DMA forms an outer-sphere complex.^{30,31}

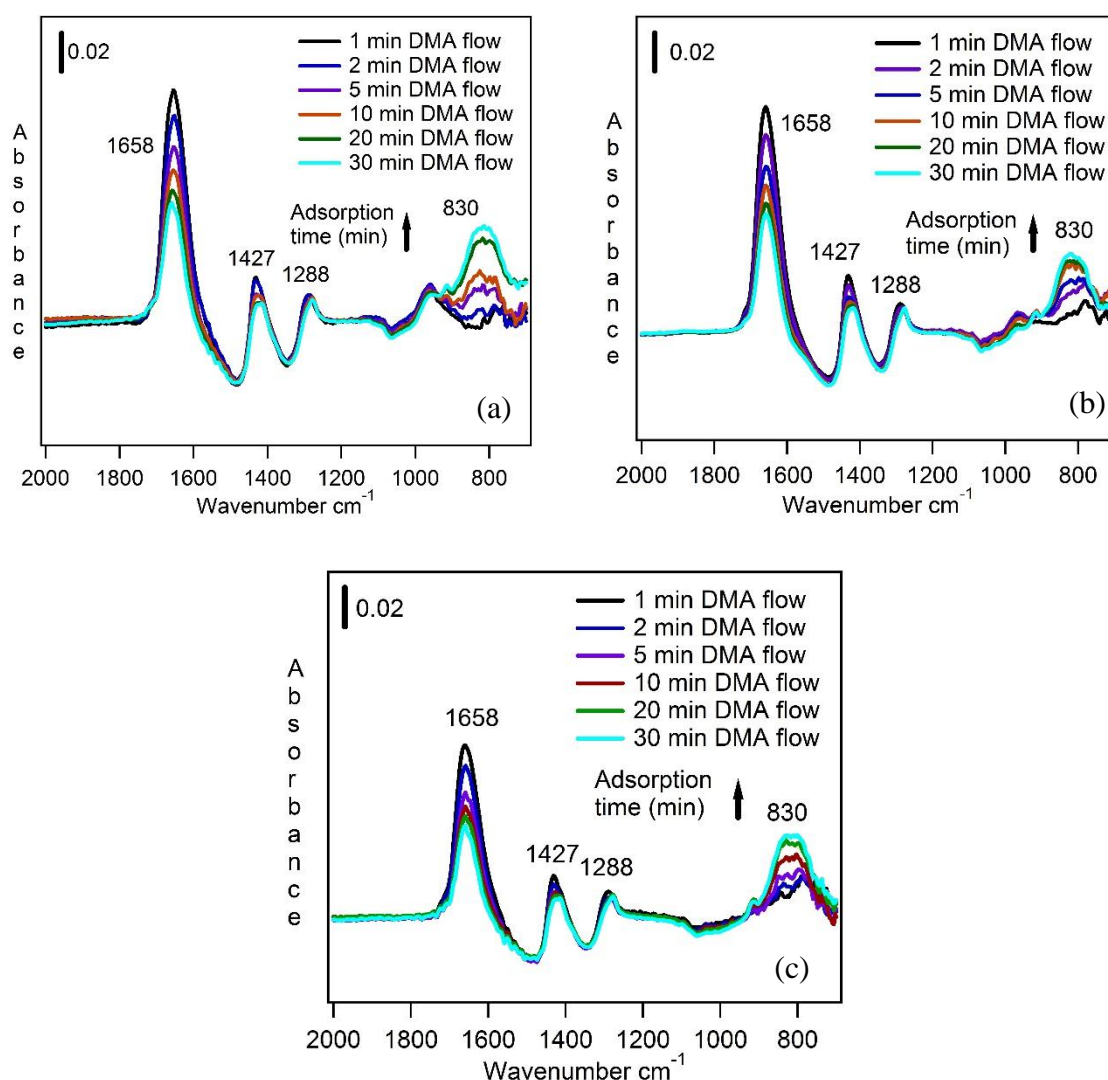


Figure 3.21 ATR-FTIR absorbance spectra correspond to the oxalate desorption from hematite (6 mg) film at pH 7 in 10 mM (a) NaCl (b) KBr and (c) H₂O at room temperature, by the flowing of 1.0 mM DMA.

Desorption kinetic experiments of oxalate from hematite nanoparticles were conducted using DMA in NaCl (0.1 M), KBr (0.01) and H₂O solution at pH 7. Spectra obtained from the experiments are shown in Figure 3.21. The spectra shown in Figure 3.21 were obtained by referencing to the spectrum collected for dry hematite nanoparticle film. The ATR-FTIR spectra were collected as a function of time (1, 2, 5, 10, 20, 30 min) upon flowing 1.0 mM DMA in on the hematite nanoparticles with adsorbed oxalate (OA). The spectral range between 1800 and 1000 cm⁻¹ contains absorption band features assigned to the symmetric and asymmetric stretching vibration of -CO₂ functional groups, $\nu(\text{CO}_2)$, and $\nu(\text{CO}_2\text{Fe})$ in oxalate. As the flow time increases, peak at 830 cm⁻¹ for DMA increases, whereas the intensity of OA peaks at 1658, 1427 and 1288 cm⁻¹ decreases as a function of time. Using baseline-corrected peak height absorbances at 1658 cm⁻¹ was plotted as a function of desorption time, kinetic curve for oxalate desorption from hematite nanoparticles was generated and a sample desorption kinetic curve are shown in Figure 3.22. Line through the data represent modified Langmuir desorption kinetic model using equation 3.11.

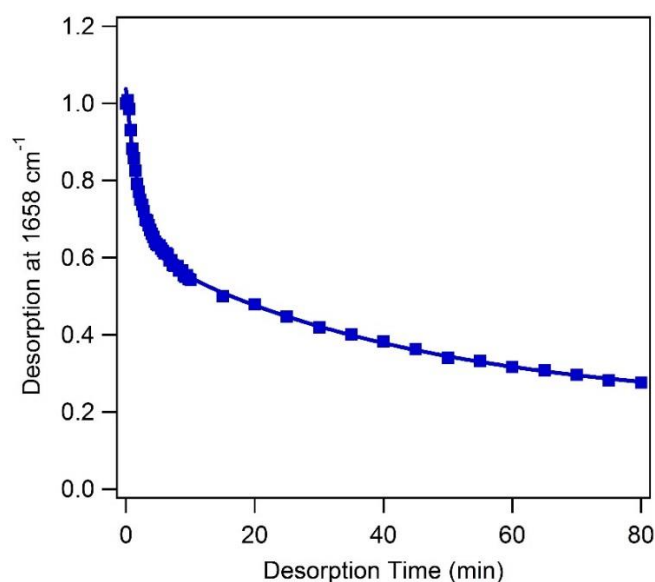


Figure 3.22 (a) Desorption kinetic curve generated from the baseline-corrected ATR-FTIR absorbances of oxalate from hematite (6 mg) nanoparticles at pH 7 in H₂O and a 2 mL/min flow rate at room temperature, by 1.0 mM DMA. Data points represent the average of two experiments. Error bars are $\pm\sigma$.

Figure 3.23 shows the linearized oxalate desorption kinetic curve.

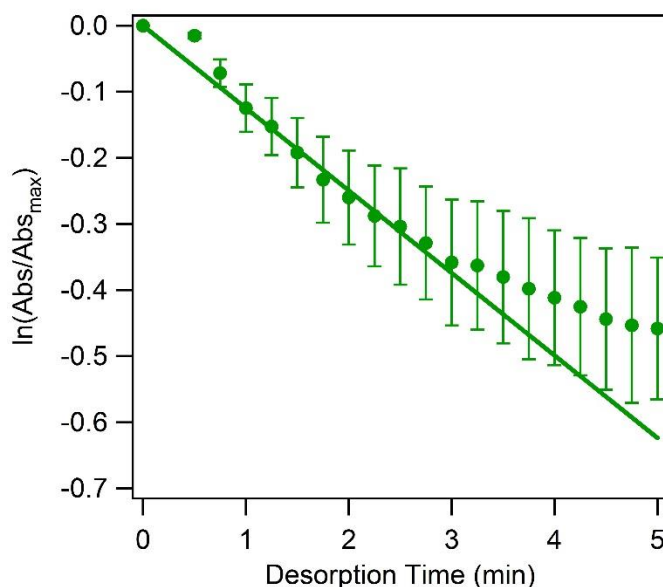


Figure 3.23 Linearized desorption kinetic curve for oxalate on the hematite film at pH 7 in H₂O. The figure shows $\ln(A(\text{organic})/A_{\text{max}}(\text{organic}))$ with $A(\text{organic})$ corresponds to absorbance at 1658 cm^{-1} for oxalate. Data points represent the average of two to four experiments and error bars $\pm\sigma$.

Linearized desorption kinetics were obtained in a similar way to the linearized adsorption kinetics by taking the natural log of baseline-corrected peak height absorbance values, normalized against the initial baseline-corrected peak height absorbance at 0 min desorption time (equation 9). Similar types of analysis were performed for pyrocatechol to obtain the desorption kinetic curve for DMA.

3.6 Conclusion

In this study, the adsorption kinetics of DMA with hematite nanoparticles pre-exposed to two types of low molecular weight organics such as oxalate, and pyrocatechol were conducted using ATR-FTIR. The results demonstrate that how the differences in the structure of arsenicals and surface organics, and the type of electrolyte present in solution affect the binding of arsenicals with hematite nanoparticles. Particularly, the negatively charged carboxylate and hydrophobic phenyl groups influence amounts and rates of arsenicals adsorption on hematite nanoparticles, the type of electrolytes affects the adsorption rate of DMA in the presence of oxalate on the surface, and the extent of organics retention by hematite nanoparticles is influenced by the type of the desorbing agent. NOM greatly influence As sorption by

interacting with mineral surfaces and consequently may play a significant role in the release of As from soils into the groundwater. The presence of NOM can enhance As release mainly through competition for available adsorption sites, forming aqueous complexes, and changing the redox chemistry of site surfaces and As species. Instead, organics can also reduce As mobility by serving as a binding agent and by forming insoluble complexes, especially when saturated with metal cations. These findings are important in advancing the understanding of the fate and transport cycle of As in the environment, and give insights for the control of As mobility. Given the ubiquity of organic-metal oxide interfaces in environmental systems, these results are significant since these studies highlight that *in situ* flow mode and time dependent spectroscopic experiments can amplify trends and molecular-level processes otherwise missed in bulk batch adsorption experiments.

3.7 References

- (1) Martin, R.; Dowling, K.; Pearce, D.; Sillitoe, J.; Florentine, S. Health Effects Associated with Inhalation of Airborne Arsenic Arising from Mining Operations. *Geosciences* **2014**, *4* (3), 128–175.
- (2) Ritter, K.; Aiken, G. R.; Ranville, J. F.; Bauer, M.; Macalady, D. L. Evidence for the Aquatic Binding of Arsenate by Natural Organic Matter - Suspended Fe(III) - *Environ. Sci. Technol.*, **2006**, *40* (17), 5380–5387.
- (3) Sánchez-Rodas, D.; Sánchez de la Campa, A. M.; de la Rosa, J. D.; Oliveira, V.; Gómez-Ariza, J. L.; Querol, X.; Alastuey, A. Arsenic Speciation of Atmospheric Particulate Matter (PM10) in an Industrialised Urban Site in Southwestern Spain. *Chemosphere* **2007**, *66* (8), 1485–1493.
- (4) Bauer, M.; Fulda, B.; Blodau, C. Groundwater Derived Arsenic in High Carbonate Wetland Soils: Sources, Sinks, and Mobility. *Sci. Total Environ.* **2008**, *401* (1–3), 109–

- 120.
- (5) Simeoni, M. A.; Batts, B. D.; McRae, C. Effect of Groundwater Fulvic Acid on the Adsorption of Arsenate by Ferrihydrite and Gibbsite. *Appl. Geochemistry* **2003**, *18* (10), 1507–1515.
 - (6) Mudhoo, A.; Sharma, S. K.; Garg, V. K.; Tseng, C.-H. Arsenic: An Overview of Applications, Health, and Environmental Concerns and Removal Processes. *Crit. Rev. Environ. Sci. Technol.* **2011**, *41* (5), 435–519.
 - (7) Yang, G.; Ma, L.; Xu, D.; Li, J.; He, T.; Liu, L.; Jia, H.; Zhang, Y.; Chen, Y.; Chai, Z. Levels and Speciation of Arsenic in the Atmosphere in Beijing, China. *Chemosphere* **2012**, *87* (8), 845–850.
 - (8) Dobran, S.; Zagury, G. J. Arsenic Speciation and Mobilization in CCA-Contaminated Soils: Influence of Organic Matter Content. *Sci. Total Environ.* **2006**, *364* (1–3), 239–250.
 - (9) Lin, H. T.; Wang, M. C.; Li, G. C. Complexation of Arsenate with Humic Substance in Water Extract of Compost. *Chemosphere* **2004**, *56* (11), 1105–1112.
 - (10) Mikutta, C.; Kretzschmar, R. Spectroscopic Evidence for Ternary Complex Formation between Arsenate and Ferric Iron Complexes of Humic Substances. *Environ. Sci. Technol.* **2011**, *45*, 9550–9557.
 - (11) Chilakapati, J.; Wallace, K.; Ren, H.; Fricke, M.; Bailey, K.; Ward, W.; Creed, J.; Kitchin, K. Genome-Wide Analysis of BEAS-2B Cells Exposed to Trivalent Arsenicals and Dimethylthioarsinic Acid. *Toxicology* **2010**, *268* (1–2), 31–39.
 - (12) Dombrowski, P. M.; Long, W.; Farley, K. J.; Mahony, J. D.; Capitani, J. F.; Di Toro, D. M. Thermodynamic Analysis of Arsenic Methylation. *Environ. Sci. Technol.* **2005**, *39*

- (7), 2169–2176.
- (13) Borch, T.; Larese-casanova, P.; Kappler, A. Redox Transformation of Arsenic by Fe(II)- Activated Goethite (α -FeOOH) Redox Transformation of Arsenic by Fe(II)- Activated Goethite (γ -FeOOH). **2010**, *44*, 102–108.
- (14) Dixit, S.; Hering, J. G. Comparison of Arsenic(V) and Arsenic(III) Sorption onto Iron Oxide Minerals: Implications for Arsenic Mobility. *Environ. Sci. Technol.* **2003**, *37* (18), 4182–4189.
- (15) Redman, A. D.; Macalady, D. L.; Ahmann, D. Natural Organic Matter Affects Arsenic Speciation and Sorption onto Hematite. *Environ. Sci. Technol.* **2002**, *36* (13), 2889–2896.
- (16) Polubesova, T.; Chefetz, B. DOM-Affected Transformation of Contaminants on Mineral Surfaces: A Review. *Crit. Rev. Environ. Sci. Technol.* **2014**, *44* (3), 223–254.
- (17) Duan, J.; Gregory, J. Coagulation by Hydrolysing Metal Salts. *Adv. Colloid Interface Sci.* **2003**, *100–102*, 475–502.
- (18) Kalbitz, K.; Kaiser, K. Contribution of Dissolved Organic Matter to Carbon Storage in Forest Mineral Soils. *J. Plant Nutr. Soil Sci.* **2008**, *171* (1), 52–60.
- (19) Lalonde, K.; Mucci, A.; Ouellet, A.; G elinas, Y. Preservation of Organic Matter in Sediments Promoted by Iron. *Nature* **2012**, *483* (7388), 198–200.
- (20) Situm, A.; Rahman, M. A.; Allen, N.; Kabengi, N.; Al-Abadleh, H. A. ATR-FTIR and Flow Microcalorimetry Studies on the Initial Binding Kinetics of Arsenicals at the Organic-Hematite Interface. *J. Phys. Chem. A* **2017**, *121* (30), 5569–5579.
- (21) Weng, L.; Van Riemsdijk, W. H.; Hiemstra, T. Effects of Fulvic and Humic Acids on Arsenate Adsorption to Goethite: Experiments and Modeling. *Environ. Sci. Technol.*

- 2009**, 43 (19), 7198–7204.
- (22) Mladenov, N.; Zheng, Y.; Simone, B.; Bilinski, T. M.; McKnight, D. M.; Nemergut, D.; Radloff, K. A.; Rahman, M. M.; Ahmed, K. M. Dissolved Organic Matter Quality in a Shallow Aquifer of Bangladesh: Implications for Arsenic Mobility. *Environ. Sci. Technol.* **2015**, 49 (18), 10815–10824.
- (23) Sharma, P.; Ofner, J.; Kappler, A. Formation of Binary and Ternary Colloids and Dissolved Complexes of Organic Matter, Fe and As. *Environ. Sci. Technol.* **2010**, 44 (12), 4479–4485.
- (24) Mikutta, R.; Lorenz, D.; Guggenberger, G.; Haumaier, L.; Freund, A. Properties and Reactivity of Fe-Organic Matter Associations Formed by Coprecipitation versus Adsorption: Clues from Arsenate Batch Adsorption. *Geochim. Cosmochim. Acta* **2014**, 144, 258–276.
- (25) Silva, G. C.; Vasconcelos, I. F.; De Carvalho, R. P.; Dantas, M. S. S.; Ciminelli, V. S. T. Molecular Modeling of Iron and Arsenic Interactions with Carboxy Groups in Natural Biomass. *Environ. Chem.* **2009**, 6 (4), 350–356.
- (26) Situm, A.; Rahman, M. A.; Goldberg, S.; Al-Abadleh, H. A. Spectral Characterization and Surface Complexation Modeling of Low Molecular Weight Organics on Hematite Nanoparticles: Role of Electrolytes in the Binding Mechanism. *Environ. Sci. Nano* **2016**, 3 (4), 910–926.
- (27) Sabur, M. A.; Al-Abadleh, H. A. Surface Interactions of Monomethylarsonic Acid with Hematite Nanoparticles Studied Using ATR-FTIR: Adsorption and Desorption Kinetics. *Can. J. Chem.* **2015**, 93 (11), 1297–1304.
- (28) Brechbühl, Y.; Christl, I.; Elzinga, E. J.; Kretzschmar, R. Competitive Sorption of

- Carbonate and Arsenic to Hematite: Combined ATR-FTIR and Batch Experiments. *J. Colloid Interface Sci.* **2012**, *377* (1), 313–321.
- (29) Sabur, M. A.; Goldberg, S.; Gale, A.; Kabengi, N.; Al-Abadleh, H. A. Temperature-Dependent Infrared and Calorimetric Studies on Arsenicals Adsorption from Solution to Hematite Nanoparticles. *Langmuir* **2015**, *31* (9), 2749–2760.
- (30) Arts, D.; Abdus Sabur, M.; Al-Abadleh, H. A. Surface Interactions of Aromatic Organoarsenical Compounds with Hematite Nanoparticles Using ATR-FTIR: Kinetic Studies. *J. Phys. Chem. A* **2013**, *117* (10), 2195–2204.
- (31) Tofan-Lazar, J.; Al-Abadleh, H. A. ATR-FTIR Studies on the Adsorption/Desorption Kinetics of Dimethylarsinic Acid on Iron-(Oxyhydr)Oxides. *J. Phys. Chem. A* **2012**, *116* (6), 1596–1604.

Chapter 4 Surface Water Structure and Hygroscopic Properties of Light Absorbing Secondary Organic Polymers of Atmospheric Relevance

This chapter of the thesis contains the following publication, reproduced from Rahman, M. A. and Al-Abadleh, H. A. *ACS Omega*, **2018**, 3, 15519-15529, licensed under an ACS AuthorChoice and accessible online at: <https://pubs.acs.org/doi/10.1021/acsomega.8b02066> with supplementary information accessible online at: https://pubs.acs.org/doi/suppl/10.1021/acsomega.8b02066/supplfile/ao8b02066_si_001.pdf.

4.1 Abstract

Hygroscopic properties and chemical reactivity of secondary organic aerosols (SOA) influence their overall contribution to the indirect effect on the climate. In this study, we investigate the hygroscopic properties of organic and organometallic polymeric particles, namely polycatechol, polyguaiacol, Fe-polyfumarate, and Fe-polyumuconate. These particles efficiently form in iron-catalyzed reactions with aromatic and aliphatic dicarboxylic acid compounds detected in field-collected SOA. The structure of surface water was studied using diffuse reflectance infrared Fourier transform spectroscopy (DRIFTS), and the uptake of gaseous water was quantified using quartz crystal microbalance (QCM) as a function of relative humidity. Spectroscopic data show that water bonding with organic functional groups acting as hydrogen bond acceptors cause shifts in their vibrational modes. Analysis of the hydroxyl group stretching region revealed weak and strong hydrogen bonding networks that suggest cluster formation reflecting water–water and water-organics interactions, respectively. A modified Type II multilayer Brunauer-Emmett-Teller adsorption model described the adsorption isotherm on the nonporous materials, polycatechol, polyguaiacol, and Fe-polyumuconate. However, water adsorption on porous Fe-polyfumarate was best described using a Type V adsorption model, namely the Langmuir-Sips model that accounts for condensation in pores. The data revealed that organometallic polymers are more hygroscopic

than organic polymers. The implications of these investigations are discussed in the context of the chemical reactivity of these particles relative to known SOA.

4.2 Introduction

Water is the solvent that affects the chemical reactivity and physical properties of atmospheric aerosols. There are molecular level differences in the structure of water between bulk and interfacial environments in atmospherically relevant systems.¹⁻³ These differences originate mainly from the number and strength of hydrogen bonds among water molecules and acceptor/donor groups.⁴⁻⁷ Reactions in liquid droplets that mimic chemistry in clouds were found to proceed at relatively lower rates than surface reactions because of solvent cage effects.⁸⁻¹⁰ Surface water in sea spray, ammonium sulfate, and mineral dust particles were shown to enhance ionic mobility, alter reaction pathways and surface speciation, and influence the hygroscopic properties of particles and their ability to form clouds.¹¹⁻¹⁴ In primary and secondary organic aerosol systems (POA and SOA), lab studies showed that temperature, relative humidity (RH), and molecular composition affect the size, viscosity, and phase state of these aerosols, which in turn affect the relative importance of bulk versus surface reactions.^{15,16} In multicomponent aerosol systems containing organics, inorganic salts, and water, changes in RH affect the aerosol liquid water ALW content and pH.^{17,18} As a result, the morphology and mixing state in the systems that can undergo deliquescence, efflorescence, and liquid-liquid phase separation are directly dependent on ALW content.^{19,20} Hence, measurements of water uptake as a function of RH are the first step toward understanding the reactivity of atmospheric aerosols. This is because water uptake curves provide crucial information on the solute to solvent ratio and surface area to volume ratio, which can be used to infer the surface chemical composition and determine the reactivity of the particles. One of the active areas of investigation in atmospheric chemistry is particle nucleation and growth via secondary pathways in the atmosphere. Processes that include atmospheric oxidation of volatile

organic compounds (VOCs) from biogenic and anthropogenic sources, gas-particle partitioning, and multiphase/heterogeneous reactions contributed to our understanding of SOA formation²¹⁻²⁴ and better parameterization of global climate models.²⁵ Following SOA formation, a number of chemical and photochemical aging processes lead to the formation of light absorbing soluble and insoluble components collectively known as “brown carbon”.²⁶ The role of transition metals such as iron in the formation and aging of SOA is not well understood.²⁷ Iron is a ubiquitous component of mineral dust, fly ash, and marine aerosols with speciation that varies by the aerosol source.²⁸⁻³² Uptake of acidic gases on iron-containing particles during long-range transport enhances the fraction of soluble iron in particles.³²⁻³⁴ Also, the concentration of dissolved iron was found to be affected by cycling between wet aerosols characterized by highly acidic conditions with a few layers of adsorbed water and cloud droplets characterized by more pH-neutral conditions.³⁵ Hence, given their rich chemistry, iron cations in (ALW) can catalyze a number of reactions with the organic content of aerosols. We recently reported that Fe(III) in solution leads to the formation of light absorbing secondary brown carbon via oxidative polymerization of polyphenols and metal-catalyzed polymerization of dicarboxylic acids.^{36,37} Polycatechol and polyguaiacol particles were formed from the reaction with semi-volatile phenolic precursors catechol and guaiacol emitted from biomass burning and produced by photooxidation of aromatic VOCs.³⁸ The reactions with Fe(III) were carried out under high solute/solvent ratio that mimic reactions in adsorbed water, with mass yields approaching 50% relative to the concentration of the organic precursor.³⁶ Also, the reaction of soluble Fe(III) with fumaric (trans-butenedioic) and muconic (trans,trans-2,4-hexadienedioic) acids, known photooxidation products of benzene, formed brightly colored organometallic nanoparticles with nearly 30% Fe (w/w) and 90% mass yields relative to the concentration of the acids.³⁷ The mass-normalized absorption coefficients of Fe-polyfumarate and Fe-polymuconate particles in the near UV light between 350 and 400 nm ranged from 1 to

$8 \text{ m}^2 \text{ g}^{-1}$, which are on the same order of magnitude as black carbon and biomass burning aerosols.³⁷

4.3 Objectives

The objective of this study is to investigate the hygroscopic properties of the aforementioned organic and organometallic particles, from the molecular-level structure of surface water to water adsorption and desorption isotherms as a function of RH. We utilized diffuse reflectance Fourier transform infrared spectroscopy (DRIFTS) to collect spectra of surface water in equilibrium with the gas phase. A quartz crystal microbalance (QCM) was used to quantify water uptake as a function of increasing and decreasing RH. We show that the presence of hydrogen bonding acceptor groups in these polymers promote the formation of adsorbed water clusters characterized by weak and strong hydrogen bonds relative to liquid water. We also show that organometallic polymers are more hygroscopic than organic polymers and can retain more water with decreasing RH. The implications of these investigations are discussed in the context of the chemical reactivity of these particles relative to known SOA. Figure 4.1 highlights a pictorial presentation of the overall research.

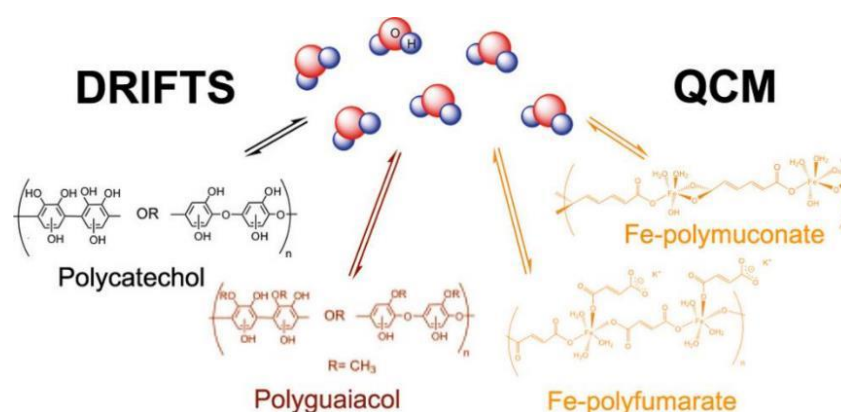


Figure 4.1 Schematic diagram for the interactions of H_2O molecules with model organic and organometallic particles.

4.4 Experimental

All the chemicals were used as received without further purification: catechol (1,2-benzenediol, >99%, CAS 120-80-9, Sigma-Aldrich), guaiacol (2-methoxyphenol, $\geq 98\%$, CAS

90-05-1, Sigma-Aldrich), fumaric acid (FA, trans-butenedioic acid, $\geq 99\%$, CAS: 110-17-8, Sigma-Aldrich), muconic acid (MA, trans, trans-2,4-hexadienedioic acid, 98%, CAS: 3588-17-8, Sigma-Aldrich), iron(III) chloride hexahydrate ($\text{FeCl}_3 \cdot 6\text{H}_2\text{O}$, 97%, CAS: 10025-77-1, Sigma-Aldrich), and diamond powder ($5 \pm 2 \mu\text{m}$, Lands Superabrasives LST600T). The synthesis procedure of polycatechol and polyguaiacol is reported in reference 36, and that for Fe-polyfumarate and Fe-polymuconate. Briefly, aqueous phase standard solutions of iron chloride, catechol, and guaiacol were prepared by dissolving the chemicals in Milli-Q water ($18.2 \text{ M}\Omega \text{ cm}$) with the solutions' ionic strength adjusted to 0.01 M by adding potassium chloride (KCl powder, 99.5%, EM Science) in order to stabilize the pH. The pH was adjusted using stock solutions of hydrochloric acid (HCl 6 N, Ricca Chemical Company) and sodium hydroxide (NaOH pellets, 99–100%, EMD). The concentration of the organic precursors was 1 mM in 100 mL, to which 2 mL of the iron chloride solution was added to start the reaction in the dark for 2 h. To get the maximum yield, the initial pH was adjusted to 3 for experiments with catechol and guaiacol, and 5 for experiments with fumaric and muconic acids. The resulting iron to organic molar ratio after mixing is 2:1. The reaction solution was then filtered on nylon membrane filters ($0.2 \mu\text{m}$ pore size, 47 mm dia., EMD Millipore) using a suction filtration system (VWR). After filtration, the products were air dried overnight. The filters were weighed before and after filtration to measure the mass of the product. The organic polymers were then scratched from the filter using a spatula into a clean vial for future use. Some of the material collected on the filters was analyzed for Brunauer-Emmett-Teller (BET) surface area using N_2 gas in a Nova 2200e multigas surface area analyzer (Quantachrome Instruments). The surface area values were found to be 4 ± 0.6 , 14 ± 2 , 36 ± 5 , $6 \pm 1 \text{ m}^2\text{g}^{-1}$ for polycatechol, polyguaiacol, Fe-polyfumarate, and Fe-polymuconate, respectively.

4.4.1 DRIFT experiments

Samples were prepared for the gas phase water uptake experiments by mixing about $7\text{-}20 \times 10^{-3}$ g of the organic polymers (ground using a grinding mill, wig-L bug, for 30 s) with ~ 0.30 g diamond powder in a stainless-steel crucible followed by mechanical shaking for 60 s without the grinding ball. This procedure was found to result in homogenous and reproducible samples. The samples were then poured into the reaction cup of a stainless-steel high temperature reaction chamber treated with a special Silco Steel-CR coating (HVC, cup 6 by 3 mm, dome cover with two Ge windows and one quartz viewing window, Harrick Scientific). Efficient and reproducible packing of the sample was obtained using a 4 kg weight for 15 min placed on top of a custom-made T-shape stainless steel cover with similar dimensions to the reaction cup.³⁹ The reaction chamber is then mounted into the praying mantis diffuse reflectance accessory (Harrick, DRK- 4N18). The DRIFTS accessory was installed into a Nicolet 8700 FTIR spectrometer (Thermo Instruments) equipped with a liquid N₂-cooled mercury cadmium telluride detector and a purge gas generator (Parker/Balston Analytical Gas Systems Purge Gas Generator 75-52). The reaction chamber has two ports for flowing gases and was connected to a gas handling system described earlier.⁴⁰ Briefly, purged air flowing into a water bubbler containing 18.2 M Ω -cm ultrapure water was mixed with dry air in a glass chamber. In one set of experiments using polyguaiacol as a sample, liquid D₂O (99.9 atom % D, Sigma Aldrich) replaced the ultrapure water in the bubbler to flow gas phase D₂O. The RH of the gas mixture was varied by changing the settings on two mass flow controllers (MKS). A RH sensor (Vaisala HM70) was used to monitor the RH of the gas exiting the chamber. The same gas handling system was used in the QCM experiments described below. In a typical DRIFTS experiment, dry air was flowed over the sample in the reaction chamber overnight at room temperature. The Fe-polyfumarate sample was heated to 50 °C to enhance desorption of gases trapped in the pores of that material. A single beam spectrum was collected for the “dry” sample first,

followed by introducing humid air as a function of increasing RH. All spectra were collected at 8 cm^{-1} resolution by averaging 100 scans. Absorbance spectra of surface water were generated by referencing the single beam spectra collected while flowing humid air to the spectrum collected initially for the dry sample. Similar experiments were conducted using a mirror (Harrick) in place of the reaction chamber to collect spectra of gas phase water. These spectra were used to subtract out gas phase water lines from the absorbance spectra of surface water. Control experiments were also conducted where diamond powder only was packed into the reaction chamber (no organic polymer sample). These spectra were used to subtract out contributions to the absorbance features from the sample spectra.

4.4.2 QCM experiments

Gas phase water uptake experiments on thin films of polycatechol, polyguaiacol, Fe-polyfumarate, and Fe-polymuconate were performed using a commercial QCM (eQCM 10 M, Gamry Instruments). The QCM houses a 0.550" dia. gold-coated quartz crystal (5 MHz) on which the thin organic films were deposited. The QCM crystal connected to the resonator was mounted onto a custom-made holder with a cover containing two ports and an opening to insert a RH sensor (Sensirion, EK-H5). The gas handling system described above for the DRIFTS experiments was connected to a gas mixing chamber to control the RH of the air flowing over the abovementioned samples. A RH sensor (Vaisala HUMICAP HM70) was placed in the gas line directly before the QCM sample holder. The polycatechol film was prepared by depositing a total volume of 60.0 μL using a 25 μL syringe (Hamilton Co.) from 5.0 mg mL^{-1} solution (prepared in 6:4 H_2O -EtOH mixture and sonicated for 40 min). The polyguaiacol film was prepared by depositing a total volume of 60.0 μL from 1.7 mg mL^{-1} solution (prepared in 6:4 H_2O -EtOH mixture and sonicated for 10 s). In case of Fe-polyfumarate, the film was prepared by depositing total volume of 44.0 μL from a 0.83 mg mL^{-1} solution (prepared in 6:4 EtOH- H_2O mixture and sonicated for 40 min). However, the Fe-polymuconate film was prepared by

depositing a total volume of 44.0 μL from a 2.5 mg mL^{-1} solution (prepared in 4.5:5.5 EtOH- H_2O mixture and sonicated for 40 min). The diameter of the film was measured after the solvent dried and was found to be ca. 0.8 ± 0.1 cm. Each film was allowed to dry overnight under a flow of dry air. In a typical QCM experiment, the initial frequency baseline was recorded while flowing dry air, and then humid air was introduced to dry air starting with the lowest RH value followed by incrementally increasing the mass flow of humid air, while allowing 30 min for equilibrium at each RH value for the adsorption part of the experiment. The total mass flow of humid and dry air was maintained at 500 sccm. Once the highest RH is obtained, the mass flow of the humid air is decreased incrementally, while allowing 30 min for equilibrium at each RH to record the desorption part of the experiment. Separate experiments were run for longer than 30 min to confirm achieving equilibrium, which is defined as the time at which insignificant change was observed in frequency with time. We found that allowing 30 min for equilibrium for all samples was long enough to cover as many RH values before the balance showed signs of electrical instability.

4.5 Results and discussion

4.5.1 Structure of surface water on polycatechol and polyguaiacol

The structure of surface water on polycatechol and polyguaiacol mixed with diamond powder (used to enhance scattering efficiency of the samples) was studied using DRIFTS as a function of increasing RH over samples dried overnight by a flow of dry air (RH < 1%).

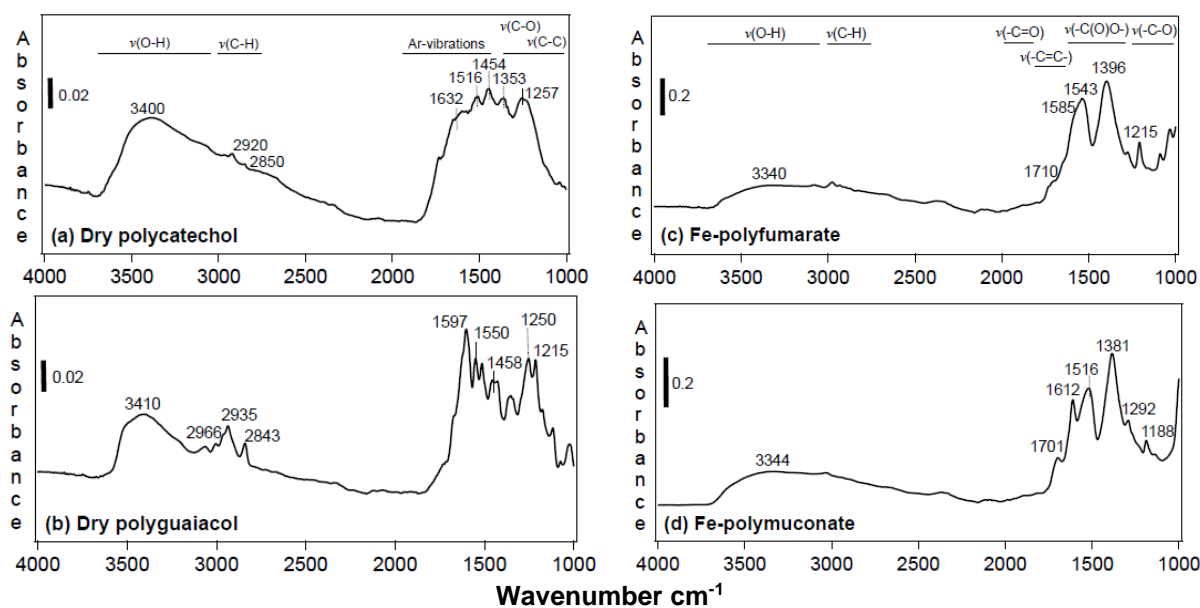
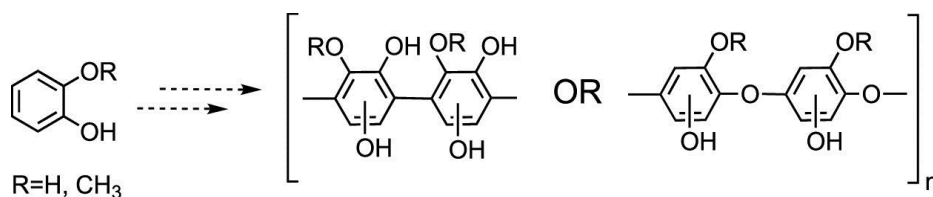


Figure 4.2 Representative DRIFTS absorbance spectra of solid organic polymers mixed with diamond powder after overnight drying at a flow of dry air: (a) 2% wt/wt polycatechol, (b) 2% wt/wt polyguaiacol, (c) 6% wt/wt Fe-polyfumarate, and (d) 7% wt/wt Fe-polymuconate. A spectrum of dry diamond powder only was used as the reference to generate these absorbance spectra. See reference 46 in main manuscript for assignment.

Figures 4.2a and 4.2b show the DRIFTS absorbance spectra of the dry samples. These spectra were obtained by referencing to the spectrum of dry diamond powder only. The spectral range 2000-1000 cm^{-1} contains fundamental vibrational modes of the functional groups in the polymer backbone of polycatechol and polyguaiacol, namely stretching vibrations (ν) because of C-C, C-O, and aromatic $-\text{C}=\text{C}-$ modes. The spectra are identical to those reported earlier by our group for dry thin films using ATR-FTIR (see the Supporting Information in ref 36). The absorbance features for the organic polymers are clearly distinguishable from the monomers, whether in the solid or aqueous phases.^{36,41} Scheme 4.1 shows the suggested general structure of these polymers.⁴²⁻⁴⁴



Scheme 4.1 General structure of units in polycatechol and polyguaiacol formed in oxidative polymerization reactions.

The presence of $\nu(\text{C}=\text{O})$ cannot be excluded with certainty because of the broadness of the feature in the 2000-1000 cm^{-1} range, and because mass spectrometry studies on the soluble products of the guaiacol dimerization reactions reported structures containing $\text{C}=\text{O}$.⁴⁵ Also, the spectral range 3600-2500 cm^{-1} contains features assigned to $\nu(\text{C}-\text{H})$ and $\nu(\text{O}-\text{H})$. The former mode is more intense for polyguaiacol compared to polycatechol because of the presence of $-\text{CH}_3$ groups. The broad feature centered around 3400 cm^{-1} originates from hydrogen bonded $-\text{OH}$ groups, whether with neighboring units or residual water molecules not removed by flowing dry air at room temperature. As detailed below, understanding the structure of the dry material aids in interpreting the spectra obtained as a function of RH. Figures 4.3a and 4.3b show representative DRIFTS absorbance spectra collected as a function of increasing % RH (solid lines) on polycatechol and polyguaiacol mixed with diamond powder samples (2% w/w).

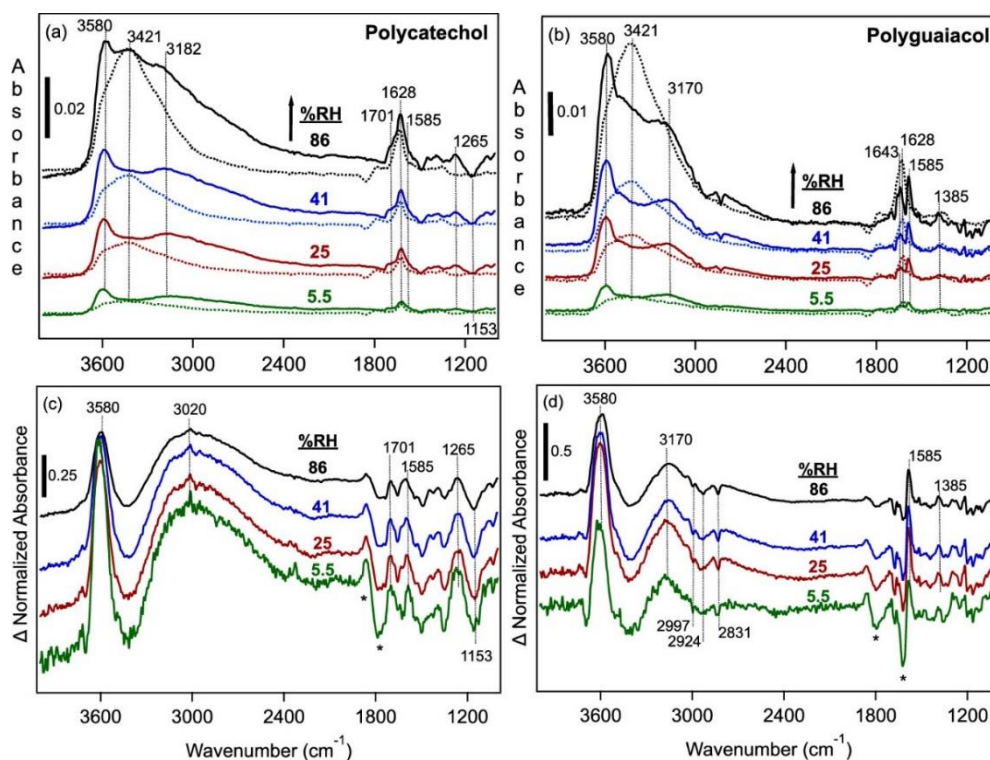


Figure 4.3 Selected DRIFTS absorbance spectra of surface water collected as a function of increasing % RH on (a) polycatechol and (b) polyguaiacol (solid lines) in ca. 2% w/w organic material/diamond powder. The dotted lines are control spectra collected on diamond particles only (no organic material) at the same % RH values. Data in (c,d) show the difference in normalized absorbance spectra as a function of RH obtained by subtracting the normalized diamond spectrum from that collected with organic materials at each % RH with a factor 1. The normalization of all spectra was done relative to the peak at 3421 cm^{-1} . The “*” denotes residual features observed only in the control spectra.

Control experiments were conducted on diamond powder only (no organic polymers) under the same conditions (dotted lines). These spectra were obtained by referencing to the spectrum of the dry organic polymer or diamond powder, respectively. Hence, the spectral features observed are due to increasing the coverage of surface water characterized by the nearly symmetric bending mode, $\delta(\text{H}_2\text{O})$, between 1630 and 1645 cm^{-1} and broad absorbance, $\nu(\text{OH})$, in the range 3600-2500 cm^{-1} . There are other clear differences in the spectra of the samples versus the control that cannot be assigned to surface water. To isolate these features, the spectra in Figures 4.3a and 4.3b were normalized to the intensity of the peak at 3421 cm^{-1} , and then the normalized diamond spectrum was subtracted out from the corresponding spectrum for polycatechol and polyguaiacol. This spectral subtraction procedure of normalized spectra

removes the contribution of concentration to absorbance. Hence, the net spectra highlight changes to functional groups because of water adsorption. The resultant difference spectra are shown in Figure 4.3c,d, and the assignment of the features is listed in Table 4.1.

Table 4.1 Assignment of features observed in the DRIFTS normalized difference absorbance spectra during gas phase water adsorption on organic polymers/diamond samples. ^{a,b}

vibrational mode	wavenumber (cm ⁻¹)			
	polycatechol	polyguaiacol	Fe-polyfumarate	Fe-polymuconate
$\delta(\text{OH})_{\text{ar}}$ or $\nu(\text{C-O})_{\text{ar}}$	1153(-)			
$\nu(\text{C-O})$			1223(+)	
$\nu(\text{C-O})_{\text{ar}}$ + $\delta(\text{CH})_{\text{ar}}$	1265(+)			
$\nu(\text{C-C})_{\text{ar}}$ + $\delta(\text{OH})_{\text{ar}}$		1385(+)		
$\nu(-\text{C}(\text{O})\text{O}-)$				1416(-)
			1446(-)	
			1516(-)	
$\nu(\text{C-C})_{\text{ar}}$ + $\nu(\text{C-O})_{\text{ar}}$	1585(+)	1585(+)		
$\nu(-\text{C}=\text{C}-)$			1620(-)	1628(-)
$\nu(\text{C}=\text{O})$				1686(+)
$\nu(\text{C}=\text{O})$	1701(+)		1705(+)	
$\nu(\text{C}=\text{O})$			1743(-)	1728(-)
$\nu(\text{OH})$	3020(+)		3020(+)	3020(-)
$\nu(\text{OH})$		3170(+)		
$\nu(\text{OH})$	3580(+)	3580(+)	3564(+)	3564(+)
$\nu(\text{OH})$			3641(+)	3641(+)

^aThese features highlight the functional groups affected by surface water. ^b(+) for the positive feature, (-) for the negative feature. ar = aromatic. See reference⁴⁶ for assignment.

The $\nu(\text{OH})$ peaks at 3580 and 3020 cm⁻¹ for polycatechol and 3580 and 3170 cm⁻¹ for polyguaiacol suggest the presence of surface water with hydroxyl groups involved in weak and strong hydrogen bonding, respectively. Similar features were observed for water adsorption on tannic acid,⁴⁰ where water adsorbs in clusters, and water molecules in contact with organic groups have fewer hydrogen bonds compared to the interior of water clusters that resemble liquid water or ice. Also, the difference spectra show changes in the 1800-1000 cm⁻¹, suggesting changes to the frequency of the organic functional groups in polycatechol and polyguaiacol with increasing coverage of surface water. The negative feature at 1153 cm⁻¹ in Figure 4.3c is associated with $\nu(\text{C-O})$ and $\delta(\text{OH})$, which are hydrogen bonding accepting groups. A similar result was obtained from water adsorption on tannic acid.⁴⁰ The positive features at 1701, 1585, 1265 cm⁻¹ for polycatechol, and 1585 and 1385 cm⁻¹ for polyguaiacol suggest changes to the aromatic $-\text{C}=\text{C}-$ vibrations because of the presence of surface water.

Water-benzene interactions were studied theoretically⁴⁷⁻⁵⁰ and in the gas phase⁵¹ because benzene is polarizable and consequently participates in the hydrogen bonding network of water.

To further explore the assignment of the spectral features near $\delta(\text{H}_2\text{O})$, namely 1585 cm^{-1} , experiments were conducted by flowing D_2O vapor over a polyguaiacol/diamond sample. Because this spectral feature became apparent in the difference of normalized spectra for the polycatechol/diamond sample (Figure 4.3c), the results obtained with the polyguaiacol isotopic exchange experiments are also applicable to the polycatechol sample. Solid lines in Figures 4.4 and 4.5 show the absorbance spectra collected as a function of increasing % RH in the spectral ranges $1800\text{-}1000$ and $4000\text{-}2000\text{ cm}^{-1}$, respectively.

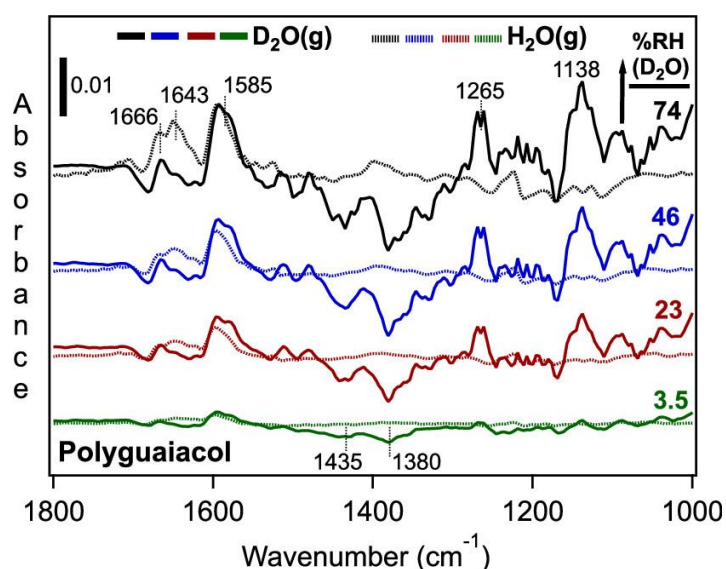


Figure 4.4 Selected DRIFTS absorbance spectra of surface water collected as a function of increasing % RH on a 2% w/w polyguaiacol/diamond sample. The solid lines are spectra collected using gas phase D_2O . The dotted lines are the same spectra shown in Figure 4.3b collected using gas phase H_2O at 5.5, 25, 41, and 86% RH.

The dotted lines in these figures are for spectra collected while flowing H_2O vapor from a Millipore water source. The solid lines in Figure 4.4 clearly show the disappearance of the feature at 1643 cm^{-1} assigned to $\delta(\text{H}_2\text{O})$ because of isotopic exchange. The positive symmetrical feature at 1265 cm^{-1} is assigned to the bending mode of isotopically labeled surface water because it is closer to the frequency of the $\delta(\text{D}_2\text{O})$ in the liquid phase (1206 cm^{-1})⁵² than that of liquid HDO at 1450 cm^{-1} .⁵³ The nearly 60 cm^{-1} blue shift can be attributed to

structural differences in the hydrogen bonding network in surface water compared to the liquid phase.

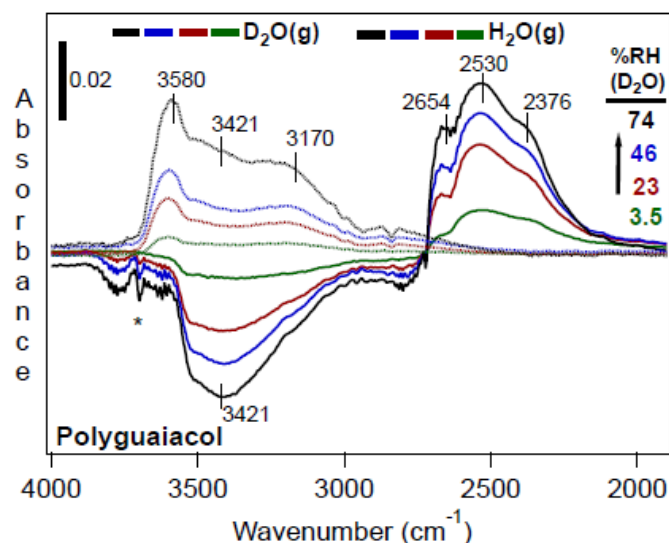


Figure 4.5 Selected DRIFTS absorbance spectra of surface water collected as a function of increasing %RH on a 2% wt/wt polyguaiacol/diamond sample. The solid lines are spectra collected using gas phase D₂O. The dashed lines are the same spectra shown in Figure 1b collected using gas phase H₂O at 5.5, 25, 41 and 86% RH. The ‘*’ donates incomplete subtraction of gas phase water lines.

The features at 1666 and 1585 cm⁻¹ were not affected by isotopic exchange confirming their assignment to aromatic -C=C- vibrations. The negative features at 1435 and 1380 cm⁻¹ and the positive feature at 1138 cm⁻¹ are only present while flowing D₂O and they increase in intensity with increasing % RH. Because the spectrum of the “dry” sample was used as a reference to generate the absorbance spectra shown in Figure 4.4, the observed negative and positive features suggest the presence of residual surface water not removed with sample drying with dry air flow at room temperature overnight. As shown in Table 4.1, 1380 cm⁻¹ and, by extension, the adjacent band at 1435 cm⁻¹ frequencies are assigned to aromatic $\delta(\text{OH})_{\text{ar}}$ coupled with aromatic $\nu(\text{C}-\text{C})_{\text{ar}}$. Because OH groups and the π system of the benzene ring are hydrogen (deuterium) bond acceptor groups,^{49,50} it is likely that H/D isotopic exchange in surface water directly bonded with them affected the $\delta(\text{OH})_{\text{ar}}$ and $\nu(\text{C}-\text{C})_{\text{ar}}$ fundamental frequencies. Moreover, the spectral range 4000-2000 cm⁻¹ shows changes to the $\nu(\text{OH})$ features at 3580,

3421, and 3170 cm^{-1} observed in Figure 4.3b due to H/D isotopic exchange with gas phase D_2O (solid lines). For comparison, the dotted lines in Figure 4.5 show the same spectra in Figure 4.3b collected using gas phase H_2O . The new positive features at 2654, 2530, and 2376 cm^{-1} are assigned to $\nu(\text{OD})$ in surface water. The ratio of the corresponding $\nu(\text{OH})$ to the $\nu(\text{OD})$ is nearly 1.35, which is very close to the ratio obtained from the reduced masses, $\mu_{\text{OD}}/\mu_{\text{OH}} = 1.38$. This ratio is also close to that obtained from the symmetric and asymmetric OH(D) stretch in liquid H_2O and D_2O , 1.36.⁵² Again, the observed positive and negative features in Figure 4.5 suggest the presence of residual surface water that undergo H/D isotopic exchange with increasing flow of D_2O vapor. In summary, gas phase water adsorption on polycatechol and polyguaiacol occurs with hydrogen bonding acceptor groups in these organic polymers, leading to the formation of clusters with water-organic and water-water hydrogen bonds that cause shifts in the vibrational modes of the functional groups by direct contact with surface water. The next section shows data for water adsorption on iron-containing aliphatic organometallic polymers for comparison with the aromatic organic polymers discussed above.

4.5.2 Structure of surface water on Fe-polyfumarate and Fe-polymuconate

Figures 4.6a and 4.6b show representative DRIFTS absorbance spectra of water adsorption on dry Fe-polyfumarate and Fe-polymuconate samples as a function of increasing % RH (solid lines). These spectra were obtained by referencing to the spectrum of the dry samples following overnight flow of dry air (Figures 4.2c and 4.2d). The dry spectra are identical to those reported earlier by our group for thin films using ATR-FTIR.³⁷ The absorbance features for these organometallic polymers were assigned based on the structure of the organic precursors and data obtained from analyzing the solid particles using electron energy loss spectroscopy and X-ray absorption spectroscopy.

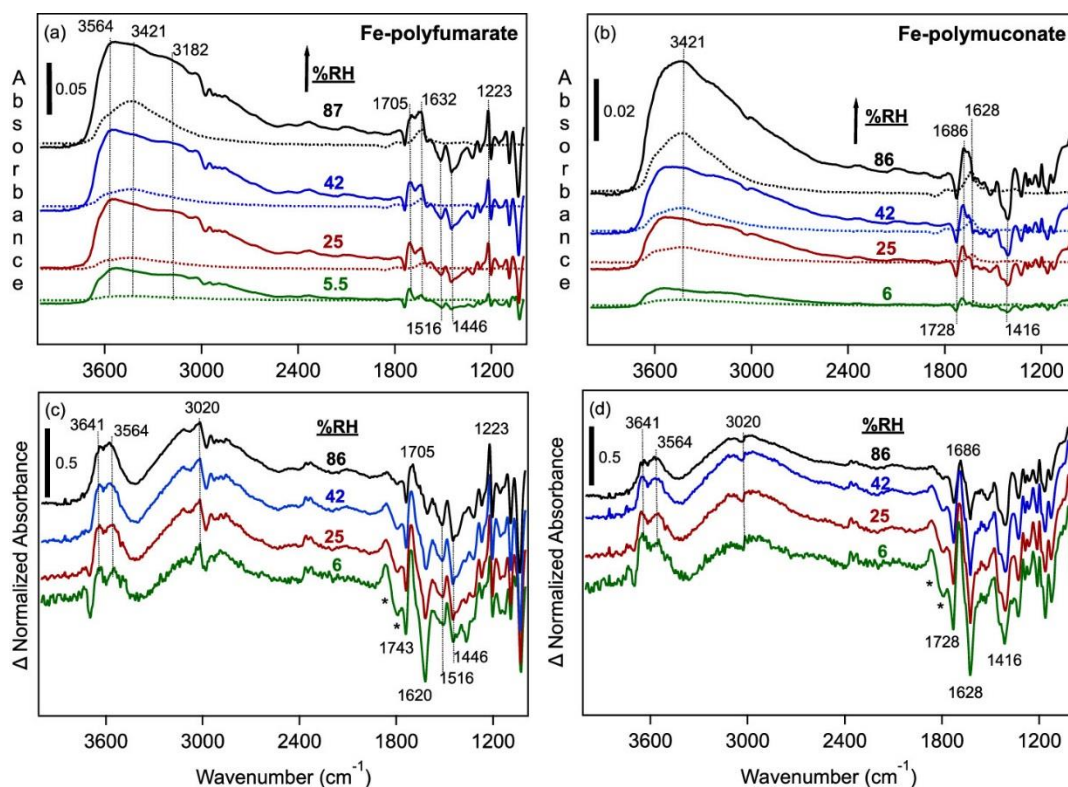
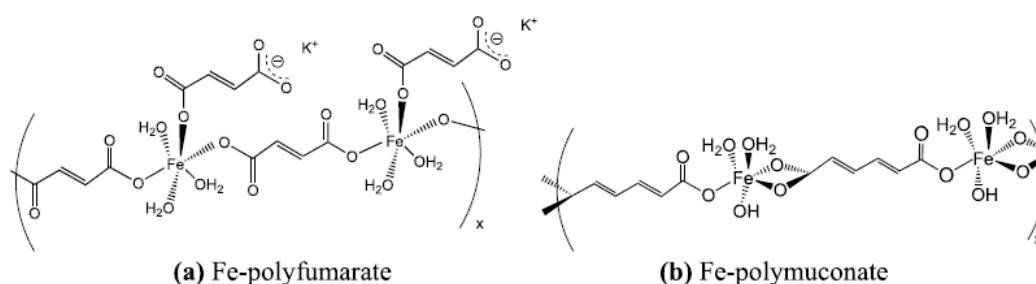


Figure 4.6 Selected DRIFTS absorbance spectra of surface water collected as a function of increasing % RH on (a) Fe-polyfumarate and (b) Fe-polymuconate (solid lines) in ca. 7% w/w organic material/diamond particles. The dotted lines are control spectra collected on diamond particles only (no organic material) at the same % RH values. Data in (c,d) show the difference in normalized absorbance spectra as a function of RH obtained by subtracting the normalized diamond spectrum from that collected with organic materials at each RH with a factor of 1. The normalization of all spectra was done relative to the peak at 3421 cm^{-1} . The “*” denotes residual features observed only in the control spectra.

Scheme 4.2 shows the suggested structure of these organometallic polymers formed in the aqueous phase reaction of FeCl_3 with fumaric and muconic acids at pH 5, respectively.³⁷



Scheme 4.2 Suggested structure of units in Fe-polyfumarate and Fe-polymuconate.³⁷

The spectral range $2000\text{--}1000\text{ cm}^{-1}$ contains aliphatic $\nu(\text{--C=C--})$, $\nu(\text{--C=O})$, $\nu(\text{--C(O)O--})$, and $\nu(\text{C--O})$. The latter three functional groups are considered hydrogen bonding acceptors. The

iron centers in these organometallic polymers contain water molecules and hydroxyl ligands capable of hydrogen bonding with surface water as well. The spectra shown in dotted lines in Figure 4.6a,b are the same as those shown in Figure 4.3a,b for water uptake on diamond powder only. Increasing % RH resulted in increasing the absorbance assigned to $\nu(\text{OH})$ and $\delta(\text{H}_2\text{O})$ centered at 3421 and 1632 cm^{-1} , respectively. There are also other clear differences in the spectra of surface water on the samples versus the control with increasing % RH. These differences include the structure of the $\nu(\text{OH})$ broad band, increasing absorbance at 1705 and 1223 cm^{-1} (Fe-polyfumarate) and 1686 cm^{-1} (Fe-polymuconate), and decreasing absorbance at 1516 and 1446 cm^{-1} (Fe-polyfumarate) and 1416 cm^{-1} (Fe-polymuconate). To better isolate these features, the spectra in Figure 4.5a and 4.5b were normalized to the intensity of the peak at 3421 cm^{-1} , and then the normalized diamond spectrum was subtracted from the corresponding spectrum for Fe-polyfumarate and Fe-polymuconate (Figure 4.6c and 4.6d). Table 4.1 lists the assignment of the features observed in Figure 4.6c and 4.6d. This subtraction procedure clearly revealed the spectral features responsible for the structure in the $\nu(\text{OH})$ broad band, namely 3641, 3564 cm^{-1} , and the feature near 3020 cm^{-1} . The former frequencies indicate the presence of OH functional groups involved in weak hydrogen bonding such as those in direct contact with the hydrophobic part of the polymers. The sharp negative features near 3020 cm^{-1} suggest changes to $\nu(\text{C-H})$ ⁴⁶ in the aliphatic backbone of the polymers as a result of water adsorption and the formation of weak $\text{OH}\cdots\pi$ hydrogen bonds.⁵⁴ The tailing of the OH broad band till 2500 cm^{-1} is characteristic of hydrogen bonding network on organic particles and films and is correlated with the presence of stronger hydrogen bonds relative to those in the liquid phase of water.^{40,55,56} In addition, the negative features in the 1800-1200 cm^{-1} spectral range (Figures 4.6c and 4.6d) appear at 1620, 1516, and 1446 cm^{-1} for Fe-polyfumarate, and 1628 and 1416 cm^{-1} for Fe-polymuconate. As listed in Table 4.1, vibrational modes in this range are assigned to $\nu(-\text{C}(\text{O})\text{O}-)$ and $\nu(-\text{C}=\text{C}-)$. These functional groups are hydrogen bonding

acceptor groups and hence, water adsorption appears to change their fundamental vibrational frequency relative to the “dry” sample. The positive features at 1705 cm^{-1} for Fe-polyfumurate and 1686 cm^{-1} for Fe-polymuconate suggest weakening of the C=O relative to the dry sample, where $\nu(\text{C=O})$ appeared at 1710 and 1701 cm^{-1} , respectively (Figures 4.2c and 4.2d). Also, the positive feature 1223 cm^{-1} for polyfumurate is assigned to $\nu(\text{C-O})$, which is higher than the 1215 cm^{-1} peak observed in the dry sample. While the difference is within the resolution of our measurements, the slight blue shift might indicate an effect of hydrogen bonding on C-O groups. In summary, ligands on the metal centers and hydrogen bonding acceptor groups in Fe-polyfumurate and Fe-polymuconate interact within adsorbed water, forming clusters characterized by weaker and stronger hydrogen bonds relative to liquid water. The formation of these clusters causes shifts in the vibrational modes of the organic groups in direct contact with surface water. With this understanding of the structure of surface water on organic and organometallic polymers of atmospheric relevance, the next section quantifies water uptake as a function of % RH with mathematical models that best describe the hygroscopicity of these materials.

4.5.3 Adsorption thermodynamics

To obtain thermodynamic parameters for gas phase water adsorption on the organic polymers studied herein, a QCM was used to quantify the amount of surface water as a function of % RH. For these experiments, thin films of the organic polymers were deposited on a gold-coated quartz crystal with an oscillation frequency of 5 MHz. The amount of the deposited organic films was optimized such that it is small enough not to change the oscillating frequency of the QCM crystal and large enough to observe changes in frequency because of gas phase water adsorption. The change in frequency, ΔF , due to gas phase water adsorption or desorption are converted to change in mass, Δm , according to the Sauerbrey equation: $\Delta F = -C_f \Delta m$, where C_f ($\text{Hz cm}^2\text{ g}^{-1}$) is a sensitivity factor unique to a particular crystal. The unit for area (cm^2)

assumes that the material coats the entire exposed area of the QCM crystal. To quantify surface water, the value of C_f was obtained from calibration experiments using droplets of liquid water with amounts that give rise to linear ΔF versus Δm . Because of the high surface tension of water, these droplets did not cover the exposed area of the QCM crystal. The geometrical contact area of the droplets with the QCM crystal was calculated and multiplied by ΔF . This way, the slope of the line of area corrected ΔF versus Δm would have units of $\text{Hz cm}^2 \text{g}^{-1}$. The value of C_f from the water calibration experiments was found to be $22564 \pm 1519 \text{ Hz cm}^2 \text{g}^{-1}$. Figures 4.7 and 4.8 show raw QCM data as a function of time and % RH (2–88%) on dry polycatechol, polyguaiacol, Fe-polyfumarate, and Fe-polymuconate, respectively.

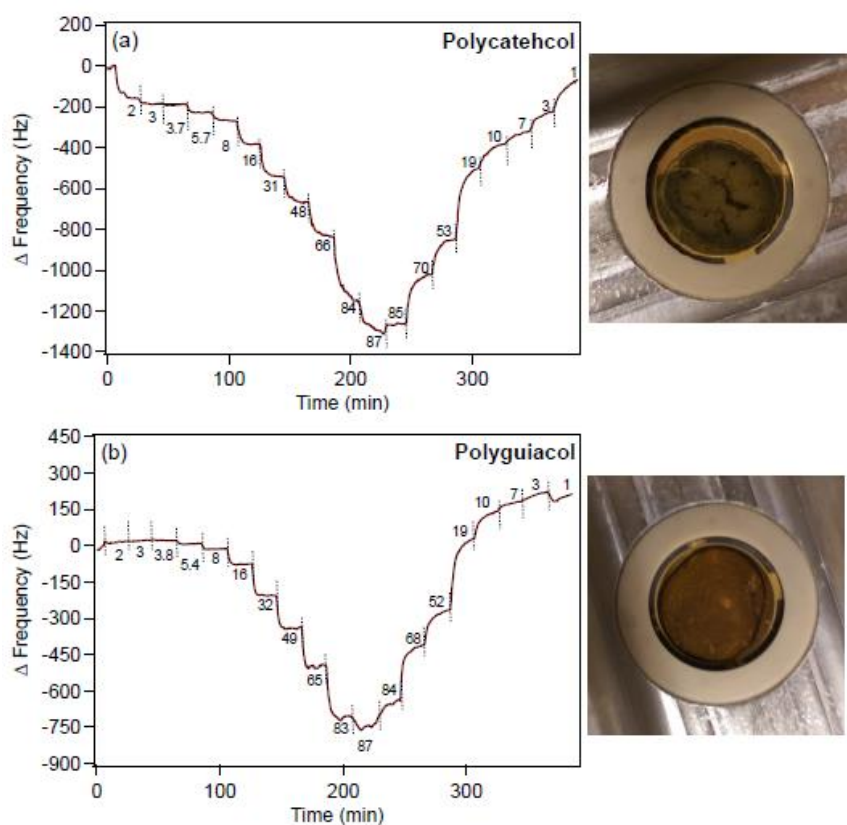


Figure 4.7 Raw QCM data showing change in frequency, ΔF , as a function of increasing relative humidity (%RH, numbers between vertical dashed lines) relative to signal recorded while flowing dry air on (a) polycatechol (0.3 mg), and (b) polyguaiacol (0.1 mg) thin films. Photos to the right show representative samples prior to starting the water uptake experiments.

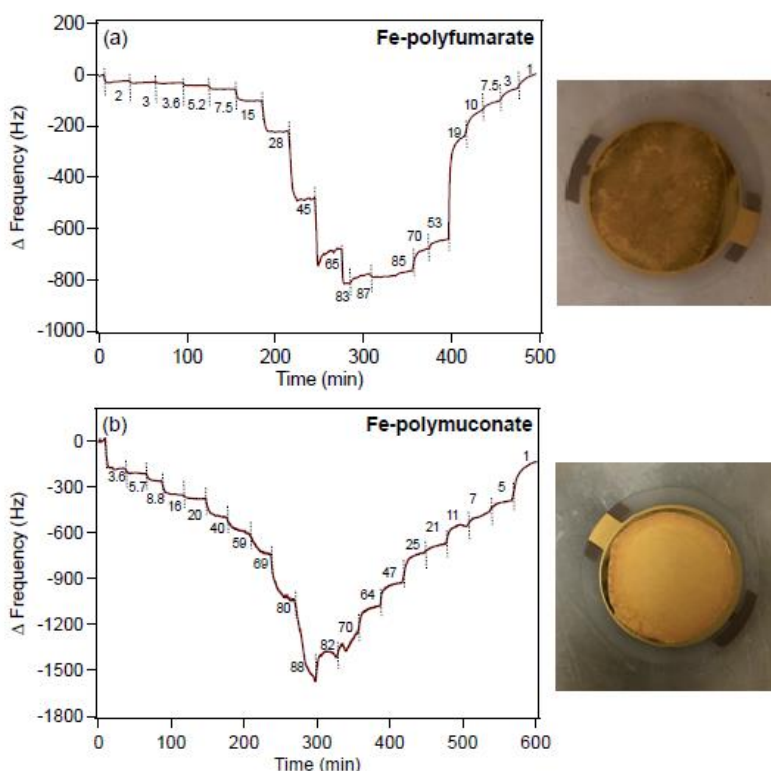


Figure 4.8 Raw QCM data showing change in frequency, ΔF , as a function of increasing relative humidity (%RH, numbers between vertical dashed lines) relative to signal recorded while flowing dry air on (a) Fe-polyfumarate (0.037 mg), and (b) Fe-polymuconate (0.11 mg) thin films. Photos to the right show representative samples prior to starting the water uptake experiments.

Representative images of the thin films deposited on the QCM crystal are shown to the right of the raw data. Increasing % RH of the humid air flowing over the films results in negative ΔF , which was calculated relative to the initial frequency while flowing dry air. The decrease in frequency indicates a positive Δm due to the increase in the coverage of surface water. Upon decreasing % RH of the humid air flowing over the film, values of ΔF become less negative, which correlates with water desorption from the films. The ΔF values were corrected for the geometrical area of the deposited films and then converted to the amount of surface water, Δm , using the C_f value mentioned above. To show the adsorption and desorption isotherms of surface water on organic polymer thin films, the left axes in Figure 4.9 are for Δm values versus % RH, and the right axes are the corresponding mass of surface water normalized to the surface

area of the deposited organic film. The latter is useful for comparing water uptake on different materials to examine their relative hygroscopic properties. The shape of the adsorption isotherms in Figure 4.9 a,b,d is similar to Type II isotherms that indicate multilayer adsorption modeled using the 2-fit parameter BET model.^{13,57} This model was derived for adsorption on uniform surfaces with infinite number of layers. However, for adsorption on heterogeneous particles such as the organic polymers studied herein, adsorption results in the formation of a

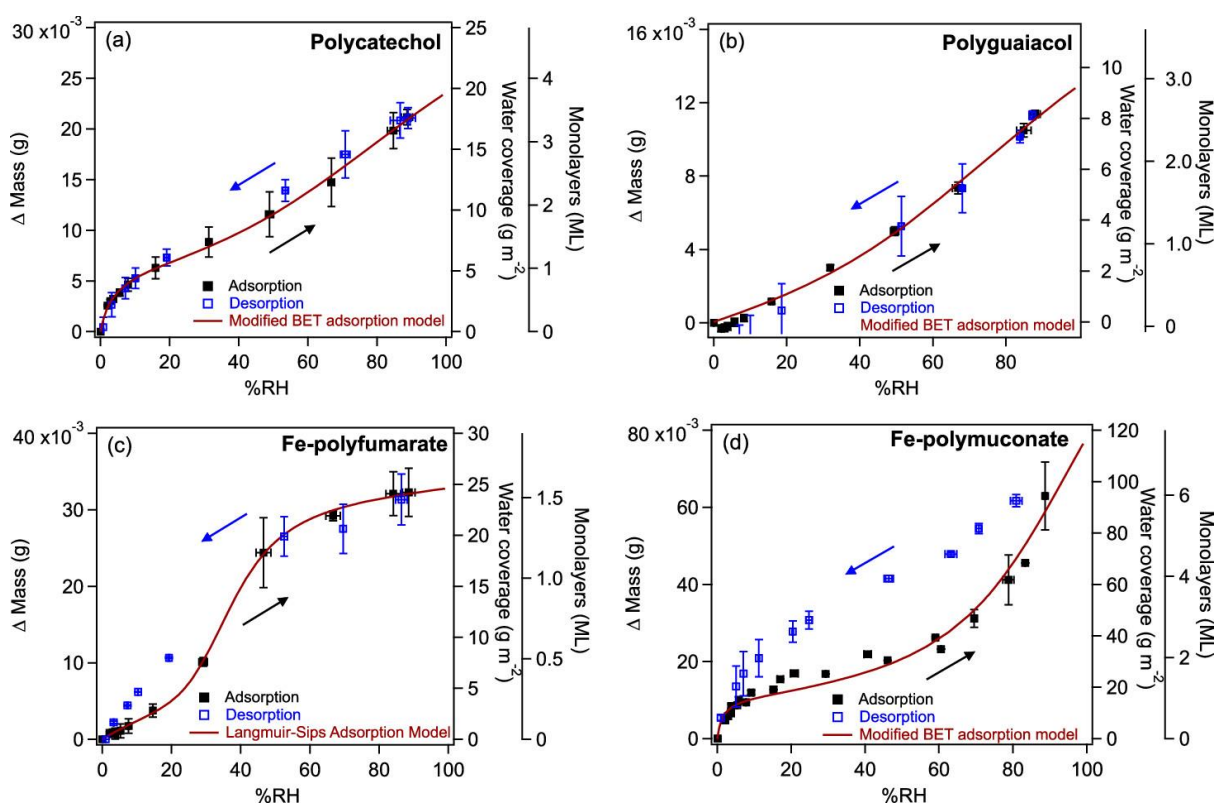


Figure 4.9 Water adsorption isotherms at 298 K constructed from the data shown in Figures 4.7 and 4.8 for (a) polycatechol (0.3 mg), (b) polyguaiacol (0.1 mg), (c) Fe-polyfumarate (0.037 mg), and (d) Fe-polymuconate (0.1 mg) using the equation $\Delta m = -\Delta F/C_f$, where Δm is the change in mass due to adsorbed water (left axis). ΔF was multiplied by the geometrical area of the deposited films. The right axes were calculated by converting Δm to water mass (g) per surface area (m^2) of the organic film deposited. The lines through the data represent least-squares best fits to the experimental data. The best fit parameters are listed in Table 4.2. The outermost right axis was obtained by dividing water coverage in gm^{-2} by that at the monolayer coverage obtained from the best-fit parameters. The error bars represent the standard deviation ($\pm\sigma$) from the average data of 3–4 water isotherm experiments, each on a freshly prepared organic film.

finite number of layers. A modified 3-fit parameter BET model was described by Goodman *et al.* that takes into account the finite number of layers.⁵⁸

$$m = \left[\frac{m_{\text{ML}}c(\text{RH})}{1 - (\text{RH})} \right] \left[\frac{1 - (n + 1)(\text{RH})^n + n(\text{RH})^{n+1}}{1 + (c - 1)(\text{RH}) - c(\text{RH})^{n+1}} \right] \dots\dots\dots 4.1$$

where m is the surface coverage of water (gm^{-2}), m_{ML} is the monolayer surface coverage of water (gm^{-2}), c is a unitless temperature-dependent constant related to the enthalpies of adsorption of the first, ΔH_1° , and subsequent layers (expressed as the standard enthalpy for water vapor condensation, $\Delta H_{\text{cond}}^\circ = -44 \text{ kJ mol}^{-1}$), $c = \exp(-[\Delta H_1^\circ - \Delta H_{\text{cond}}^\circ]/RT)$, and n is a unitless fitting parameter that represents the maximum number of layers of adsorbed species and is related to the pore size and properties of the adsorbent, R is the gas constant and T is temperature in K. The best fit parameters using the modified BET adsorption model to the data shown in Figure 4.9 a,b,d are listed in Table 4.2. The outermost right axis in these figures shows water coverage in monolayers calculated relative to m_{ML} obtained from the fits.

Table 4.2 Best Fit Parameters for Gas Phase Water Adsorption on Polymeric Organic Films at 298 K Shown in Figure 4.9^a

polymeric organic film	modified BET adsorption model			
	H ₂ O Coverage at ML (g m^{-2}) (% RH at 1 ML)	n	c	ΔH_1° (kJ mol^{-1})
polycatechol	5.2 ± 0.3 (16%)	6.6 ± 2	28 ± 13	-52 ± 24
polyguaiaicol	3.1 ± 1.4 (45%)	5.7 ± 1	1.6 ± 0.5	-45 ± 22
Fe-polymuconate	16 ± 0.5 (14%)	14 ± 3	72 ± 3	-55 ± 3
Fe-polyfumarate	Langmuir–Sips adsorption model			
	H ₂ O Coverage at saturation (g m^{-2})	n	K_1	K_2
Fe-polyfumarate	16 ± 2.4 (43%)	5.4 ± 2	1.3 ± 0.6	212 ± 100

^asat = saturation surface coverage.

The trend in the values of the best-fit parameters: m_{ML} , n , and c for water adsorption of polycatechol, polyguaiaicol, and Fe-polymuconate reflects their affinity to water based on their chemical structure. Both polycatechol and polyguaiaicol are more hydrophobic than Fe-

polymuconate. Both organic polymer films with substituted benzene ring units result in the formation of a water monolayer at later % RH values (16 and 45%) compared to 14% for Fe-polymuconate, which is an organometallic film with aliphatic dicarboxylic acid units connected through iron centers that favor water as ligands. This higher affinity toward water is evident in the values of n , where Fe-polymuconate takes up nearly double the maximum number of layers observed for polycatechol and polyguaiacol. In addition, the formation of the monolayer water coverage on Fe-polymuconate is more exothermic than on polycatechol and polyguaiacol. The presence of the methyl substituents in polyguaiacol compared to hydroxyl groups in polycatechol resulted in a value for ΔH_1° close to $\Delta H_{\text{cond}}^\circ$. This result suggests that water-water hydrogen bonding interactions dominate over water-polyguaiacol hydrogen bonding. For polycatechol, hydroxyl substituents are involved in hydrogen bonding with surface water resulting in higher ΔH_1° than $\Delta H_{\text{cond}}^\circ$. The shape of the water adsorption isotherm on Fe-polymuconate in Figure 4.9c is different from that observed for Fe-polymuconate. The S-shaped curve is characteristic of a Type V isotherm typically observed for gas phase adsorption on porous materials, where pore condensation takes place.⁵⁹ A similar isotherm shape was observed for N₂ gas adsorption at 77 K as shown in Figure 4.10. The model used to fit the S shaped isotherm shown in Figure 4.9c is the Langmuir-Sips isotherm model, which accounts for monolayer adsorption according to the Langmuir isotherm at low pressure, and capillary condensation described by the Sips isotherm at moderate to high pressure⁶⁰

$$m = m_{\text{sat}} \left[\frac{K_1(\text{RH})}{1 + K_1(\text{RH})} + \frac{K_2(\text{RH})^n}{1 + K_2(\text{RH})^n} \right] \dots\dots\dots 4.2$$

where m and RH are defined above, m_{sat} is the saturation surface coverage (g m^{-2}), n is a fitting parameter characteristic of the heterogeneity of the surface, K_1 and K_2 are surface affinity parameters at low and moderate/high vapor pressure regions, respectively. As summarized by Inglezakis *et al.*,⁶⁰ this composite isotherm was used to describe the adsorption of polar and

nonpolar organic compounds on mesoporous silicate and water adsorption on a silica-based high-purity spherical gel.

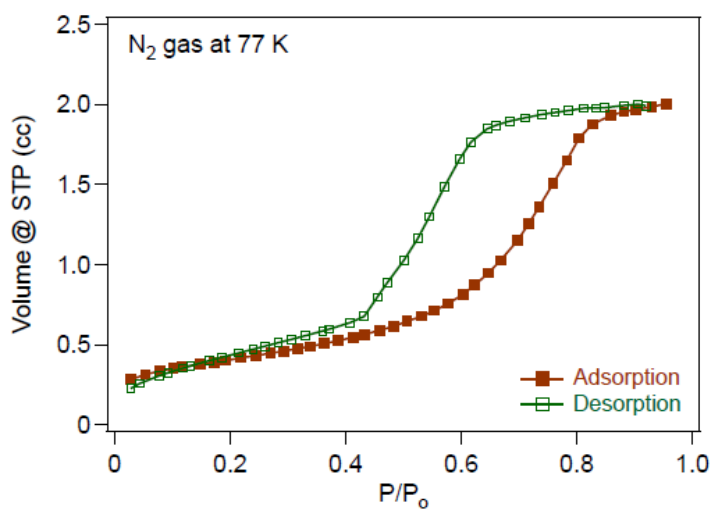


Figure 4.10 Adsorption isotherm of N₂ gas on Fe-polyfumarate at 77 K confirming the porous structure of this organometallic material.

The best-fit parameters using the Langmuir-Sips adsorption model to the data shown in Figure 4.9c are listed in Table 4.2.

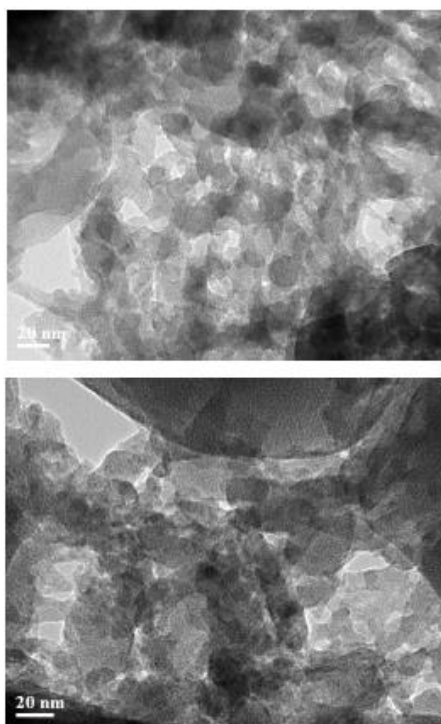


Figure 4.11 High resolution transmission electron microscopy (HR-TEM) images for Fe-polyfumarate showing the pore structure of this material.

The outermost right axis in this figure shows water coverage in monolayers calculated relative to m_{sat} , obtained from the fit. The S-shaped isotherm is a direct consequence of the porous structure of Fe-polyfumarate, which is apparent in the high-resolution transmission electron microscopy images shown in Figure 4.11. The value m_{sat} (corresponding to 1 ML) occurred at 43% RH indicating complete condensation of water in the pores. The values of K_1 and K_2 suggest that water–water interactions due to condensation in the pores at moderate to high % RH are more favorable than water-polyfumarate interactions at low % RH. Also shown in Figure 4.9 is the extent of water desorption as a result of decreasing % RH from the highest value reached during adsorption. Within the uncertainty and over the time frame of the measurements, there is no hysteresis observed in the case of polycatechol and polyguaiacol because of weak adsorbate-adsorbent and adsorbate-adsorbate interactions. The Fe-polyfumarate sample shows no hysteresis above 50% RH, and water retention at RH values below 40% RH. The largest hysteresis is observed in the case of Fe-polyumuconate, where at 30% RH, for example, the sample contains nearly double the amount of water in the desorption part relative to the adsorption part of the experiment. This suggests that the desorption kinetics are slower than adsorption kinetics over the 30 min allowed for equilibrium at % RH. Such behavior would have consequences on the chemical and physical properties of aerosols containing organometallic polymers.

4.6 Conclusion

In this study, the hygroscopic properties of organic and organometallic polymeric particles formed in iron catalyzed reactions with aromatic and aliphatic dicarboxylic acid compounds detected in field-collected SOA, were investigated. The structure of surface water was studied using DRIFTS revealed that water bonding with organic functional groups acting as hydrogen bond acceptors caused shifts in their vibrational modes. There was also evidence for weak and strong hydrogen bonding networks that suggest cluster formation with water-water and water-

organics interactions, respectively. In addition, gas phase water adsorption and desorption isotherms collected as a function of RH was best modeled using a modified Type II multilayer BET adsorption model on nonporous materials, namely polycatechol, polyguaiacol, and Fe-polymuconate. Water adsorption on porous Fe-polyfumarate was best described using a Type V adsorption model, namely the Langmuir-Sips model that accounts for condensation in pores. The results presented herein are significant because global climate models²⁵ need better parametrization of the hygroscopic properties and chemical reactivity of SOA. Of the organic and organometallic polymeric particles studied here, the shape of the adsorption isotherm of water on polyguaiacol is similar to particle growth factor curves (ranging from 1.1 to 1.2) obtained for SOA formed by oxidation of cycloalkenes, monoterpenes, and sesquiterpenes.⁶¹ Gas phase water adsorption isotherms on the other polymers, polycatechol and Fe-polymuconate, show that they have higher affinity for water, particularly below 20% RH relative to other SOA. The hygroscopic behavior of Fe-polyfumarate is the most unique given its porous structure, and the shape of the adsorption isotherm has not been observed before for atmospheric aerosols. This adsorption isotherm resembles those obtained from water uptake on metal-organic frameworks owing to their extensive network of pores.⁶² As mentioned in the introduction, water structure and hygroscopic properties are the first step to understanding the surface chemistry of atmospheric aerosols. The organic polymers studied have chemical structures (unsaturated bonds, benzene rings, iron centers) that cause their light absorbing properties to appear in the UV-visible region. The fact that these materials can adsorb water even at low % RH suggests that water will play a role in their photo reactivity and electron transfer processes, whether at the surface or in the pores as in the case of Fe-polyfumarate. Hence, these reactions will impact their aging, atmospheric residence time, and impact on gas phase composition.

4.7 References

- (1) Fairbrother, H.; Geiger, F. M.; Grassian, V. H.; Hemminger, J. C. Physical chemistry of environmental interfaces. *J. Phys. Chem. C* **2009**, *113*, 2035.
- (2) Signorell, R.; Bertram, A. K. Physical chemistry of aerosols. *Phys. Chem. Chem. Phys.* **2009**, *11*, 7741-8104.
- (3) Finlayson-Pitts, B. J. Reactions at surfaces in the atmosphere: Integration of experiments and theory as necessary (but not necessarily sufficient) for predicting the physical chemistry of aerosols. *Phys. Chem. Chem. Phys.* **2009**, *11*, 7760-7779.
- (4) Jeffrey, G. An introduction to hydrogen bonding; Oxford University Press: New York, **1997**.
- (5) Allen, H. C.; Casillas-Ituarte, N. N.; Sierra-Hernández, M. R.; Chen, X.; Tang, C. Y. Shedding light on water structure at air-aqueous interfaces: Ions, lipids, and hydration. *Phys. Chem. Chem. Phys.* **2009**, *11*, 5538-5549.
- (6) Hore, D. K.; Walker, D. S.; Richmond, G. L. Water at hydrophobic surfaces: When weaker is better. *J. Am. Chem. Soc.* **2008**, *130*, 1800-1801.
- (7) Moussa, S. G.; McIntire, T. M.; Szőri, M.; Roeselová, M.; Tobias, D. J.; Grimm, R. L.; Hemminger, J. C.; Finlayson-Pitts, B. J. Experimental and Theoretical Characterization of Adsorbed Water on Self-Assembled Monolayers: Understanding the Interaction of Water with Atmospherically Relevant Surfaces. *J. Phys. Chem. A* **2009**, *113*, 2060-2069.
- (8) Nissenon, P.; Dabdub, D.; Das, R.; Maurino, V.; Minero, C.; Vione, D. Evidence of the water-cage effect on the photolysis of NO_3^- and FeOH_2^+ . Implications of this effect and of H_2O_2 surface accumulation on photochemistry at the air-water interface of atmospheric droplets. *Atmos. Environ.* **2010**, *44*, 4859-4866.
- (9) Kameel, F. R.; Riboni, F.; Hoffmann, M. R.; Enami, S.; Colussi, A. J. Fenton oxidation of gaseous isoprene on aqueous surfaces. *J. Phys. Chem. C* **2014**, *118*, 29151-29158.

- (10) Nissenon, P.; Knox, C. J. H.; Finlayson-Pitts, B. J.; Phillips, L. F.; Dabdub, D. Enhanced photolysis in aerosols: Evidence for important surface effects. *Phys. Chem. Chem. Phys.* **2006**, *8*, 4700-4710.
- (11) Rubasinghege, G.; Grassian, V. H. Role(s) of adsorbed water in the surface chemistry of environmental interfaces. *Chem. Commun.* **2013**, *49*, 3071-3094.
- (12) Trainic, M.; Abo Riziq, A.; Lavi, A.; Rudich, Y. Role of Interfacial Water in the Heterogeneous Uptake of Glyoxal by Mixed Glycine and Ammonium Sulfate Aerosols. *J. Phys. Chem. A* **2012**, *116*, 5948–5957.
- (13) Tang, M.; Cziczo, D. J.; Grassian, V. H. Interactions of water with mineral dust aerosol: Water adsorption, hygroscopicity, cloud condensation, and ice nucleation. *Chem. Rev.* **2016**, *116*, 4205–4259.
- (14) Ibrahim, S.; Romanias, M. N.; Alleman, L. Y.; Zeineddine, M. N.; Angeli, G. K.; Trikalitis, P. N.; Thevenet, F. Water interaction with mineral dust aerosol: Particle size and hygroscopic properties of dust. *ACS Earth Space Chem.* **2018**, *2*, 376-386.
- (15) Kuwata, M.; Martin, S. T. Phase of atmospheric secondary organic material affects its reactivity. *Proc. Natl. Acad. Sci. U.S.A.* **2012**, *109*, 17354-17359.
- (16) Shiraiwa, M.; Ammann, M.; Koop, T.; Poschl, U. Gas uptake and chemical aging of semisolid organic aerosol particles. *Proc. Natl. Acad. Sci. U.S.A.* **2011**, *108*, 11003-11008.
- (17) Nguyen, T. K. V.; Zhang, Q.; Jimenez, J. L.; Pike, M.; Carlton, A. G. Liquid water: Ubiquitous contributor to aerosol mass. *Environ. Sci. Technol. Lett.* **2016**, *3*, 257-263.
- (18) Guo, H.; Xu, L.; Bougiatioti, A.; Cerully, K. M.; Capps, S. L.; Hite, J. R.; Carlton, A. G.; Lee, S.-H.; Bergin, M. H.; Ng, N. L.; Nenes, A.; Weber, R. J. Fine-particle water and pH in the southeastern united states. *Atmos. Chem. Phys.* **2015**, *15*, 5211-5228.

- (19) Freedman, M. A. Phase separation in organic aerosol. *Chem. Soc. Rev.* **2017**, *46*, 7694-7705.
- (20) Song, M.; Marcolli, C.; Krieger, U. K.; Lienhard, D. M.; Peter, T. Morphologies of mixed organic/inorganic/aqueous aerosol droplets. *Faraday Discuss.* **2013**, *165*, 289-316.
- (21) Zhang, R.; Khalizov, A.; Wang, L.; Hu, M.; Xu, W. Nucleation and growth of nanoparticles in the atmosphere. *Chem. Rev.* **2012**, *112*, 1957-2011.
- (22) Pöschl, U. Atmospheric Aerosols: Composition, Transformation, Climate and Health Effects. *Angew. Chem.* **2005**, *44*, 7520-7540.
- (23) Farmer, D. K.; Cappa, C. D.; Kreidenweis, S. M. Atmospheric processes and their controlling influence on cloud condensation nuclei activity. *Chem. Rev.* **2015**, *115*, 4199-4217.
- (24) Ziemann, P. J.; Atkinson, R. Kinetics, products, and mechanisms of secondary organic aerosol formation. *Chem. Soc. Rev.* **2012**, *41*, 6582-6605.
- (25) Kanakidou, M.; Seinfeld, J. H.; Pandis, S. N.; Barnes, I.; Dentener, F. J.; Facchini, M. C.; Van Dingenen, R.; Ervens, B.; Nenes, A.; Nielsen, C. J.; et al. Organic aerosol and global climate modelling: A review. *Atmos. Chem. Phys.* **2005**, *5*, 1053-1123.
- (26) Swietlicki, A.; Laskin, J.; Nizkorodov, S. A. Chemistry of atmospheric brown carbon. *Chem. Rev.* **2015**, *115*, 4335-4382.
- (27) Al-Abadleh, H. A. Review of the bulk and surface chemistry of iron in atmospherically relevant systems containing humic-like substances. *RSC Adv.* **2015**, *5*, 45785-45811.
- (28) Ito, A. Atmospheric processing of combustion aerosols as a source of bioavailable iron. *Environ. Sci. Technol. Lett.* **2015**, *2*, 70-75.
- (29) Oakes, M.; Weber, R. J.; Lai, B.; Russell, A.; Ingall, E. D. Characterization of iron speciation in urban and rural single particles using xanes spectroscopy and micro x-ray

- fluorescence measurements: Investigating the relationship between speciation and fractional iron solubility. *Atmos. Chem. Phys.* **2012**, *12*, 745-756.
- (30) Ault, A. P.; Peters, T. M.; Sawvel, E. J.; Casuccio, G. S.; Willis, R. D.; Norris, G. A.; Grassian, V. H. Single-particle sem-edx analysis of iron-containing coarse particulate matter in an urban environment: Sources and distribution of iron within Cleveland, Ohio. *Environ. Sci. Technol.* **2012**, *46*, 4331–4339.
- (31) Guasco, T. L.; Cuadra-Rodriguez, L. A.; Pedler, B. E.; Ault, A. P.; Collins, D. B.; Zhao, D.; Kim, M. J.; Ruppel, M. J.; Wilson, S. C.; Pomeroy, R. S.; Grassian, V. H.; Azam, F.; Bertram, T. H.; Prather, K. A. Transition metal associations with primary biological particles in sea spray aerosol generated in a wave channel. *Environ. Sci. Technol.* **2014**, *48*, 1324-1333.
- (32) Li, W.; Shao, L.; Shi, Z.; Chen, J.; Yang, L.; Yuan, Q.; Yan, C.; Zhang, X.; Wang, Y.; Sun, J.; Zhang, Y.; Shen, X.; Wang, Z.; Wang, W. Mixing state and hygroscopicity of dust and haze particles before leaving asian continent. *J. Geophys. Res.: Atmos.* **2014**, *119*, 1044-1059.
- (33) Wang, V. H. L.; Edwards, R.; Bowie, A. R.; Keywood, M.; Williams, A. G.; Chambers, S. D.; Selleck, P. W.; Desservettaz, M.; Mallet, M. D.; Paton-Walsh, C. Dry season aerosol iron solubility in tropical northern australia. *Atmos. Chem. Phys.* **2016**, *16*, 12829-12848.
- (34) Shi, Z.; Krom, M. D.; Jickells, T. D.; Bonneville, S.; Carslaw, K. S.; Mihalopoulos, N.; Baker, A. R.; Benning, L. G. Impacts on iron solubility in the mineral dust by processes in the source region and the atmosphere: A review. *Aeolian Res.* **2012**, *5*, 21-42.
- (35) Shi, Z.; Krom, M. D.; Bonneville, S.; Benning, L. G. Atmospheric processing outside clouds increases soluble iron in mineral dust. *Environ. Sci. Technol.* **2015**, *49*, 1472-1477.

- (36) Slikboer, S.; Grandy, L.; Blair, S. L.; Nizkorodov, S. A.; Smith, R. W.; Al-Abadleh, H. A. Formation of light absorbing soluble secondary organics and insoluble polymeric particles from the dark reaction of catechol and guaiacol with Fe(III). *Environ. Sci. Technol.* **2015**, *49*, 7793-7801.
- (37) Tran, A.; Williams, G.; Younus, S.; Ali, N. N.; Blair, S. L.; Nizkorodov, S. A.; Al-Abadleh, H. A. Efficient formation of lightabsorbing polymeric nanoparticles from the reaction of soluble Fe(III) with C4 and C6 dicarboxylic acids. *Environ. Sci. Technol.* **2017**, *51*, 9700-9708.
- (38) Ofner, J.; Krüger, H.-U.; Grothe, H.; Schmitt-Kopplin, P.; Whitmore, K.; Zetzsch, C. Physico-chemical characterization of SOA derived from catechol and guaiacol - a model substance for the aromatic fraction of atmospheric HULIS. *Atmos. Chem. Phys.* **2011**, *11*, 1–15.
- (39) Cowen, S. Heterogeneous photodegradation of tannic acid studied by diffuse reflectance FTIR. MSc Thesis, University of Guelph, Guelph, ON, Canada, **2009**.
- (40) Cowen, S.; Al-Abadleh, H. A. DRIFTS studies on the photodegradation of tannic acid as a model for HULIS in atmospheric aerosols. *Phys. Chem. Chem. Phys.* **2009**, *11*, 7838-7847.
- (41) Tofan-Lazar, J.; Situm, A.; Al-Abadleh, H. A. DRIFTS studies on the role of surface water in stabilizing catechol-iron(III) complexes at the gas/solid interface. *J. Phys. Chem. A* **2013**, *117*, 10368-10380.
- (42) Kobayashi, S.; Makino, A. Enzymatic polymer synthesis: An opportunity for green polymer chemistry. *Chem. Rev.* **2009**, *109*, 5288-5353.
- (43) Faure, E.; Falentin-Daudré, C.; Jérôme, C.; Lyskawa, J.; Fournier, D.; Woisel, P.; Detrembleur, C. Catechols as versatile platforms in polymer chemistry. *Prog. Polym. Sci.* **2013**, *38*, 236-270.

- (44) Dubey, S.; Singh, D.; Misra, R. A. Enzymatic synthesis and various properties of poly(catechol). *Enzyme Microb. Technol.* **1998**, *23*, 432-437.
- (45) Doerge, D. R.; Divi, R. L.; Churchwell, M. I. Identification of the colored guaiacol oxidation product produced by peroxidases. *Anal. Biochem.* **1997**, *250*, 10-17.
- (46) Silverstein, R. M.; Webster, F. X. Spectrometric identification of organic compounds, 6th ed.; Wiley: New York, **1998**.
- (47) Slipchenko, L. V.; Gordon, M. S. Water-Benzene Interactions: An Effective Fragment Potential and Correlated Quantum Chemistry Study. *J. Phys. Chem. A* **2009**, *113*, 2092-2102.
- (48) Wang, H.; Agmon, N. Protonated water dimer on benzene: Standing eigen or crouching Zundel? *J. Phys. Chem. A* **2015**, *119*, 2658-2667.
- (49) Gierszal, K. P.; Davis, J. G.; Hands, M. D.; Wilcox, D. S.; Slipchenko, L. V.; Ben-Amotz, D. π -Hydrogen Bonding in Liquid Water. *J. Phys. Chem. Lett.* **2011**, *2*, 2930-2933.
- (50) Gómez-Zaleta, B.; Gómez-Balderas, R.; Hernández-Trujillo, J. Theoretical analysis of hydrogen bonding in catechol- n (H₂O) clusters ($n = 0...3$). *Phys. Chem. Chem. Phys.* **2010**, *12*, 4783-4790.
- (51) Cheng, T. C.; Bandyopadhyay, B.; Mosley, J. D.; Duncan, M. A. IR Spectroscopy of Protonation in Benzene-Water Nanoclusters: Hydronium, Zundel, and Eigen at a Hydrophobic Interface. *J. Am. Chem. Soc.* **2012**, *134*, 13046-13055.
- (52) Lappi, S. E.; Smith, B.; Franzen, S. Infrared spectra of H₂ ¹⁶O, H₂¹⁸O and D₂O in the liquid phase by single-pass attenuated total internal reflection spectroscopy. *Spectrochim. Acta, Part A* **2004**, *60*, 2611-2619.

- (53) Walrafen, G. E. Raman and infrared spectral investigations of water structure. In *Water a Comprehensive Treatise*; Franks, F., Ed.; Plenum Press: New York, **1972**; Vol. 1, pp 151-214.
- (54) Heger, M.; Mata, R. A.; Suhm, M. A. Soft hydrogen bonds to alkenes: the methanol-ethene prototype under experimental and theoretical scrutiny. *Chem. Sci.* **2015**, *6*, 3738-3745.
- (55) Nichols, B. R.; Rapa, C.; Costa, V.; Hinrichs, R. Z. Heterogeneous and Photochemical Reactions of Solid Benzophenone-Catechol Films with NO₂. *J. Phys. Chem. C* **2009**, *113*, 2111-2119.
- (56) Wentworth, G. R.; Al-Abadleh, H. A. DRIFTS studies on the photosensitized transformation of gallic acid by iron(III) chloride as a model for HULIS in atmospheric aerosols. *Phys. Chem. Chem. Phys.* **2011**, *13*, 6507-6516.
- (57) Atkins, P. W.; de Paula, J. *Physical Chemistry*, 7th ed.; W. H. Freeman and Company: New York, **2008**.
- (58) Goodman, A. L.; Bernard, E. T.; Grassian, V. H. Spectroscopic study of nitric acid and water adsorption on oxide particles: Enhanced nitric acid uptake kinetics in the presence of adsorbed water. *J. Phys. Chem. A* **2001**, *105*, 6443-6457.
- (59) Sing, K. S. W. Reporting physisorption data for gas/solid systems with special reference to the determination of surface area and porosity (Provisional). *Pure Appl. Chem.* **1982**, *54*, 2201-2218.
- (60) Inglezakis, V. J.; Pouloupoulos, S. G.; Kazemian, H. Insights into the S-shaped sorption isotherms and their dimensionless forms. *Microporous Mesoporous Mater.* **2018**, *272*, 166-176.
- (61) Varutbangkul, V.; Brechtel, F. J.; Bahreini, R.; Ng, N. L.; Keywood, M. D.; Kroll, J. H.; Flagan, R. C.; Seinfeld, J. H.; Lee, A.; Goldstein, A. H. Hygroscopicity of secondary

organic aerosols formed by oxidation of cycloalkenes, monoterpenes, sesquiterpenes, and related compounds. *Atmos. Chem. Phys.* **2006**, *6*, 2367-2388.

- (62) Furukawa, H.; Gándara, F.; Zhang, Y.-B.; Jiang, J.; Queen, W. L.; Hudson, M. R.; Yaghi, O. M. Water Adsorption in Porous Metal-Organic Frameworks and Related Materials. *J. Am. Chem. Soc.* **2014**, *136*, 4369-4381.

Chapter 5 Iron-containing Metal-Organic Frameworks (MOFs) in Enhancing the Selective Catalytic Reduction (SCR) of NO_x to Nitrogen Gas

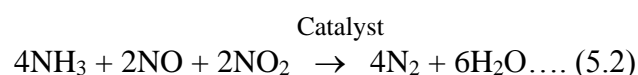
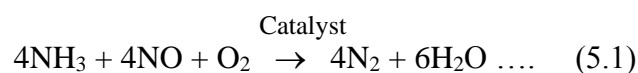
5.1 Abstract

This chapter describes systematic investigation on the reactivity of Fe-BTC and CoFe₂O₄ with urea as the *in situ* source of ammonia gas as a reductant to reduce NO_(g) by DRIFTS. It was found that the rate of conversion of NO_(g) in the presence of CoFe₂O₄/8%urea was 2.3±0.03 ppm m⁻² min⁻¹, whereas in the presence of Fe-BTC//8%urea, the rate of conversion of NO_(g) was 0.22±0.04 ppm m⁻² min⁻¹.

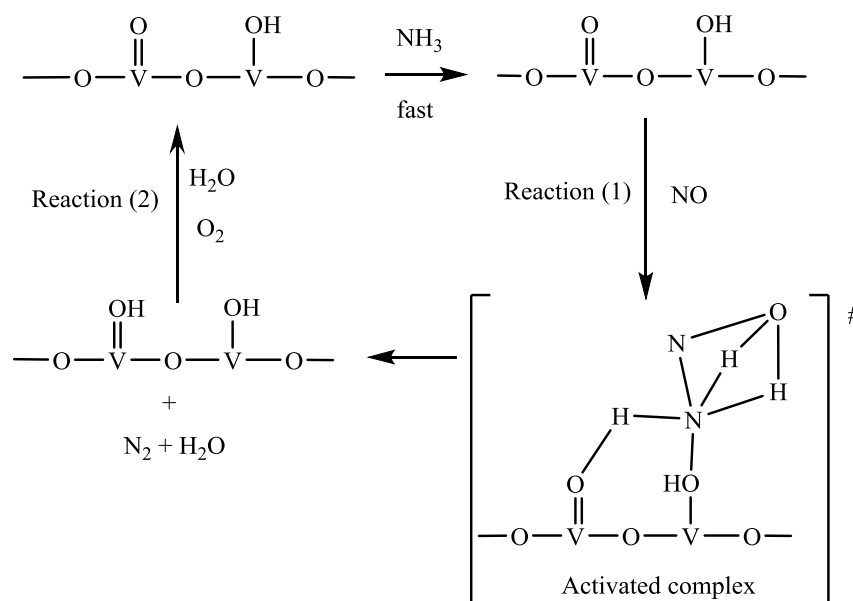
5.2 Introduction

Recently, there has been increasing environmental awareness due to the “air pollution” that have harmful effect on living beings, plants and materials.¹ It has been found that the major contribution to this pollution are anthropogenic and occurs due to the burning of fossil fuels (such as coal, petroleum and natural gas), vehicles and other ignition processes. Nitrogen oxides (NO_x, mainly NO and NO₂) are one of the key components of air contaminants, generated from combustion processes. NO_x are known as primary pollutant in the atmosphere and react to form photochemical smog and acid rain as well as take part in ozone layer depletion.^{2,3} Moreover, they are harmful for human health and can cause damage to the respiratory systems. Considering the toxicity, it has become an important environmental concern to control or remove NO_x from the air. Though NO_x emission occurs from various anthropogenic activities, industrial sources such as power plants and mobile engines are considered mainly responsible for the release of NO_x into the atmosphere. Nitrogen oxides are highly reactive and complete removal of these gases is barely possible. However, NO_x emanation can be controlled and classified into three categories such as pre-combustion treatment, combustion modification and post-combustion treatment. It appears that pre-combustion as well as combustion modification can make significant reduction of NO_x.

However, the success is modest and typically less than 50%.⁴ Therefore, during recent years, more focuses have been made for the development of technologies, associated with post-combustion treatment of NO_x to control and reduce the level of emission.⁵ The selective catalytic reduction (SCR) is one of the most recognized and effective technologies to remove NO_x from the air by reducing it into environmentally friendly N₂ gas. In this process, a reducing agent along with catalysts is added to the flue gas of NO_x at moderate temperature. NH₃ can act as a reducing agent in SCR of NO_x and has been reported as the most efficient, highly selective and cost-effective technologies for NO_x emission control.³ The reactions that occur during the NH₃-SCR of NO_x are given in the following equations.



The first reaction (5.1) is known as the “standard” SCR reaction. It takes place in the presence of oxygen. However, it turned out that equimolar amounts of NO and NO₂ in the system facilitate the reaction to be faster than the “standard” reaction. As the catalyst plays an important role in the SCR process, recent studies focused on the improvement of the catalyst and its efficiency. Earlier, oxides of Pt, Co, Ni, Fe and Cr were used as catalysts for the SCR. However, due to some drawbacks (required high temperature that may end up with forming explosive ammonium nitrate) these oxides required replacing. In 1960, Japan and the United States made progress in SCR and developed an inexpensive and highly robust V₂O₅/TiO₂ catalyst, that was efficient at medium temperatures (Scheme 5.1).²



Scheme 5.1 Reaction mechanism for the NH_3 -SCR over vanadium oxide catalysts.²

However, it was observed that vanadium catalysts lacked thermal stability as well as oxidized SO_2 into SO_3 , a very harmful acidic gas. Later, in 1970, modified vanadium-based catalysts, in particular WO_3 or MoO_3 doped $\text{V}_2\text{O}_5/\text{TiO}_2$, have been extensively employed to remove NO_x , mostly from stationary sources due to their high denitrification efficiency. Nevertheless, there are some disadvantages for these catalysts as they can be deactivated during the application process. The deactivation can take place through several ways such as poisoning, fouling, thermal degradation and vapor compound formation. Moreover, there can be vapor-solid reactions between vapor and catalyst surface as well as solid-solid reactions between carrier of the catalyst and promoter that are responsible for the deactivation of the catalysts. In addition, these catalysts offer low range of operating temperature (300-400 °C). Besides, V_2O_5 is toxic, has lower selectivity towards N_2 at high temperature and is expensive. Last but not the least, vanadium is known as a pollutant to the environment and is hard to dispose of.⁴ All these disadvantages questioned the application of vanadium-based catalysts in the industrial arena.

Recently, modified activated coke (AC) has been used as a catalyst for the de NO_x in NH_3 -SCR. AC is a porous carbon material and has similar pore structure as activated carbon.⁵

However, it is not fully activated. It is low cost and possess higher mechanical strength. The existing activated coke by itself, has poor deNO_x performance at low temperature. However, there has been a considerable improved performance of activated coke as a catalyst after structural modification. AC can be modified through doping using various metal oxides such as Fe₂O₃, Co₃O₄, CeO₂ and CrO₃. It was found that metal oxides helped to enhance the performance of AC, as they possess various oxidation states and redox properties.⁵ Figure 5.1 shows the possible mechanism of NO_x removal via NH₃-SCR, where Fe_xCo_yCe_zO_m/AC, a modified activated coke, act as a catalyst. In this work, AC was modified by Fe₂O₃, Co₂O₃ and CeO₂ with incipient wetness impregnation method. The modified AC was employed to remove NO_x from simulated flue gas in a lab-scale fixed-bed system at 100-350 °C.

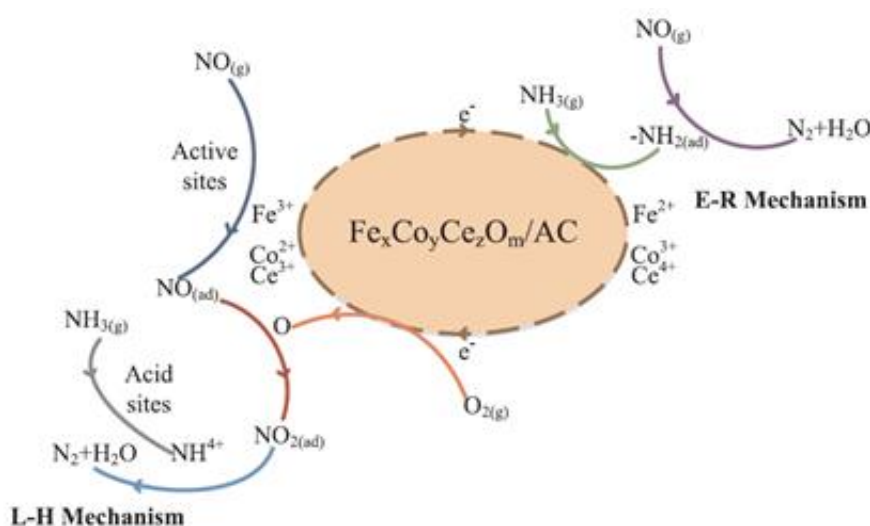


Figure 5.1 Mechanism of NO conversion to N₂ on the surface of Fe_xCo_yCe_zO_m supported on activated carbon.⁵(adapted with permission from Ref 5)

In the first step of the SCR reactions, the adsorption of NH_{3(g)} on the acid sites or metallic atom is well documented. NH₄⁺_(ad) and NH_{2(ad)} are the intermediate products that appear upon the adsorption of NH_{3(g)}. NH₄⁺_(ad) can be combined with NO_{2(ad)} to produce NH₄NO₂ followed by decomposition to N₂ and H₂O according to the Eley Rideal (E-R) mechanism. On the other hand, NH_{2(ad)} could react with NO_(g) to generate NH₂NO, followed by decomposition to N₂ and H₂O according to the Langmuir Hinshelwood (L-H) mechanism. It appeared that modified AC

plays an important role in reduction of NO(g) and the results revealed that the abundance of active sites and good redox cycle among Fe, Co and Ce, facilitated the enhanced performance of the catalysts.⁵

Mn-based catalysts also have drawn much attention due to their enhanced catalytic performance for SCR at low temperatures.⁶ It has been shown that, H₂O and SO₂ inhibits the activity of pure MnO_x catalysts in real conditions. However, Mn-based catalysts with multiple metal oxides support exhibit enhanced stability such as Cu-Mn, Sn-Mn, Fe-Mn, Nb-Mn, Li-Mn, Eu-Mn and Ni-Mn. These catalysts show decent SCR performances and N₂ selectivity. Still, their performance towards H₂O and SO₂ were questionable and not satisfactory at lower temperatures below 250 °C. Recently, some modified Mn-based catalysts were synthesized and performed well against H₂O and SO₂ inhibitors-such as MnO_x-CeO₂. These multi-metal oxides have special crystal shape and structures, along with modified TiO₂ and carbon support. It was observed that MnO_x-CeO₂ catalysts possess outstanding SCR performance as a result of synergic behavior between Mn and Ce metal center. This behavior helps to enhance the quality, acidity of the acid sites and capability to store or oxygen.⁶ Another kind of Mn-Based catalysts have been reported and synthesized with hollow porous Mn_xCo_{3-x}O₄ nanocages. These nanoparticles were derived from Mn₃[Co(CN)₆]₂nH₂O, having a structure nanocube, like metal-organic frameworks (MOFs) via a self-assemble method. It was found that their uniform structural distribution and strong interaction between Mn and Co, are the reasons behind their larger surface area, more active sites and enhanced catalytic cycle. Moreover, flexible valence states and excellent redox ability of Mn-based catalysts were found favorable to the low-temperature SCR activity.

Recently, metal-organic frameworks (MOFs) have emerged as a new class of useful materials and are the latest addition to the list after zeolites for the reduction of NO₂.⁷⁻¹² MOFs (also known as porous coordination polymers or PCPs) have drawn much attention due to their

various applications in the field of chemistry for the past two decades.¹² These materials have high surface area and tunable pore size which may offer many kinds of industrial application in near the future. However, they are already well known for their application in gas separation and storage,¹³ capture of greenhouse gases,¹⁴ adsorption of volatile organic compounds,¹⁵ drug delivery and sensors, and in the area of heterogeneous catalysis.¹² In comparison to the typical adsorbents, the advantages of MOFs as adsorbents due to their various compositions and structure types, tunable pore size, high surface area, and coordinatively unsaturated or saturated metal sites to control the adsorption ability.¹⁶⁻¹⁸

Fe-based structures are known as the most promising type of MOF materials considering their relatively high thermal stability, low cost, high biocompatibility and low toxicity. Fe-BTC (BTC: 1,3,5-benzenetricarboxylate) is one of the MOFs that has been commercialized by BASF under the name of Basolite (Basolite A100, C300, F300, Z1200 and Basosiv M050 or aluminum terephthalate MIL-53, copper trimesate HKUST-1, iron trimesate, zinc imidazolate or ZIF-8, and magnesium formate, respectively). Fe-BTC has iron as a metal center and BTC as organic linker. Basolite Fe-BTC can be prepared from the reaction of trimesic benzene-1,3,5-tricarboxylic acid and iron salt. Figure 5.2 shows the structure of Fe-BTC where Fe_2 clusters are coordinated to carboxylate groups to form paddle wheel groups.

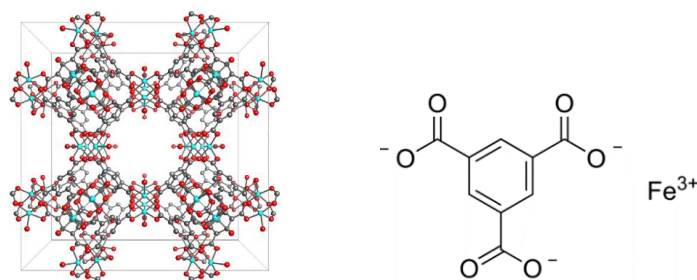


Figure 5.2 The structure of Fe-BTC (carbon atoms gray, oxygen atoms red, and iron atoms light-blue).¹⁹

The properties of Fe-BTC are given in Table 5.1.²⁰

Table 5.1: Properties of Fe-BTC

Properties	Fe-BTC
Metal	Fe
Linker	BTC
Iron mass content	25
Carbon mass content	32
Crystal Structure	unknown
BET surface area (m ² /g)	771
Pore dimension	21.7
Particle size (in EtOH) (μm)	5
Lewis acid	Strong
Lewis base	Weak
Bulk density	0.16-0.35 g/cm ³

Fe-BTC (benzene-1, 3, 5-tricarboxylate) metal-organic frameworks have been employed for various purposes such as catalysis, separation and CO₂ capture. It has been reported for the first time to be used as a combined catalyst and carbon source for the synthesis of multi-walled carbon nanotubes (MWCNTs).¹⁹ Fe-BTC also been successfully used for separation of small organic compounds in the liquid phase. It was found that separation with the Fe-BTC was achieved because of the specific interactions between the solutes and Fe³⁺ sites. Fe-BTC exhibits high catalytic activity for a large variety of reactions requiring Lewis acidity, able to carbon capture and storage (CCS).²¹ Recently, Fe-BTC has been used as a candidate for combustion catalysis of solid propellants containing ammonium perchlorate. Thermal decomposition of ammonium perchlorate was enhanced in presence of the Fe-BTC.²² Most recently, Fe-BTC was introduced for CO₂ capture along with Cu-BTC and ZIF-8 MOFs. It was found that Cu-BTC involved in dehydration reactions, as well as the interaction between copper and CO₂ molecule, whereas for Fe-BTC and ZIF-8, physical driving force was detected for CO₂ adsorption measurements.²³

5.3 Objectives

As NO_x are very harmful air pollutants, it is important to develop nontoxic catalysts which have low costs, stability, high deNO_x activity at wide temperature range and favorable tolerance of other components in the flue gas. Considering the properties (such as highly active catalyst, higher surface area and pore size) it is obvious that Fe-BTC might be the better candidate for the reduction $\text{NO}_{(g)}$ in NH_3 -SCR. In order to compare with Fe-BTC, we also studied CoFe_2O_4 nano materials (Figure 5.3) as a catalyst for the deNO_x via NH_3 -SCR. The major objective of the experimental activities is to systematically investigate the reactivity of Fe-BTC and CoFe_2O_4 with urea as the *in situ* source of ammonia gas as a reductant to reduce $\text{NO}_{(g)}$. Experiments were conducted to monitor changes to the surface of the solid materials and to identify gas phase products.

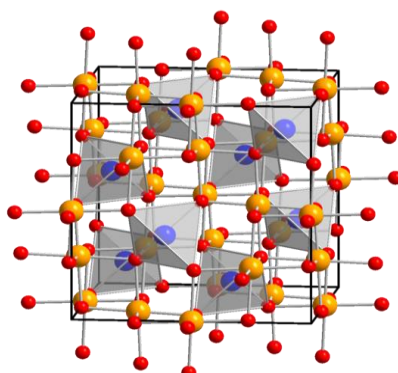


Figure 5.3 Structure of CoFe_2O_4 ($43 \text{ m}^2/\text{g}$).²⁴

5.4 Experimental

5.4.1 Chemicals

Most of the chemicals were used as received without further purification. Fe-BTC from Sigma-Aldrich (Basolite F300 Cat. No. 690872); Cobalt iron nano powder from US research Nanomaterials Inc. (CoFe_2O_4 , 99.9%, CAS# 12052-28-7); $\text{NO}_{(g)}$ from Praxair (Product Lot# 70001802562), Cylinder no CC311308, $[\text{NO}] = 500 \text{ ppm}$; Urea, Crystallized from BDH (CAS: 57-13-6); Diamond powder from Lands Superabrasives ($6 \mu\text{m}$, LST600T). The surface of the

diamond powder was cleaned by several cycles of washing with ethanol/water mixtures and then water in a suction filtration system followed by drying in an oven.

5.4.2 DRIFTS experiments

The surface of the diamond powder was cleaned several times with ethanol and water mixtures (50/50%, v/v%) and finally with water using suction filtration. The cleaned diamond powder was oven dried overnight. DRIFTS spectra were collected using a praying mantis diffuse reflectance accessory (Harrick, DRK-4N18) with a stainless-steel high temperature reaction chamber treated with a special SilcoSteelCR coating (HVC, cup 6 by 3 mm, dome cover with two Ge windows and one quartz viewing window).

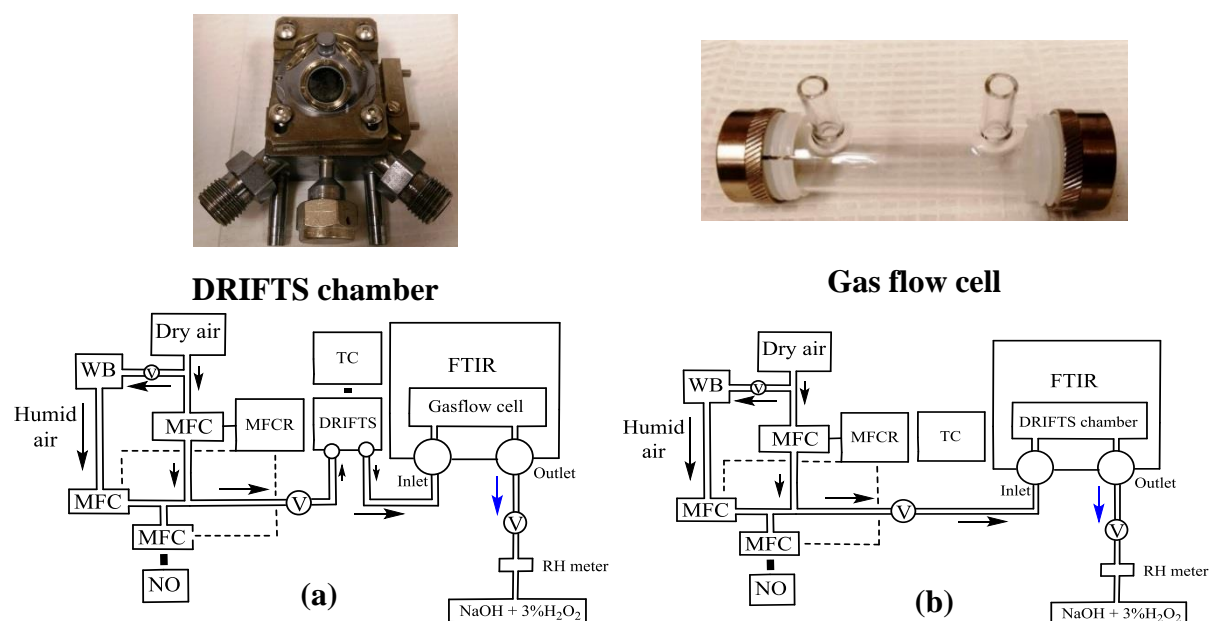


Figure 5.4 Experimental setup for DRIFTS experiments. a) for surface species characterization b) for gas phase species characterization.

A total mass of 0.23 g filled the sample cup of the HVC reaction chamber. The gas handling system described in Figure 5.4 was used to introduce NO vapor and humid air into the reaction chamber using carrier air from a purge gas generator (Paker/Balston Analytical Gas Systems Purge Gas Generator 75-52, less 1 ppm CO₂ and H₂O). The maximum air flow in these experiments after mixing was around 202 standard cubic centimeters per minute (scm). The

DRIFTS accessory was installed into a Nicolet 8700 FTIR spectrometer (Thermo Instruments) equipped with a purge gas generator and a liquid N₂ cooled MCT detector. Each experiment started by preparing a fresh sample containing 8% (wt/wt) urea in Fe-BTC, CoFe₂O₄ or diamond powder. Mechanical mixing of these chemicals was achieved using a wig-L-bug (no ball) for 1 min or manually until the sample became completely homogeneous. Efficient and reproducible packing of the sample was obtained using a 4 kg weight for 10 min. For DRIFTS experiments conducted under dry conditions, the sample was prepared and kept under dry air flow (350 MFC) at 115 °C for about 12 h prior to flowing NO_(g). A single beam spectrum was first collected, and then NO_(g) was introduced. All spectra up to this point were collected by averaging 100 scans at 8 cm⁻¹ resolution. The relative humidity (RH) of the air was measured by a humidity sensor (Vaisala HUMICAP HM70, ±2% RH uncertainty) located at the exit of the DRIFTS reaction chamber.

5.5 Results and discussion

In order to clearly understand and facilitate the analysis for the reactions between $\text{NO}_{(\text{g})}$ and Fe-BTC/8%urea or CoFe_2O_4 /8%urea under dry conditions, several supplementary experiments were performed. The following sections will describe those experiments followed by the NH_3 -SCR of $\text{NO}_{(\text{g})}$ Fe-BTC/8%urea or CoFe_2O_4 /8%urea.

5.5.1 *In situ* production of ammonia (NH_3) from urea (NH_2CONH_2)

In NH_3 -SCR of $\text{NO}_{(\text{g})}$ with Fe-BTC/8%urea or CoFe_2O_4 /8%urea, $\text{NH}_{3(\text{g})}$ will be acting as the reducing agent. In these experiments, urea is the source of $\text{NH}_{3(\text{g})}$. The use of urea for $\text{NH}_{3(\text{g})}$ production is very common. Earlier, aqueous or anhydrous ammonia had mostly been used as a reducing agent for SCR. However, ammonia is a hazardous chemical. Therefore, transportation, storage and handling of $\text{NH}_{3(\text{aq})}$ required high level of safety and environmental regulation. On the other hand, urea is non-toxic, safe and easy to carry. In order to examine the gaseous species upon heating of urea, gas phase experiments were carried out.²⁵ The thermal decomposition of urea was performed and the gas phase products were characterized under dry and humid conditions. Figure 5.5 shows absorbance spectra of control experiment of 8%urea mixed with diamond powder (wt/wt) (used to enhance scattering efficiency of the samples) under dry and humid conditions. All the spectra were referenced to the spectrum obtained after overnight flow of dry air over the sample. After a 20 min flow of dry (Figure 5.5a) and humid air (Figure 5.5b) at 115 °C, there was no evidence of gas phase species. As the melting point of urea is 133 °C, no gas phase product was observed below the melting point. However, when the temperature increased to 180 °C, four strong bands at 3525, 2350, 2269 and 950 cm^{-1} and three relatively weaker bands at 3334 and 1625 cm^{-1} were observed. In the N-H stretching region, the band at 3525 cm^{-1} can be assigned to HNCO (overlapped with gas phase water under humid conditions, Figure 5.5b) while the weak band at 3334 cm^{-1} can be assigned to

NH_3 . The bands at 2350 and 2269 cm^{-1} are due to C=O asymmetric stretching of CO_2 and HNCO , respectively.

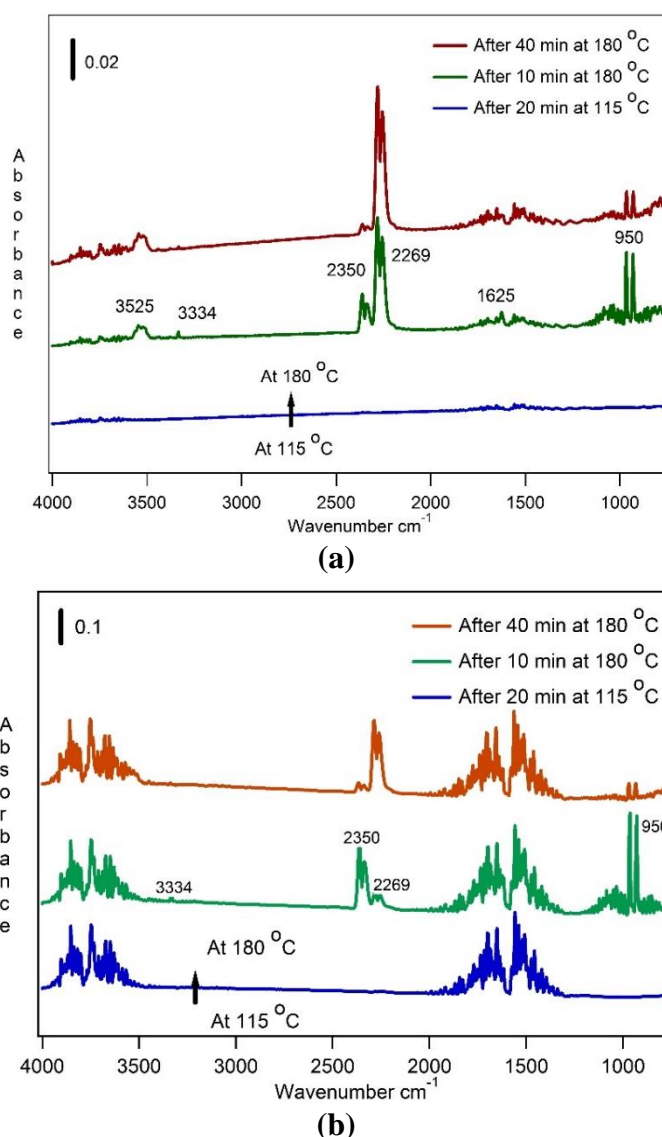


Figure 5.5 Thermal decomposition of urea only under dry and humid conditions (a) Gas phase spectra as a function of time (t) 8% urea/diamond, dry air, at 115 °C, then with heating to 180 °C. (b) Gas phase spectra as function of time (t) 8% urea/diamond, humid air (%RH 10-12), at 115 °C, then with heating to 180 °C.

The band at 1625 cm^{-1} is due to the bending vibration of NH_3 while the band at 950 cm^{-1} is due to the umbrella mode of NH_3 .²⁶ The amount of gas phase product produced was quantified by using the molar absorptivity values from the Table 6.1 in Appendix 3. The kinetic curve was obtained by plotting the change in concentration for the gases with time for each experiment.

Figure 5.6 shows kinetic curves for both NH_3 and HNCO as a function of time for data in Figure 5.5a,b.

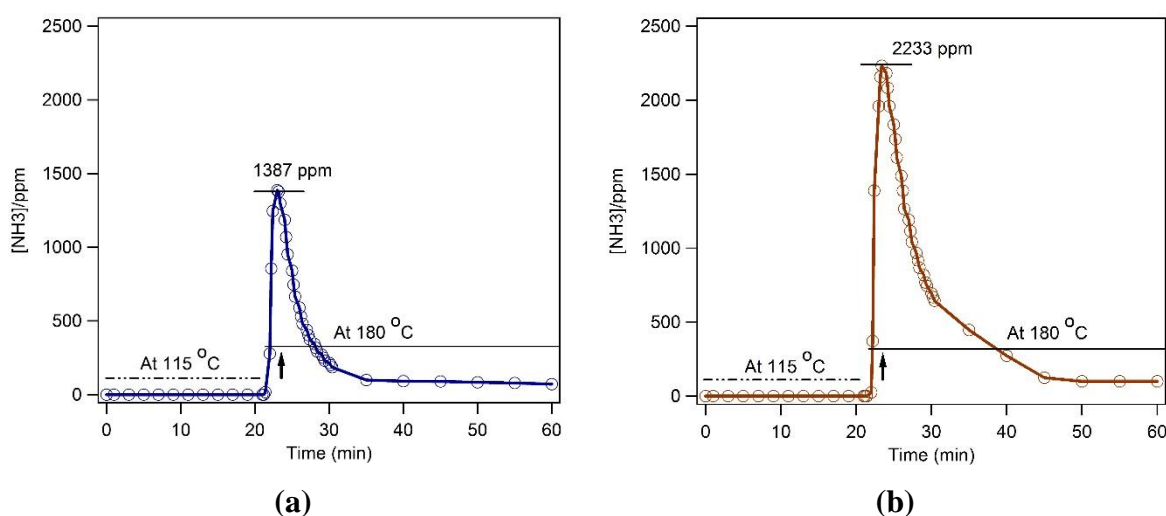
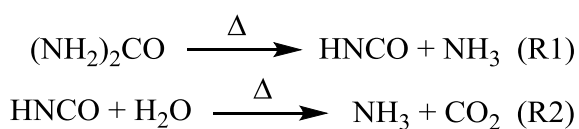


Figure 5.6(a) Kinetic curve of $[\text{NH}_3]$ vs time for data in figure 5.5(a). **(b)** Kinetic curve of $[\text{NH}_3]$ vs time (min) for data in Figure 5.5(b).

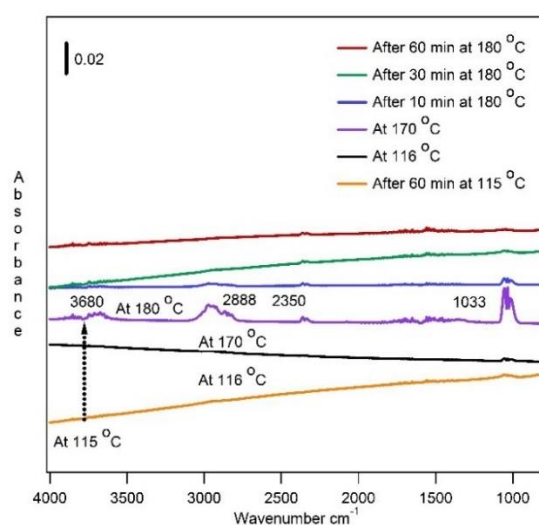
The data implies that under both dry and humid condition, the production of NH_3 is fast, within 10 min, and hardly observed with the span of time by 60 min. The kinetic data shows the effect of humidity on the production of NH_3 . The amount of $\text{NH}_{3(\text{g})}$ produced under humid condition (2233 ppm) is 1.6 times greater than the dry condition (1387 ppm). Reactions on the thermal decomposition of urea are given below. Urea firstly decomposes into equimolar products of $\text{NH}_{3(\text{g})}$ and $\text{HNCO}_{(\text{g})}$ (R1). However, water vapor existing in the system may further react with $\text{HNCO}_{(\text{g})}$ to form additional $\text{NH}_{3(\text{g})}$ and $\text{CO}_{2(\text{g})}$ via hydrolysis according to the following reaction (R2).²⁵



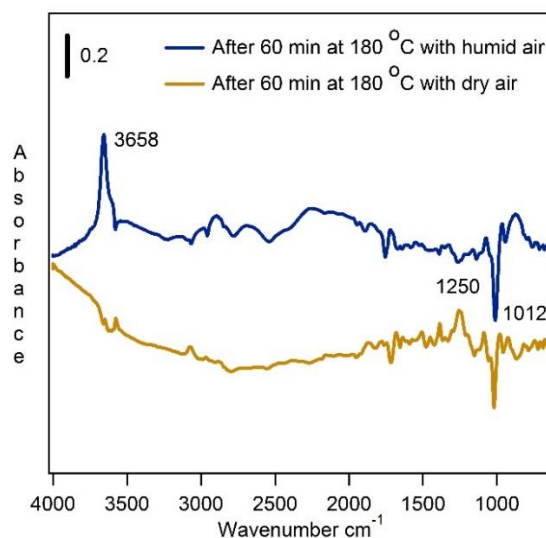
Under dry condition R1 is a standard reaction that occurs. However, R2 dominates under humid conditions.

5.5.2 Thermal decomposition of Fe-BTC under dry conditions

Fe-BTC has been known as a stable MOF at higher temperature and possesses good thermal stability.²⁷ In order to examine the stability as well as to characterize the gas phase products obtained from the thermal decomposition under dry conditions, Fe-BTC only was heated to 115 °C and then 180 °C for 60 min at each temperature. Figure 5.7 shows the absorbance spectra for both gas and surface species from the thermal decomposition of Fe-BTC.



(a)



(b)

Figure 5.7 Thermal decomposition of Fe-BTC only under dry conditions (a) Gas phase spectra as a function of time and temperature, dry condition. (b) DRIFTS spectra of Fe-BTC only as a function of time and temperature-dry (brown) and humid (blue) conditions.

There was no evidence of gas phase product at 115 °C. However, when the temperature was increased to 170 °C, there is evidence of production of gas phase CH₃OH. Figure 5.7a shows the gas phase absorbance spectra with peaks at 3680, 2888 and 1033 cm⁻¹ which have been assigned to ν (-OH), ν (-CH) and ν (C-O) functional groups of CH₃OH, respectively. The production of CH₃OH was very fast and almost disappeared after 60 min at 180 °C. Figure 5.7b shows the DRIFTS absorption spectra as a function of time and temperature. All the spectra were referenced to the spectrum obtained after overnight flow of dry air over the sample. The experiments were designed to thermally-treat the solid materials Fe-BTC at 180 °C under a flow of dry and humid air and observe the changes on the surface species after heating. There was a negative at 1250 cm⁻¹ and a peak appeared at 3658 cm⁻¹ after heating Fe-BTC at 180 °C for 60 min under humid air. The negative feature assigned to ν (-CH₂) while another negative feature at 1012 cm⁻¹ (appeared in both dry and humid conditions) might be due to ν (C-O). Peak at 3658 cm⁻¹ is due to the adsorbed -OH on the surface. However, the data reveals that Fe-BTC is a stable material at these temperatures under both dry and humid conditions.

5.5.3 Thermal decomposition of Fe-BTC/8%urea mixture under dry conditions

Thermal decomposition of Fe-BTC/8%urea mixture under dry condition was performed with a view to investigate the gas phase product obtained without reacting with NO(g). Figure 5.8a shows the gas phase absorbance spectra of thermal decomposition Fe-BTC/8%urea mixture as a function of time and temperature under dry condition.

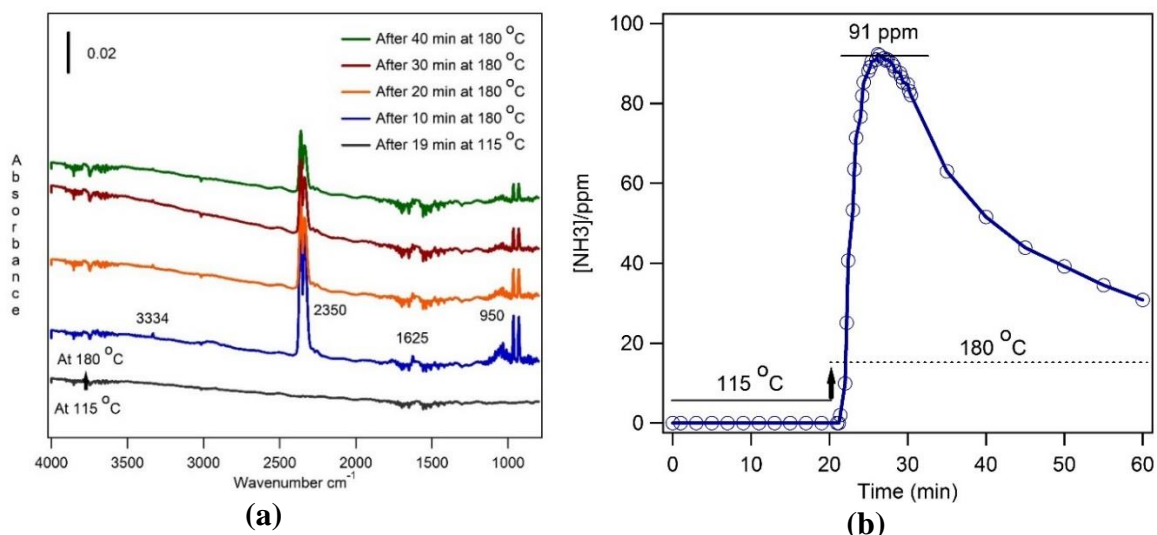


Figure 5.8 Thermal decomposition of Fe-BTC/8%urea mixture under dry conditions and quantification of gas phase products. (a) Gas phase spectra as a function of time (min) and temperature ($^\circ\text{C}$) under dry air. (b) Kinetic curve of $[\text{NH}_3]$ vs time (min) for data in Figure 5.8(a).

At first Fe-BTC/8%urea was heated at 115°C for 19 min. Then, the temperature was increased to 180°C and kept another 40 min. There was no evidence of gas phase product at 115°C . However, when the temperature increased to 180°C , the amount of $\text{NH}_3(\text{g})$ went to the maximum (91 ppm) within 10 min, as evident from the kinetic curve (Figure 5.8b). As the time progressed, the concentration of $\text{NH}_3(\text{g})$ went down. In similar experimental condition, 8%urea mixed with diamond powder produced 1387 ppm $\text{NH}_3(\text{g})$ (Figure 5.6a). The results imply that, Fe-BTC trap $\text{NH}_3(\text{g})$ inside the MOF. Moreover, there is a clear difference between the gas phase product of thermally treated Fe-BTC only and Fe-BTC/8%urea. There was an evidence of gas phase CH_3OH when Fe-BTC only was heated. However, in case of Fe-BTC/8%urea mixture, there is no evidence of gas phase CH_3OH . The reason might be as follows-when Fe-BTC only is heated, CH_3OH is produced from catalytic hydrogenation of $\text{CO}_2(\text{g})$.²⁸ In this hydrogenation reaction, the source of $\text{H}_2(\text{g})$ is the small amount of gas phase water as the reaction is performed under dry condition. However, thermal treatment of Fe-BTC/8%urea mixture produces intermediate product $\text{HNCO}(\text{g})$ from urea as discussed in section 5.4.1 and it reacts with gas phase H_2O to produce more $\text{NH}_3(\text{g})$ and $\text{CO}_2(\text{g})$. Since the source of $\text{H}_2(\text{g})$ is

blocked, in this experiment gas phase CH_3OH production is hindered. Thus, thermal treatment of Fe-BTC/8%urea mixture produces $\text{NH}_3(\text{g})$ (91 ppm) along with $\text{CO}_2(\text{g})$. No evidence of gas phase CH_3OH . However, the amount of NH_3 is nearly 16 time less than the amount (1387 ppm) produced with 8% urea only.

5.5.4 Thermal decomposition of Fe-BTC/8%urea mixture under humid conditions

The Fe-BTC/8%urea mixture was heated similarly as discussed in previous section 5.4.3 under humid conditions. The purpose of this experiment was to understand the effect of humidity on the thermal treatment. Figure 5.9a shows the absorption spectra as a function of time and temperature under humid conditions.

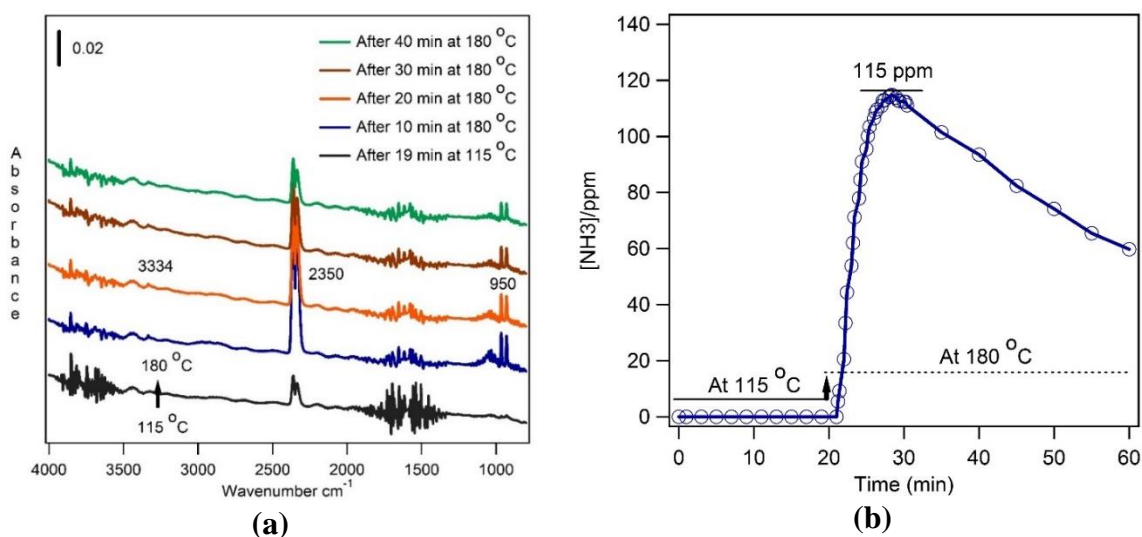


Figure 5.9 Thermal decomposition of Fe-BTC/8%urea mixture under humid conditions and quantification of gas phase products (a) Gas phase spectra as a function of time (min) and temperature ($^{\circ}\text{C}$) under humid conditions, (%RH 10-12). (b) Kinetic curve of $[\text{NH}_3]$ vs time (min) for data in Figure 5.9(a).

At first, Fe-BTC/8%urea was heated at 115 $^{\circ}\text{C}$ for 19 min, (%RH 10-12). Then, the temperature was increased to 180 $^{\circ}\text{C}$. There was no evidence of gas phase product at 115 $^{\circ}\text{C}$. However, when the temperature increased to 180 $^{\circ}\text{C}$, bands appeared at 3334 and 950 cm^{-1} . However, other characteristics peaks (3525 and 1625 cm^{-1}) have been overlapped with gas phase water. The amount of $\text{NH}_3(\text{g})$ went to the maximum (115 ppm) within 10 min, as evident from the

kinetic curve (Figure 5.9b). As the time progress, the concentration of $\text{NH}_3(\text{g})$ went down. In similar experimental conditions, 8%urea mixed with diamond powder produced 2233 ppm $\text{NH}_3(\text{g})$ (Figure 5.6b). It was expected that the humid conditions will enhance the production of $\text{NH}_3(\text{g})$ relative to dry conditions. Since, the presence of gas phase H_2O enhanced the amount of $\text{NH}_3(\text{g})$ with 8%urea only (section 5.4.1). The amount of $\text{NH}_3(\text{g})$ produced is 115 ppm, slightly higher than the dry conditions (91 ppm). The results imply that Fe-BTC trap $\text{NH}_3(\text{g})$ inside the MOF, in both dry and humid conditions.

Earlier sections (5.4.1 to 5.4.4) discussed the experiments associated with the reactions in absence of $\text{NO}(\text{g})$. From the following section the reaction of $\text{NO}(\text{g})$ with Fe-BTC, CoFe_2O_4 and urea will be discussed under different experimental conditions.

5.5.5 Reaction of $\text{NO}(\text{g})$ with either Fe-BTC or 8%urea under dry conditions

Previously, the thermal decomposition of 8%urea (5.4.1) and Fe-BTC only (5.4.2) have been discussed and the gas phase products have been characterized. In order to study the change in the gas phase products upon addition of $\text{NO}(\text{g})$, the reaction of $\text{NO}(\text{g})$ with Fe-BTC only or 8%urea were performed under dry conditions. In these experiments, $\text{NH}_3(\text{g})$ was produced from the decomposition of urea to act as reducing agent for the reduction of $\text{NO}(\text{g})$. These controlled experiments were performed in order to compare the results obtained from the actual experiment. Figure 5.10 shows the gas phase absorption spectra of the reaction of $\text{NO}(\text{g})$ with either Fe-BTC (5.10a) or 8% urea (5.10c) under dry conditions along with the kinetic curve for selected gases $\text{NO}(\text{g})$, $\text{NH}_3(\text{g})$ and $\text{HNCO}(\text{g})$ as a function of time and temperature. For the reaction between $\text{NO}(\text{g})$ with Fe-BTC only under dry conditions, the sample was heated for 19 min at 115 °C. Then, the temperature was increased to 180 °C and kept for 20 min. Since these experiments were conducted under excess NO , the gas phase species detected were NO (1875 cm^{-1}) and NO_2 (1627 cm^{-1}) from wall reactions along²⁹ with CO_2 (2350 cm^{-1}). In addition, there

was an evidence of gas phase CH_3OH ($\nu(\text{C-H})$ 2888 and $\nu(\text{C-O})$ 1033 cm^{-1}) when the temperature is increased to 180 °C.

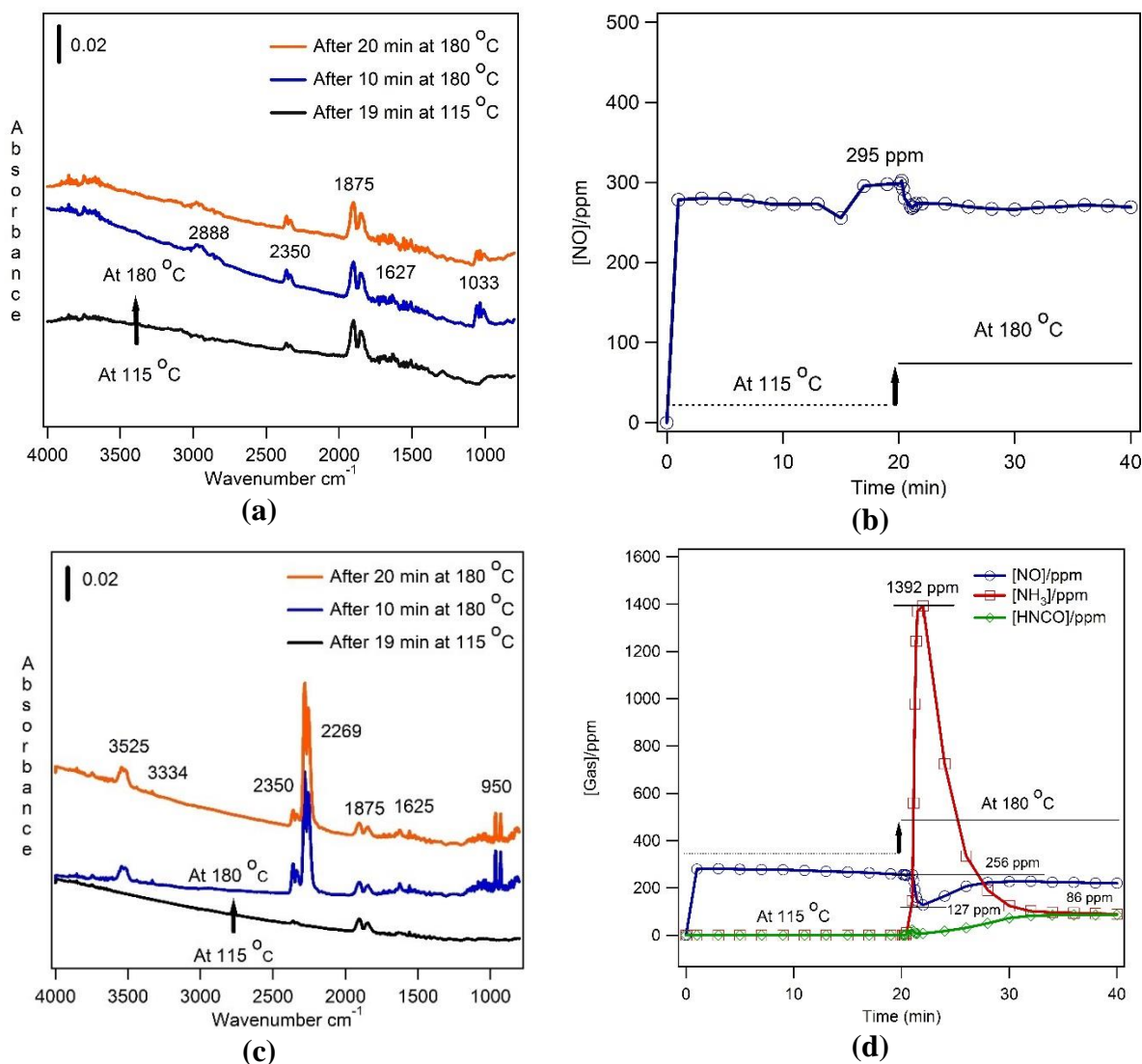


Figure 5.10 Reaction of NO with either Fe-BTC or 8% urea under dry conditions. (a) Gas phase spectra of reaction between NO and Fe-BTC only as a function of time (min) and temperature (°C) under dry air. (b) Kinetic curve of [NO] vs time (min) for data in figure 5.10(a). (c) Gas phase spectra of reaction between NO and diamond/8% urea as a function of time (min) and temperature (°C) under dry conditions. (d) Kinetic curve of [NO]/[NH₃]/[HNCO] vs time (min) for data in Figure 5.10(c).

Figure 5.10b shows kinetic curve of $\text{NO}_{(\text{g})}$ in a control gas phase experiment of Fe-BTC with $\text{NO}_{(\text{g})}$. The data show that there was no significant change in the concentration of $\text{NO}_{(\text{g})}$ throughout the reaction time. The concentration of $\text{NO}_{(\text{g})}$ was steady even as the temperature increased to 180 °C from 115 °C. The maximum concentration of $\text{NO}_{(\text{g})}$ was 295 ppm.

Reaction of $\text{NO}_{(g)}$ with 8%urea was performed under dry conditions. Figure 5.10c shows the absorbance spectra of the reaction between $\text{NO}_{(g)}$ and 8%urea mixed with diamond powder under dry conditions. At first, the sample was heated for 19 min at 115 °C. Then, the temperature was increased to 180 °C and kept for 20 min. There was no evidence of gas phase product at 115 °C. At 180 °C, the gas phase species detected were $\text{NH}_{3(g)}$ (3525, 3334, 1625 and 950 cm^{-1}), $\text{HNCO}_{(g)}$ (2269 cm^{-1}), and reactant $\text{NO}_{(g)}$ (1875 cm^{-1}) along with $\text{CO}_{2(g)}$ (2350 cm^{-1}). The kinetic curves for $\text{NH}_{3(g)}$, $\text{HNCO}_{(g)}$ and $\text{NO}_{(g)}$ as a function of time, are represented in Figure 5.10d. The data showed that when 8%urea react with $\text{NO}_{(g)}$ under dry conditions at 180 °C, the change in concentration for $\text{NO}_{(g)}$ was significant, 256 ppm to 127 ppm. The maximum amount of $\text{NH}_{3(g)}$ produced is 1392 ppm. While 86 ppm of $\text{HNCO}_{(g)}$ was produced from the reaction. Thus, the data revealed that reaction of $\text{NO}_{(g)}$ with Fe-BTC only under dry conditions shows similar types of products that were obtain in the absence of $\text{NO}_{(g)}$ (section 5.4.2). As the concentration of $\text{NO}_{(g)}$ remains the same throughout the total experimental time and does not change even after the increase of temperature, implies that no reaction takes place between $\text{NO}_{(g)}$ and Fe-BTC only. The slight dip in the concentration observed in the kinetic curve (5.10b) might be due to adsorption of $\text{NO}_{(g)}$ onto surface after increasing temperature for opening of surface sites. On the other hand, 8%urea produce $\text{NH}_{3(g)}$ (1392 ppm) that reduced $\text{NO}_{(g)}$, as evident from the kinetic curve (Figure 5.10 d). The concentration of $\text{NO}_{(g)}$ was steady (256 ppm) at 115 °C. However, when the temperature was increased, $\text{NH}_{3(g)}$ was produced and upon reduction the concentration of $\text{NO}_{(g)}$ went to 127 ppm, revealed that reduction of $\text{NO}_{(g)}$ takes place.

5.5.6 Reaction of $\text{NO}_{(g)}$ with Fe-BTC/8%urea mixture under dry conditions

In order to examine the catalytic performance of Fe-BTC/8%urea mixture in NH_3 -SCR of $\text{NO}_{(g)}$, reaction of $\text{NO}_{(g)}$ with Fe-BTC/8%urea mixture was carried out under dry conditions. Figure 5.11a shows the absorbance spectra of the reaction between $\text{NO}_{(g)}$ and Fe-BTC/8%urea under dry conditions.

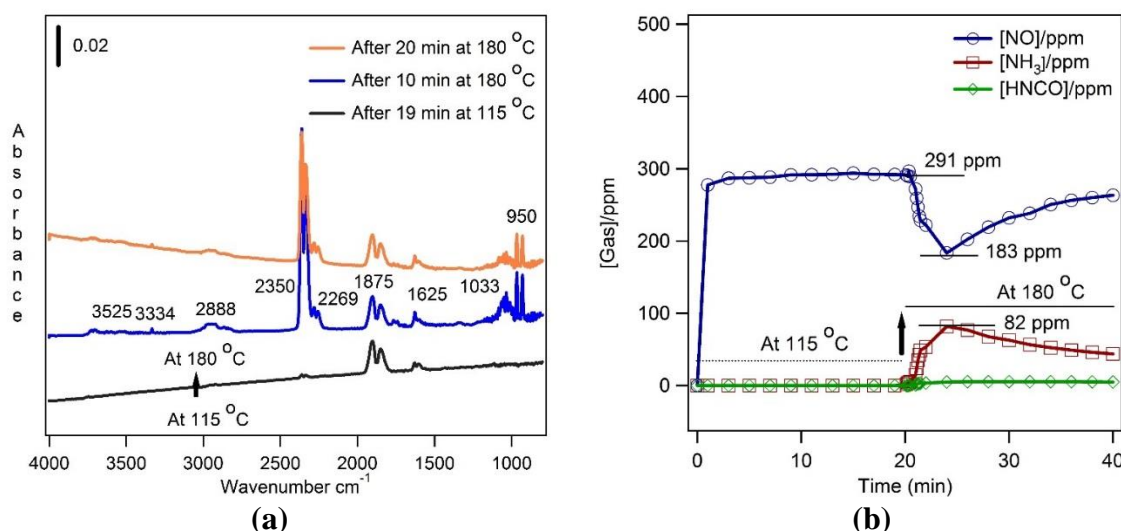


Figure 5.11 Reaction of NO with Fe-BTC/8%urea mixture under dry conditions. (a) Gas phase spectra of reaction between NO and Fe-BTC/8%urea as a function of time (min) and temperature ($^{\circ}\text{C}$) under dry air. (b) Kinetic curve of $[\text{NO}]/[\text{NH}_3]/[\text{HNCO}]$ vs time (min) for data in Figure 5.11(a).

The Fe-BTC/8%urea mixture was under dry air flow overnight at 115°C . The purpose of this step was to remove loosely bonded species from the surface and/or pores of the active materials, particularly water and volatile organic compounds. This temperature was below the melting point of urea at 133°C . Then, a dry flow of $\text{NO}_{(g)}$ was introduced. All the spectra were referenced to the spectrum obtained after overnight flow of dry air over the sample at 115°C . No evidence of gas phase product appeared at 115°C . When the temperature was increased to 180°C , several peaks appeared. The gas phase species detected are $\text{NH}_{3(g)}$, $\text{HNCO}_{(g)}$, $\text{CO}_{2(g)}$ along with gas phase CH_3OH . These species have been characterized in previous sections. Figure 5.11b shows the kinetic curves for $\text{NO}_{(g)}$, $\text{NH}_{3(g)}$ and $\text{HNCO}_{(g)}$ as a function of time and temperature. The kinetic data showed that there was a change in the concentration of $\text{NO}_{(g)}$

from 291 ppm to 183 ppm, as the temperature increased from 115 °C to 180 °C. The change in concentration of $\text{NO}_{(\text{g})}$ is reasonable as at this temperature, $\text{NH}_{3(\text{g})}$ is produced and reacts to reduce $\text{NO}_{(\text{g})}$. However, the concentration of $\text{HNCO}_{(\text{g})}$ is negligible. In the absence of $\text{NO}_{(\text{g})}$, the concentration of $\text{NH}_{3(\text{g})}$ went up to 91 ppm (Figure 5.8b) at 180 °C, whereas the maximum concentration of $\text{NH}_{3(\text{g})}$ is 82 ppm implies that $\text{NH}_{3(\text{g})}$ participates to reduce $\text{NO}_{(\text{g})}$.

5.5.7 Reaction of $\text{NO}_{(\text{g})}$ with Fe-BTC/8%urea mixture under humid conditions

In order to study the effect of humidity on NH_3 -SCR of $\text{NO}_{(\text{g})}$ in presence of Fe-BTC/8%urea, reaction of $\text{NO}_{(\text{g})}$ with Fe-BTC/8%urea mixture was carried out under humid conditions. Figure 5.12a shows the absorbance spectra of the reaction between $\text{NO}_{(\text{g})}$ and Fe-BTC/8%urea under humid conditions (%RH 10-12).

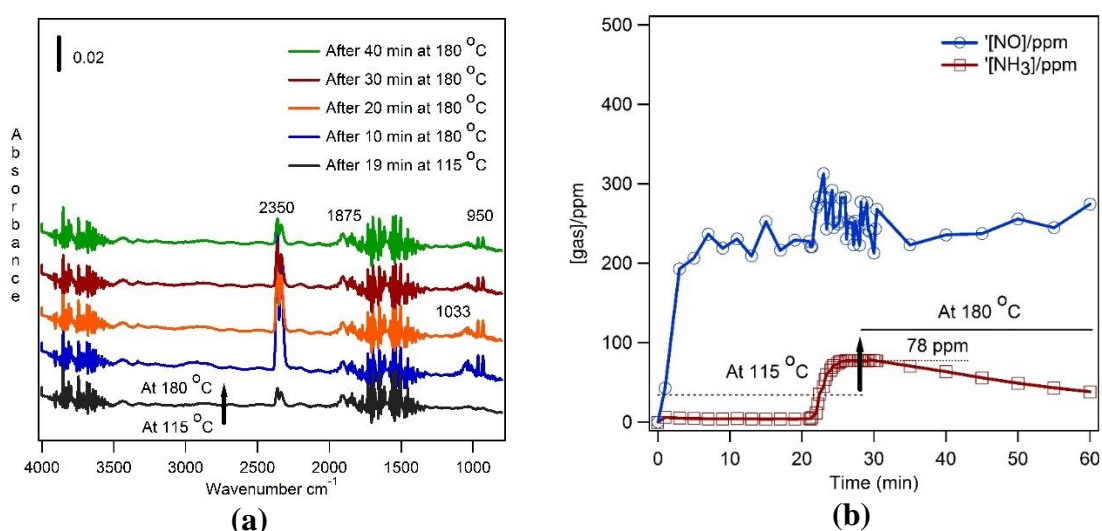


Figure 5.12 Reaction of NO with Fe-BTC/8%urea mixture under humid conditions. (a) Gas phase spectra of reaction between NO and FeBTC/8%urea as a function of time (min) and temperature (°C) under humid conditions (%RH 10-12). (b) Kinetic curve of $[\text{NO}]/[\text{NH}_3]$ vs time (min) for data in Figure 5.12(a).

All the spectra were referenced to the spectrum obtained after overnight flow of dry air over the sample at 115 °C. No gas phase product appeared at 115 °C. When the temperature was increased to 180 °C, peaks appeared. The gas phase species detected are $\text{NH}_{3(\text{g})}$ (950 cm^{-1}) and $\text{CO}_{2(\text{g})}$ (2350 cm^{-1}) along with gas phase CH_3OH (1033 cm^{-1}). Due to the presence of gas phase water, all the peaks did not appear for the gas phase species detected under dry conditions.

These species have been characterized in previous sections. Figure 5.12d shows the kinetic curve for $\text{NO}_{(\text{g})}$ and $\text{NH}_{3(\text{g})}$. The trend of $\text{NO}_{(\text{g})}$ concentration fluctuated due to the presence of gas phase water. However, the average concentration of $\text{NO}_{(\text{g})}$ was around 250 ppm. The maximum amount of $\text{NH}_{3(\text{g})}$ product is 78 ppm, less than the amount obtained from the dry conditions at 180 °C. On the other hand, comparison with the experiment of Fe-BTC/8%urea in the absence of $\text{NO}_{(\text{g})}$ (Figure 5.9b), shows that the concentration of $\text{NH}_{3(\text{g})}$ is higher (115 ppm) than in presence of $\text{NO}_{(\text{g})}$ under humid conditions at 180 °C. However, the kinetic data reveals that reduction of $\text{NO}_{(\text{g})}$ did not take place under humid conditions.

5.5.8 Reaction of $\text{NO}_{(\text{g})}$ with CoFe_2O_4 under dry conditions

Reaction of $\text{NO}_{(\text{g})}$ with CoFe_2O_4 nanoparticles were investigated in order to compare the results obtained from the reaction of $\text{NO}_{(\text{g})}$ and Fe-BTC. Figure 5.13a show the absorbance spectra of the reaction between $\text{NO}_{(\text{g})}$ and CoFe_2O_4 as a function of time and temperature.

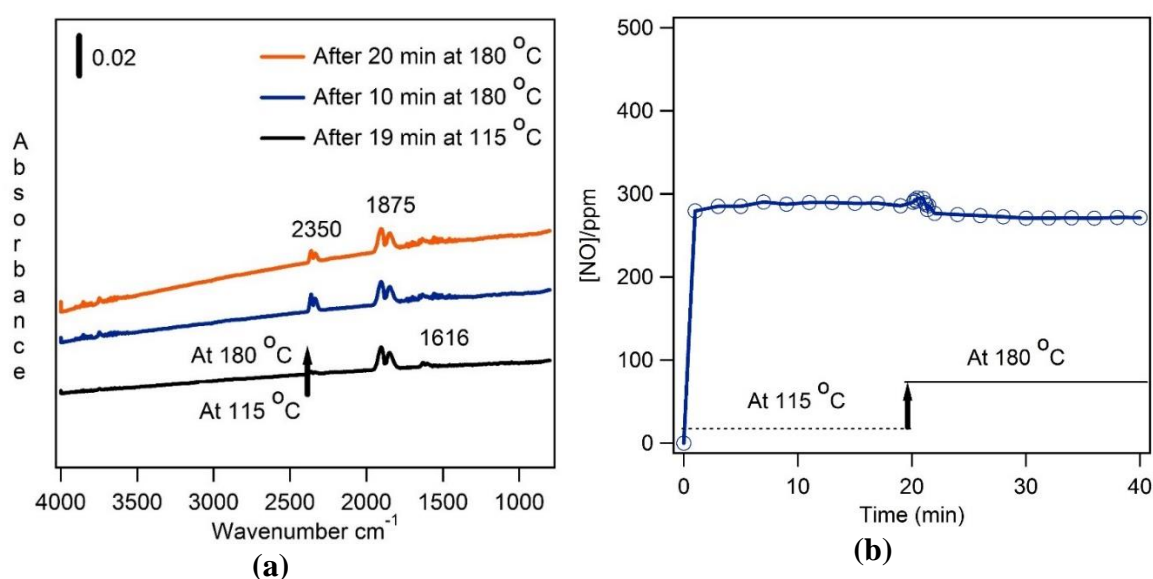


Figure 5.13 (a) Gas phase spectra of reaction between NO and CoFe_2O_4 only as a function of time (min) and temperature (°C) under dry air. (b) Kinetic curve of $[\text{NO}]$ vs time (min) for data in Figure 5.13(a).

At 115 °C, the spectrum shows peak at 1875 and 1616 cm^{-1} due to the $\text{NO}_{(\text{g})}$ and $\text{NO}_{2(\text{g})}$, respectively. However, when the temperature is increased to 180 °C, $\text{CO}_{2(\text{g})}$ show up at 2350 cm^{-1} . Figure 5.13b shows the kinetic curve for $\text{NO}_{(\text{g})}$ as a function of time and temperature. The

concentration of $\text{NO}_{(g)}$ remains almost steady, throughout the reaction time, even at higher temperature. The amount of $\text{NO}_{(g)}$ is around 290 ppm. The data showed that $\text{NO}_{(g)}$ do not react with CoFe_2O_4 , similar to the data obtained for the reaction with Fe-BTC. However, there is no evidence of gas phase CH_3OH as observed in the reaction of Fe-BTC only at high temperature.

5.5.9 Reaction of $\text{NO}_{(g)}$ with $\text{CoFe}_2\text{O}_4/8\%$ urea mixture under dry conditions

In order to compare the results obtained from the reaction of $\text{NO}_{(g)}$ with Fe-BTC/8%urea, reactions of $\text{NO}_{(g)}$ with $\text{CoFe}_2\text{O}_4/8\%$ urea nanoparticles mixer were carried out under dry conditions. Figure 5.14a shows the absorbance spectra of the reaction between $\text{NO}_{(g)}$ and $\text{CoFe}_2\text{O}_4/8\%$ urea nanoparticles under dry conditions.

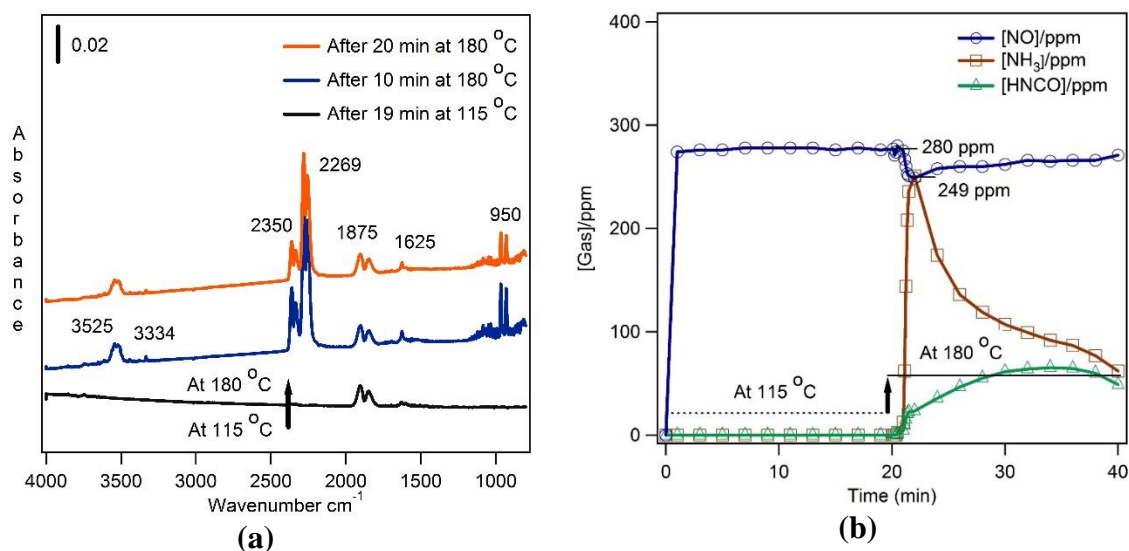


Figure 5.14 (a) Gas phase spectra of reaction between NO and $\text{FeCoO}_x/8\%$ urea as a function of time (min) and temperature ($^{\circ}\text{C}$) under dry air. (b) Kinetic curve of $[\text{NO}]/[\text{NH}_3]/[\text{HNCO}]$ vs time (min) for data in Figure 5.14(a).

The gas phase species detected are $\text{NH}_3_{(g)}$, $\text{HNCO}_{(g)}$ along with $\text{CO}_2_{(g)}$ at 180°C . Figure 5.14b shows the kinetic curves for $\text{NH}_3_{(g)}$, $\text{NO}_{(g)}$ and $\text{HNCO}_{(g)}$ for the gas phase experiment of 8%urea/Fe-Co with $\text{NO}_{(g)}$ under dry conditions. The temperature was kept at 115°C for first 19 min and then increased to 180°C for next 20 min. The initial concentration of $\text{NO}_{(g)}$ was found 280 ppm. However, when the temperature was increased to 180°C , the concentration of $\text{NO}_{(g)}$ went down to 249 and $\text{NH}_3_{(g)}$ concentration was around 250 ppm. Also, maximum 65

ppm isocyanic acid $\text{HNCO}_{(g)}$ was observed. It was found that only 10% of $\text{NO}_{(g)}$ reacted in the presence of $\text{CoFe}_2\text{O}_4/8\%$ urea. However, in case of $\text{Fe-BTC}/8\%$ urea, 37% $\text{NO}_{(g)}$ reacted. Figure 5.15 shows the proposed mechanism for the reaction of $\text{NO}_{(g)}$ with $\text{Fe-BTC}/8\%$ urea and $\text{CoFe}_2\text{O}_4/8\%$ urea under dry conditions based on the data obtained from the gas phase experiments.

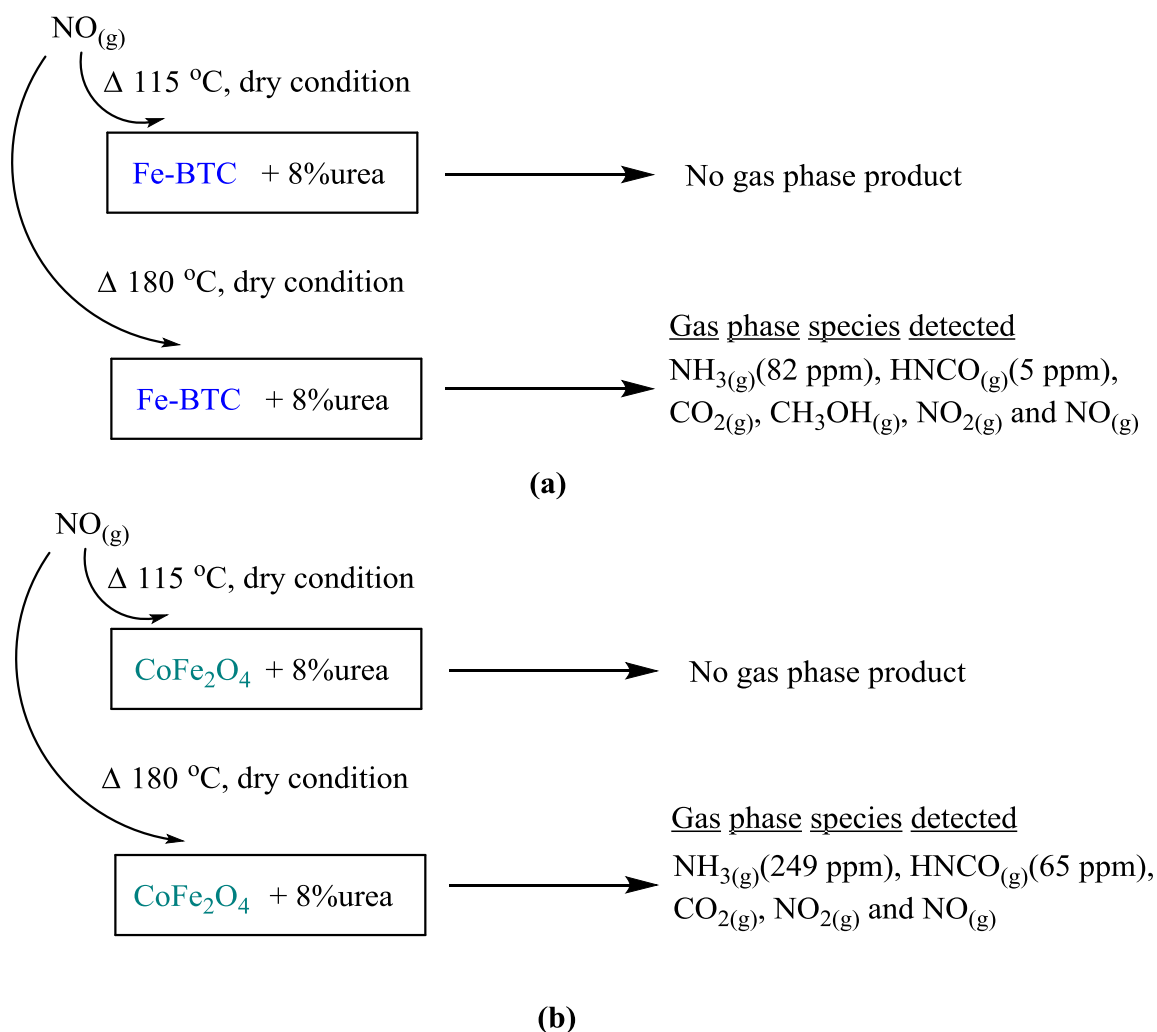


Figure 5.15 Summary diagram for the reaction of $\text{NO}_{(g)}$ with (a) $\text{Fe-BTC}/8\%$ urea and (b) $\text{CoFe}_2\text{O}_4/8\%$ urea under dry conditions.

In both $\text{Fe-BTC}/8\%$ urea and $\text{CoFe}_2\text{O}_4/8\%$ urea, no gas phase product is observed at 115 °C. However, when the temperature is increased to 180 °C, gas phase species such as $\text{NH}_3_{(g)}$,

$\text{HNCO}_{(g)}$, $\text{CO}_{2(g)}$, $\text{NO}_{2(g)}$ and $\text{NO}_{(g)}$ was detected. In addition, gas phase CH_3OH was observed in case Fe-BTC/8%urea due to catalytic hydrogenation of $\text{CO}_{2(g)}$.

5.6 Conclusion

In summary the presence of urea appears to change the type of surface functional groups on Fe-BTC and CoFe_2O_4 . The reaction of $\text{NO}_{(g)}$ with Fe-BTC/8%urea and CoFe_2O_4 /8%urea end up producing gas phase products such as NH_3 , HNCO and CO_2 . In addition, gas phase CH_3OH is observed from catalytic hydrogenation in presence of Fe-BTC. The data reveals that 8%urea with diamond mixed produced the maximum amount of $\text{NH}_{3(g)}$ 1392 ppm under dry conditions. This amount increased to 2233 ppm in the present of humid air. However, in the case of 8%urea mixed with Fe-BTC and CoFe_2O_4 , the results were completely different. Humid conditions did not favor the production of $\text{NH}_{3(g)}$ as demonstrated by the data analysis. However, CoFe_2O_4 nanoparticle showed better performance compared to Fe-BTC MOFs, considering the rate of conversion of $\text{NO}_{(g)}$, which are $2.3 \pm 0.03 \text{ ppm} \cdot \text{m}^{-2} \cdot \text{min}^{-1}$ and $0.22 \pm 0.04 \text{ ppm} \cdot \text{m}^{-2} \cdot \text{min}^{-1}$, respectively. This is expected, since the conversion rate depends on the concentration of the $\text{NH}_{3(g)}$ produced during the reaction. The data reveals that $\text{NH}_{3(g)}$ produced from the decomposition of Fe-BTC/8%urea is trapped into the pores of Fe-BTC MOFs, results in a lower concentration of $\text{NH}_{3(g)}$ in the system. In contrast, decomposition of CoFe_2O_4 /8%urea releases more $\text{NH}_{3(g)}$, increasing the conversion of $\text{NO}_{(g)}$.

5.7 References

- (1) Xu, J.; Chen, G.; Guo, F.; Xie, J. Development of Wide-Temperature Vanadium-Based Catalysts for Selective Catalytic Reducing of NO_x with Ammonia: Review. *Chem. Eng. J.* **2018**, *353*, 507–518.
- (2) Roy, S.; Hegde, M. S.; Madras, G. Catalysis for NO_x Abatement. *Appl. Energy* **2009**, *86* (11), 2283–2297.

- (3) Ma, L.; Cheng, Y.; Cavataio, G.; McCabe, R. W.; Fu, L.; Li, J. *In Situ* DRIFTS and Temperature-Programmed Technology Study on NH₃-SCR of NO_x over Cu-SSZ-13 and Cu-SAPO-34 Catalysts. *Appl. Catal. B Environ.* **2014**, *156–157*, 428–437.
- (4) Cheng, X.; Bi, X. T. A Review of Recent Advances in Selective Catalytic NO_x Reduction Reactor Technologies. *Particuology* **2014**, *16*, 1–18.
- (5) Lu, P.; Li, R.; Xing, Y.; Li, Y.; Zhu, T.; Yue, H.; Wu, W. Low Temperature Selective Catalytic Reduction of NO_x with NH₃ by Activated Coke Loaded with Fe x Coy CezO_M: The Enhanced Activity, Mechanism and Kinetics. *Fuel* **2018**, *233* (January), 188–199.
- (6) Gao, F.; Tang, X.; Yi, H.; Zhao, S.; Li, C.; Li, J.; Shi, Y.; Meng, X. A Review on Selective Catalytic Reduction of NO_x by NH₃ over Mn-Based Catalysts at Low Temperatures: Catalysts, Mechanisms, Kinetics and DFT Calculations; **2017**; Vol. 7.
- (7) Zhou, H.-C. “Joe”; Kitagawa, S. Metal–Organic Frameworks (MOFs). *Chem. Soc. Rev.* **2014**, *43* (16), 5415–5418.
- (8) Furukawa, H.; Ko, N.; Go, Y. B.; Aratani, N.; Choi, S. B.; Choi, E.; Yazaydin, a O.; Snurr, R. Q.; O’Keeffe, M.; Kim, J.; et al. Ultrahigh Porosity in Meta-Organic Frameworks. *Science*. **2010**, *329* (5990), 424.
- (9) Czaja, A. U.; Trukhan, N.; Müller, U. Industrial Applications of Metal–Organic Frameworks. *Chem. Soc. Rev.* **2009**, *38* (5), 1284.
- (10) Wang, Q.; Luo, J.; Zhong, Z.; Borgna, A. CO₂ Capture by Solid Adsorbents and Their Applications: Current Status and New Trends. *Energy Environ. Sci.* **2011**, *4* (1), 42–55.
- (11) Chaemchuen, S.; Kabir, N. A.; Zhou, K.; Verpoort, F. Metal–Organic Frameworks for Upgrading Biogas via CO₂ Adsorption to Biogas Green Energy. *Chem. Soc. Rev.* **2013**,

- 42 (24), 9304.
- (12) Furukawa, H.; Cordova, K. E.; O’Keeffe, M.; Yaghi, O. M. The Chemistry and Applications of Metal-Organic Frameworks. *Science*. **2013**, *341* (6149).
- (13) Zou, L.; Zhou, H. C. Hydrogen Storage in Metal-Organic Frameworks. *Nanostructured Mater. Next-Generation Energy Storage Convers. Hydrog. Prod. Storage, Util.* **2017**, 143–170.
- (14) Sumida, K.; Rogow, D. L.; Mason, J. A.; McDonald, T. M.; Bloch, E. D.; Herm, Z. R.; Bae, T.-H.; Long, J. R. Carbon Dioxide Capture in Metal–Organic Frameworks. *Chem. Rev.* **2012**, *112* (2), 724–781.
- (15) Huang, C. Y.; Song, M.; Gu, Z. Y.; Wang, H. F.; Yan, X. P. Probing the Adsorption Characteristic of Metal-Organic Framework MIL-101 for Volatile Organic Compounds by Quartz Crystal Microbalance. *Environ. Sci. Technol.* **2011**, *45* (10), 4490–4496.
- (16) Dutta, A.; Wong-Foy, A. G.; Matzger, A. J. Coordination Copolymerization of Three Carboxylate Linkers into a Pillared Layer Framework. *Chem. Sci.* **2014**, *5* (10), 3729–3734.
- (17) Li, J. R.; Kuppler, R. J.; Zhou, H. C. Selective Gas Adsorption and Separation in Metal-Organic Frameworks. *Chem. Soc. Rev.* **2009**, *38* (5), 1477–1504.
- (18) Zhao, X.; Wang, Y.; Li, D. S.; Bu, X.; Feng, P. Metal–Organic Frameworks for Separation. *Adv. Mater.* **2018**, *30* (37), 869–932.
- (19) Youn, H. K.; Kim, J.; Ahn, W. S. MWCNT Synthesis over Fe-BTC as a Catalyst/Carbon Source via CVD. *Mater. Lett.* **2011**, *65* (19–20), 3055–3057.
- (20) Dhakshinamoorthy, A.; Alvaro, M.; Horcajada, P.; Gibson, E.; Vishnuvarthan, M.; Vimont, A.; Grenèche, J. M.; Serre, C.; Daturi, M.; Garcia, H. Comparison of Porous

- Iron Trimesates Basolite F300 and MIL-100(Fe) as Heterogeneous Catalysts for Lewis Acid and Oxidation Reactions: Roles of Structural Defects and Stability. *ACS Catal.* **2012**, 2 (10), 2060–2065.
- (21) Shahid, S.; Nijmeijer, K. High Pressure Gas Separation Performance of Mixed-Matrix Polymer Membranes Containing Mesoporous Fe(BTC). *J. Memb. Sci.* **2014**, 459, 33–44.
- (22) Yang, Y.; Bai, Y.; Zhao, F.; Yao, E.; Yi, J.; Xuan, C.; Chen, S. Effects of Metal Organic Framework Fe-BTC on the Thermal Decomposition of Ammonium Perchlorate. *RSC Adv.* **2016**, 6, 67308–67314.
- (23) Du, M.; Li, L.; Li, M.; Si, R. Adsorption Mechanism on Metal Organic Frameworks of Cu-BTC, Fe-BTC and ZIF-8 for CO₂ Capture Investigated by X-Ray Absorption Fine Structure. *RSC Adv.* **2016**, 6 (67), 62705–62716.
- (24) No Title <https://commons.wikimedia.org/wiki/File:CoFe2O4.png>.
- (25) Wang, D.; Hui, S.; Liu, C. Mass Loss and Evolved Gas Analysis in Thermal Decomposition of Solid Urea. *Fuel* **2017**, 207 (2), 268–273.
- (26) Wang, H.; Agmon, N. Complete Assignment of the Infrared Spectrum of the Gas-Phase Protonated Ammonia Dimer. *J. Phys. Chem. A* **2016**, 120 (19), 3117–3135.
- (27) Yang, Y.; Bai, Y.; Zhao, F.; Yao, E.; Yi, J.; Xuan, C.; Chen, S. Effects of Metal Organic Framework Fe-BTC on the Thermal Decomposition of Ammonium Perchlorate. *RSC Adv.* **2016**, 6 (71), 67308–67314.
- (28) Bukhtiyarova, M.; Lunkenbein, T.; Kähler, K.; Schlögl, R. Methanol Synthesis from Industrial CO₂ Sources: A Contribution to Chemical Energy Conversion. *Catal. Letters* **2017**, 147 (2), 416–427.

- (29) Gadzhiev, O. B.; Ignatov, S. K.; Gangopadhyay, S.; Masunov, A. E.; Petrov, A. I. Mechanism of Nitric Oxide Oxidation Reaction ($2\text{NO} + \text{O}_2 \rightarrow 2\text{NO}_2$) Revisited. *J. Chem. Theory Comput.* **2011**, 7 (7), 2021–2024.

Chapter 6 Conclusion and Significance

Iron is ubiquitous in nature and the presence of iron in the aquatic environment, mineral dust, rocks and soils emphasizes its involvement in various environmental processes. The chapters of this thesis highlight the chemistry of iron-containing materials and their role in three different environmental arenas such as aqueous geochemistry, heterogenous atmospheric chemistry and environmental catalysis and remediation.

The interactions of organic matter with metal oxide surfaces occurs through several mechanisms in aquatic environment. In this study, the interactions of low molecular weight organics that include citric acid, oxalic acid and pyrocatechol on hematite nanoparticles have been studied from *in situ* measurements (please see details in chapter 2). Spectroscopic data have been analyzed for the structure of surface complexes and binding strength using ATR-FTIR. ATR-FTIR absorption spectra of adsorbed citrate, oxalate, and pyrocatechol on hematite nanoparticles were collected after flowing 10^{-4} M solutions prepared in D₂O as a function of decreasing pD from 9 to 5. H/D exchange experiment spectral analyses revealed the existence of a higher degree of outer-sphere complexation for oxalate than citrate, which is dominated by inner-sphere monodentate complexes. In the case of pyrocatechol bidentate-binuclear complexes dominate. Moreover, experiments were performed for the adsorption kinetics of dimethylarsinic acid (DMA) and sodium arsenate with hematite nanoparticles pre-exposed to low molecular weight organics such as oxalate and pyrocatechol (please see details in chapter 3). These studies were conducted using ATR-FTIR with an emphasis on the role that electrolytes (KCl, NaCl, and KBr) play in the adsorption process. The results showed that the adsorption rates, obtained from the Langmuir adsorption kinetic model for model organics onto hematite surface were enhanced in the presence of electrolytes. The rate of adsorption for the arsenicals onto pre-exposed model organic hematite surface were greater in the presence of electrolytes. Experiments on the desorption of model organics from the surface of hematite

nanoparticles were also carried out to obtain initial rates of desorption using the Langmuir desorption kinetic model. These data reveal that arsenate is an effective desorbing agent for the model organics. The results obtained from these studies are significant and give a better understanding of how different functional groups (such as -OH and -COOH) affect the binding of organic matter onto iron oxide surface. Besides, the study highlights that *in situ* flow mode experiments can amplify trends otherwise missed in bulk batch adsorption experiments. Considering the ubiquity of organic–metal oxide interfaces in environment, mechanistic details at the molecular level are best elucidated from experimental procedures that mimic real systems and conditions. Moreover, kinetics and thermodynamic parameters obtained from these investigations will aid in the development of models to understand the transport and mobility of organics and other associated constituents (such as Fe, As) in soil and aquatic system.

In addition, the hygroscopic properties and chemical reactivity of SOA influence their overall contribution to the heterogenous atmospheric chemistry. In this study, the hygroscopic properties of organic and organometallic polymeric particles, namely polycatechol, polyguaiacol, Fe-polyfumarte, and Fe-polymuconate were investigated (please see details in Chapter 4). It has been found that these particles are efficiently formed in iron-catalyzed reactions with aromatic and aliphatic dicarboxylic acid compounds detected in field-collected SOA. The structure of surface water was studied using DRIFTS, and the uptake of gaseous water was quantified using QCM as a function of relative humidity. Spectroscopic data show that water bonding with organic functional groups acting as hydrogen bond acceptors causes shifts in their vibrational modes. Analysis of the hydroxyl group stretching region exhibited weak and strong hydrogen bonding networks that suggest cluster formation reflecting water-water and water-organics interactions, respectively. The results obtained from this study are significant because water plays a vital role in reactions with the pollutant gases. Moreover, the radiative balance of the atmosphere depends on the chemical composition, physical state (such

as solid or liquid) and the size of the particles. Besides, the results presented herein are important since global climate models need better parametrization of the hygroscopic properties and chemical reactivity of SOA.

On the chemistry of iron in heterogeneous remediation, iron-containing materials have been used as a catalyst in various systems. Here, Fe-BTC MOFs and CoFe_2O_4 nanomaterials have been studied as catalysts to explore their performance in reducing NO_x in NH_3 -SCR by DRIFTS (please see details in Chapter 5). From the spectroscopic data analysis, it was found that both Fe-BTC and CoFe_2O_4 contributed to the reduction of NO_x , in presence of urea, the source of *in situ* ammonia (NH_3) and experienced structural change in the surface functional groups. For both materials, gas phase products were observed at 180 °C. From the data analysis and kinetic studies, it was found that $\text{CoFe}_2\text{O}_4/8\%$ urea has the better rate for the conversion of $\text{NO}(\text{g})$, compared to Fe-BTC/8%urea. The proposed mechanism and kinetic study show that at 115 °C, no gas phase product is observed. However, increase of the temperature to 180 °C produced gases such as $\text{NH}_3(\text{g})$, $\text{HCNO}(\text{g})$ and $\text{CO}_2(\text{g})$. In addition, gas phase CH_3OH was observed for the decomposition of Fe-BTC only. The concentration of $\text{NH}_3(\text{g})$ after decomposition of $\text{CoFe}_2\text{O}_4/8\%$ urea, was much better than that of Fe-BTC/8%urea, that results in better conversion rate of $\text{NO}(\text{g})$ for CoFe_2O_4 compared to Fe-BTC. Even though, the surface area of Fe-BTC (771 m^2/g) is larger than that of CoFe_2O_4 (43 m^2/g). The results of these experiments are significant, as extensive studies are underway to develop NH_3 -SCR catalysts with high activity and stability in the low-temperature range, for the removal of NO_x from both flue and stationary sources. Introducing Fe-BTC metal-organic frameworks (MOFs) and CoFe_2O_4 nanomaterials to NH_3 -SCR as a catalyst is very significant in this regard.

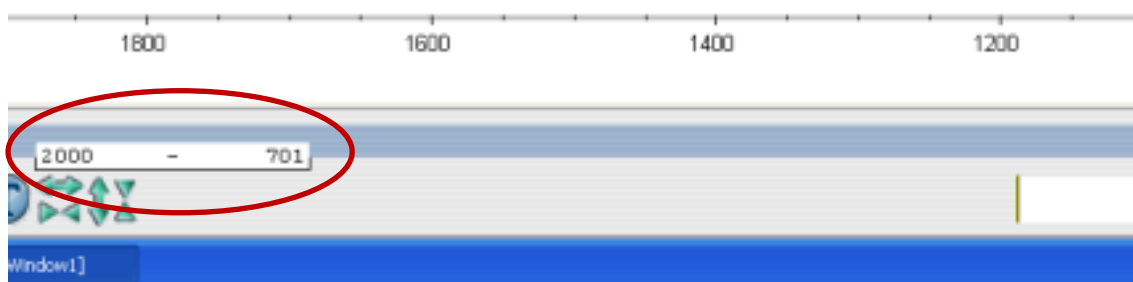
In brief, the main focuses of this thesis are to explore iron in understanding soil chemistry in the presence of organic matter, mineral dust chemistry, and designing environmental remediation technologies. Taking into account the intensive studies in these three branches of

environment, it can be concluded that the impact of this research in heterogeneous chemistry of iron at the liquid-solid and gas-solid interface will bridge the knowledge gaps in the chemistry of transition-metal in multicomponent atmospheric aerosol systems containing organic matter as well as remediating environmental pollutants.

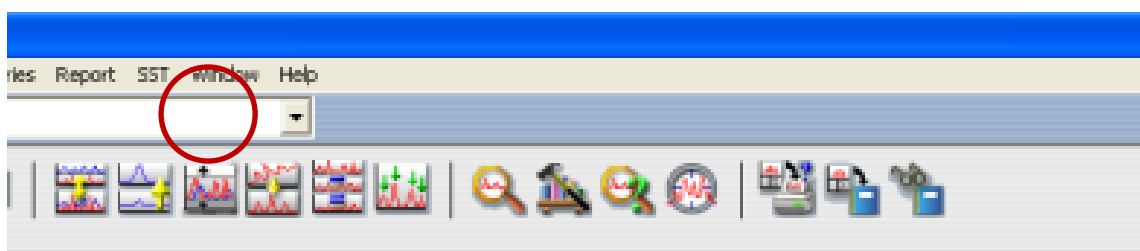
Appendix 1

Data analysis using Macros and OMNIC software

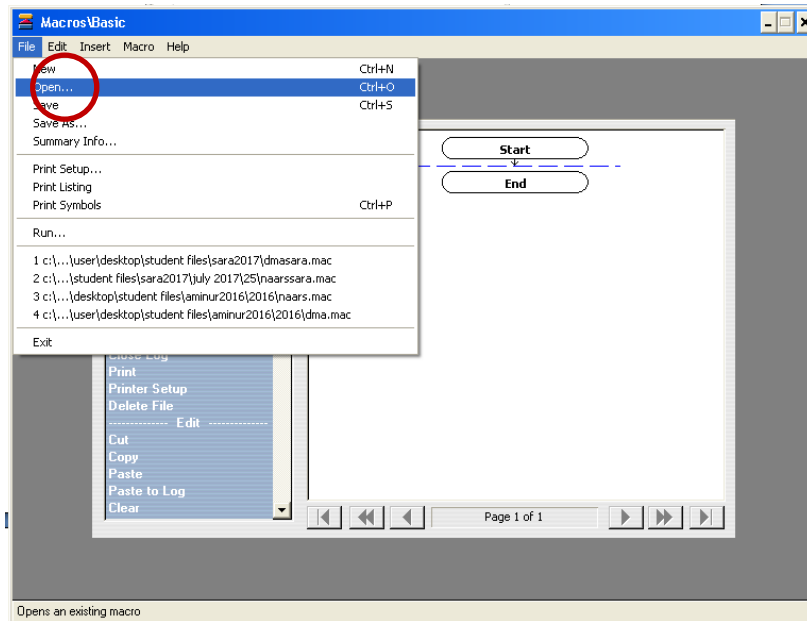
1. Open OMNIC
2. Zoom in the window by using the black bar at the right bottom of the screen to around 2000-700 cm^{-1} .



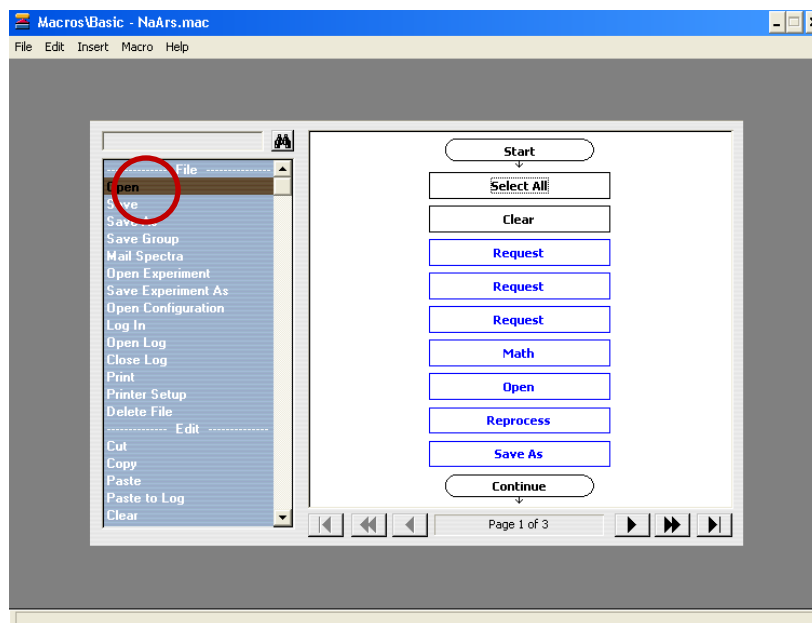
3. Press the full scale on the top of the window.



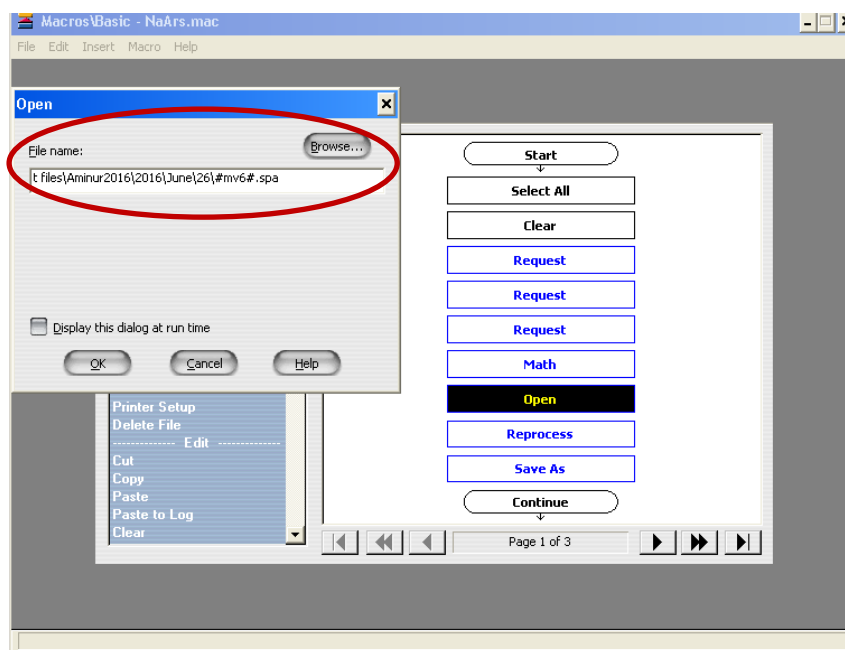
4. Open Macros window.



5. Go to the File and Open the drop-down menu.
6. Open the macros file that will be used to analyze target files. The screen will look like the following three pages which can be seen by using arrows at the bottom of windows.



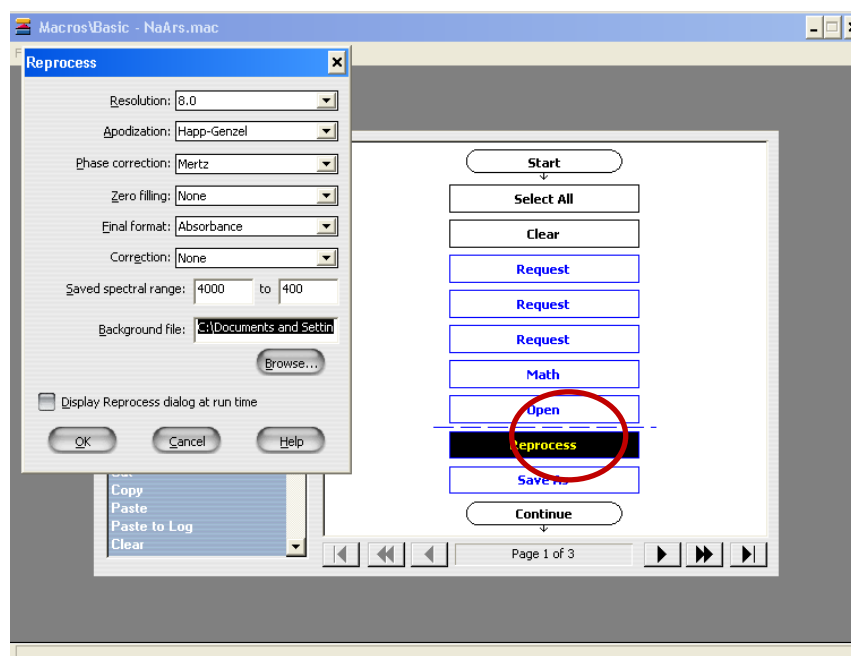
7. Double click to **open (Page 1)** the main window.
8. Change the “file name” to the location that has the single beam spectra followed by **\#mv6#.spa**



9. The link of the location of the folder can be found in the top left corner of the windows when the folder is opened.

10. Press ok to proceed.

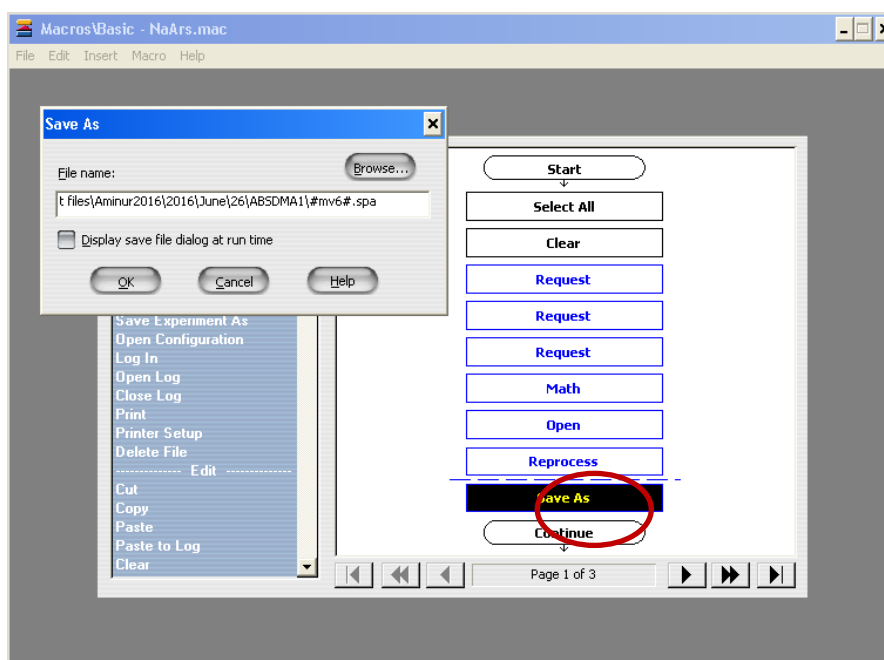
11. Double click the **“Reprocess”** (page 1) after open button.



12. Click browse to select the reference spectrum. The other setting should show up as displayed above.

13. Press ok to proceed.

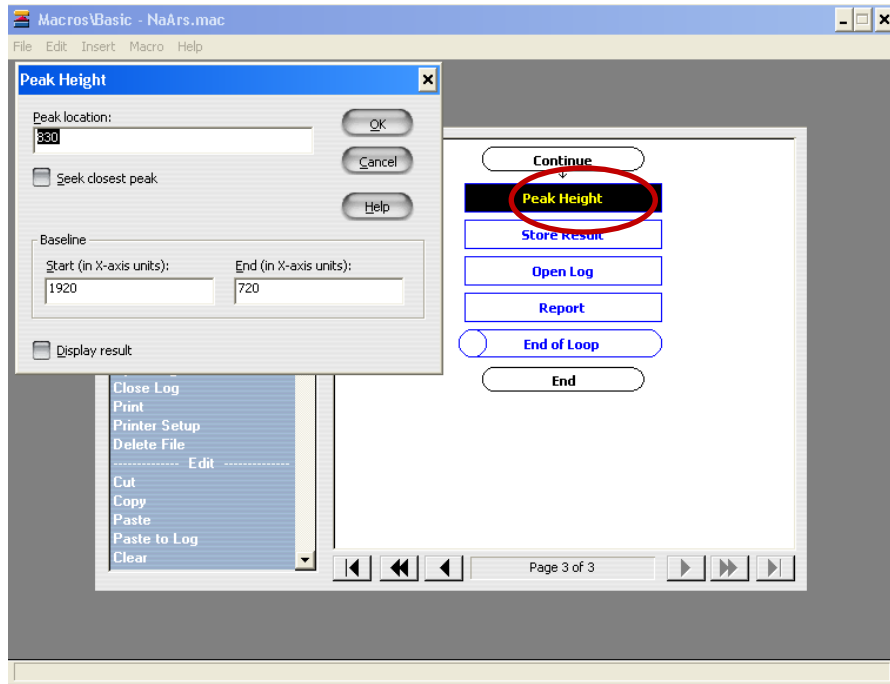
14. Then click on “Save as” (in page 1) to save the reprocessed spectra. Do the same thing for Save as in the main window and follow the location of the folder where the reprocessed spectra will be saved. (Make a folder by naming “ABS”. Make sure the file is empty.)



15. Press ok to proceed to page 2.

16. Repeat step 7-15 on page 2.

17. Proceed to page 3 and double click “Peak height”. Enter the base line and peak height.

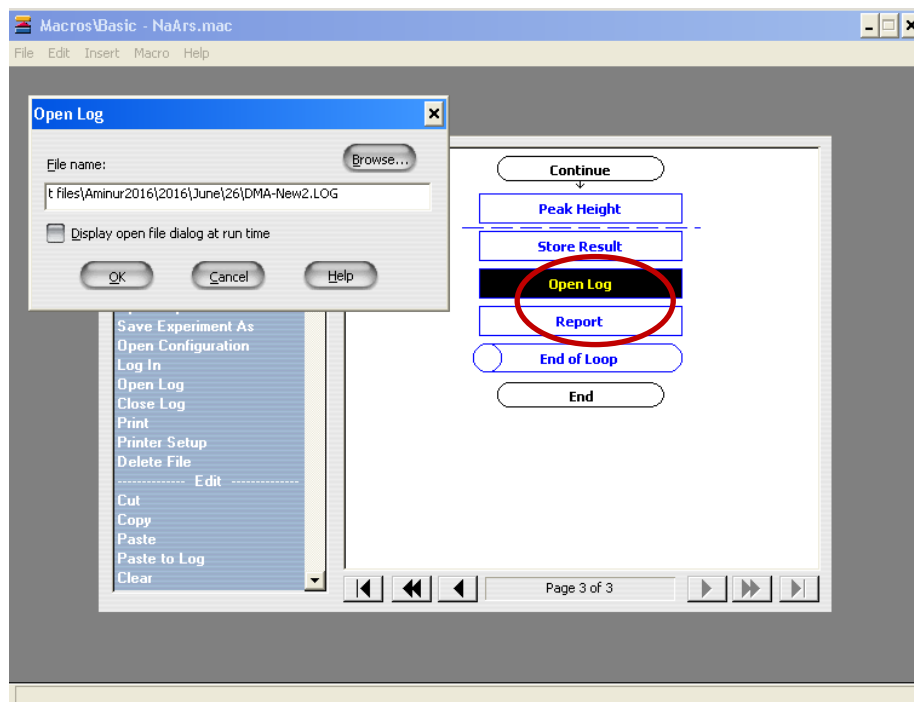


18. Then Press ok.

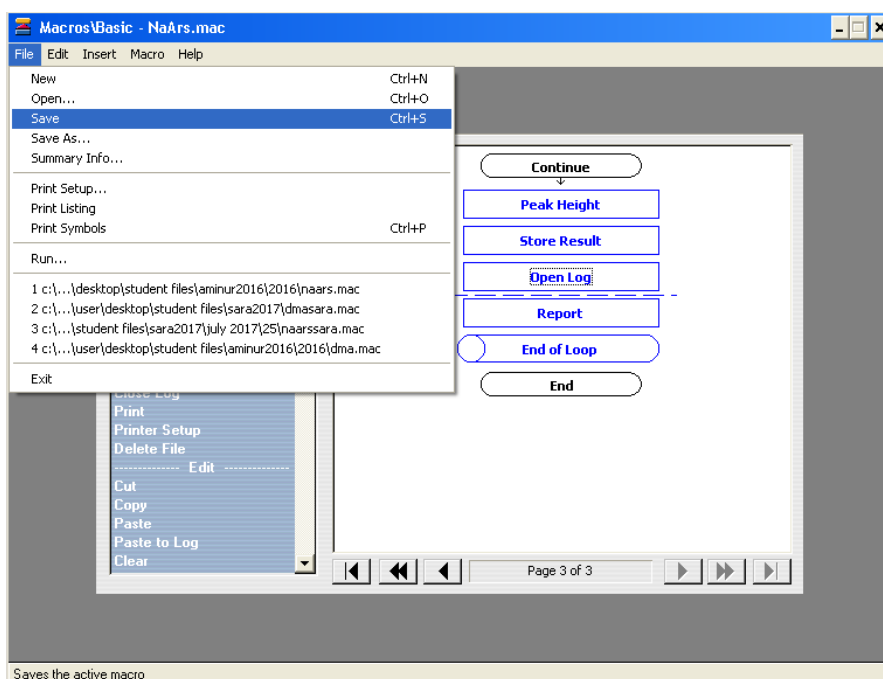
19. Double click “Open log”.

20. Edit the “File name” to the location where the log file will be saved. The last part as follows

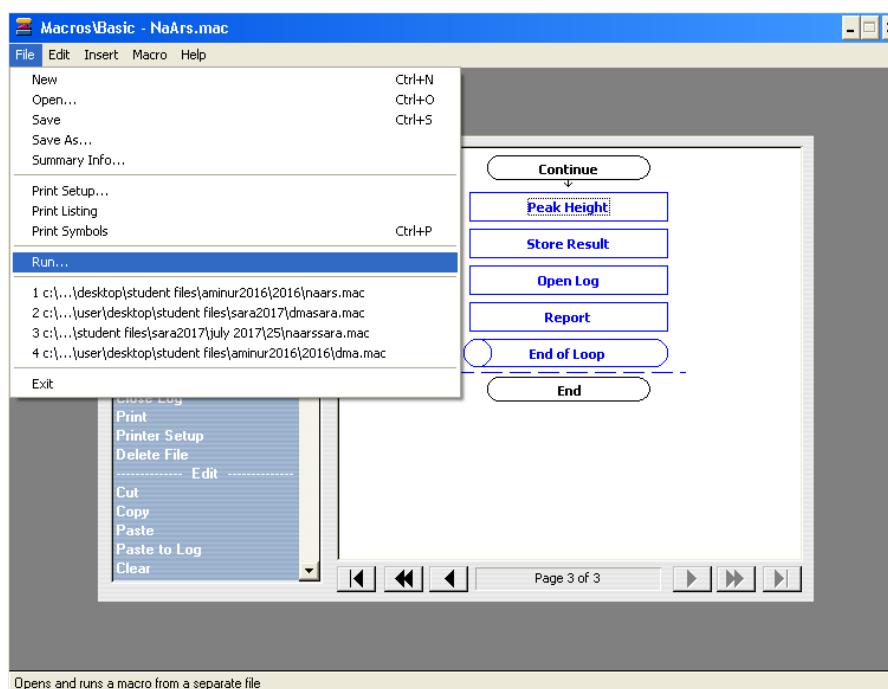
\file name.LOG



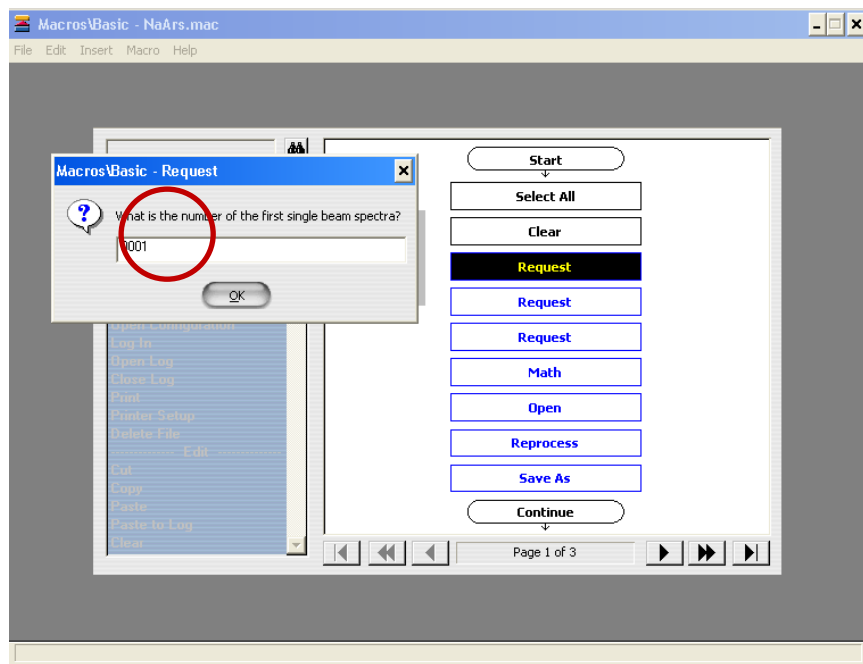
21. Go to **File** on the left corner of the windows and then **Save** in the drop-down menu.



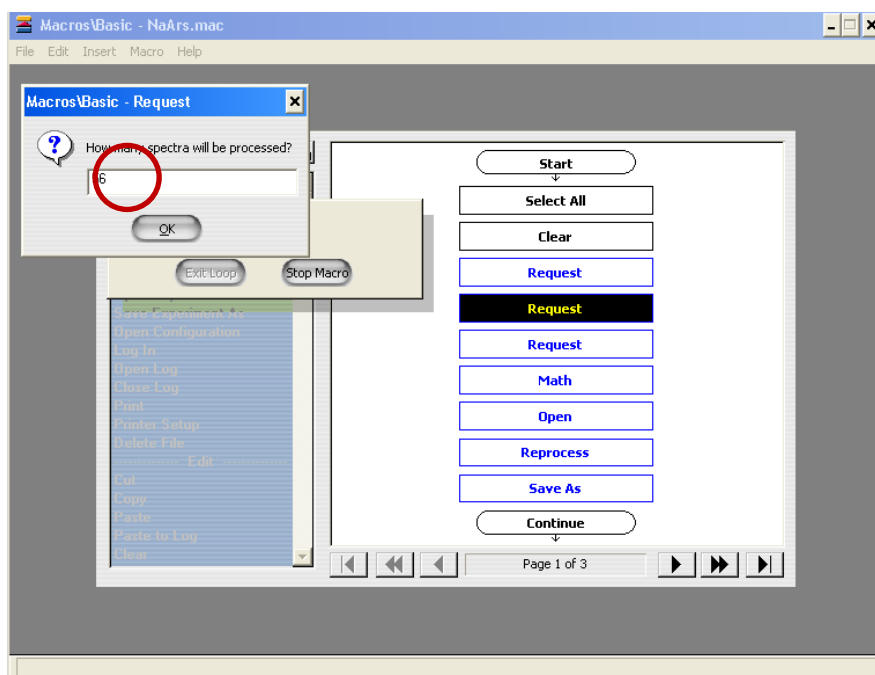
22. Again, go to **File** and then **Run** to the drop-down menu followed by the macros file that is used for analysis.



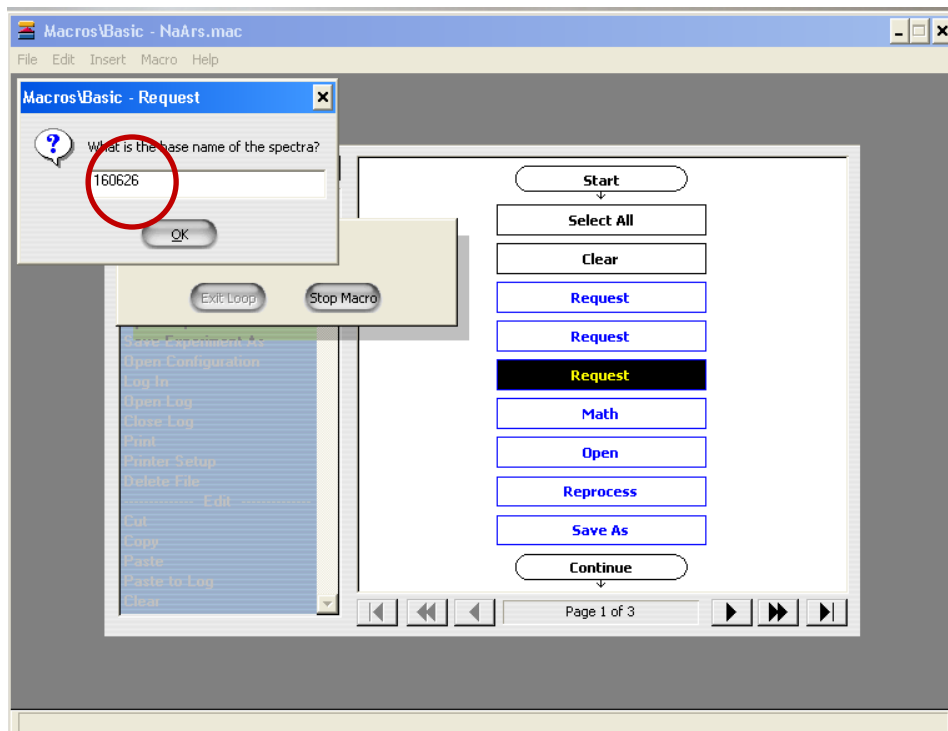
23. In the first pop up window enter **last 4 digits** of the single beam. (example: 0001)



24. In the second pop up window enter the number **two higher** than the number of spectra that are to be processed.



25. In the last pop up enter the **base number** of the spectra that are being processing (The number ahead of last four digit). Example **1606260001**. Here **160626** in the base number.



26. Macro will start running as soon as ok button is pressed.

27. After running macro close the OMNIC and Macro window to view log file where it was saved.

Appendix 2

Procedure for BET instrument

Step 1 Calibration of Cell with Rod

1. Turn on pump
2. Open the Nitrogen Gas cylinder by turning knob on pump
3. Calibration:
 - a. Monthly Calibration of Manifold
 - i. Select **Calibration Menu** on the Instrument
 - ii. Select **Manifold calibration**
 - iii. Select (4) – **Measure**
 - iv. When prompted:
 1. Enter V_{rod} as listed on calibration sheet and press **enter**
 2. Insert the cell with the spring without the rod into station **A** (right chamber) using the nut and screw to secure the cell. Then press **enter.**
 3. Remove the cell and insert the rod into the cell. Then re-insert the cell into station **A** and press **enter.**
 4. Manually record the **Measured Volume** after each repeat
 - v. Repeat Step iv. 5 times. After the 5th time, select **repeat** and then select option (2). When prompted, enter the average of the 3 middle volumes obtained.
 - b. Sample Cell Calculation (needs to be completed once)
 - i. Refer to the log to see if the cell/filling rod combination that will be used has been calibrated

- ii. Power on the machine and the vacuum while ensuring that the pressure of the nitrogen is at 10psi.
- iii. On the instrument select the calibration menu
- iv. Select sample cell calibration menu
- v. Select adsorbate (e.g. Nitrogen)
- vi. Select Calculate at run time (exception – if P_0 was calculated recently and is a known value)
- vii. When prompted, select which analysis station is the cell attached to.
- viii. Enter a cell number (be careful to NOT overwrite another cell number)
- ix. Select the type of cell that will be calibrated (e.g. 9mm for long cell with large bulb)
- x. Place the cell in the station that has been selected for calibration
- xi. Fill the Dewar ~2/3 with Liquid Nitrogen
- xii. Enter 600 sec for thermal equilibrium

Step 2: Evacuation/degassing of sample

1. Ensure that the vacuum is on and that the gas cylinder is at ~10psi
2. Press 3 on the BET instrument (Control Panel)
3. Press 2 on the BET instrument (Degas Station)
4. Press 1 on the BET instrument (Yes [load the degasser])
5. Press 1 on the BET instrument (Vacuum degas)
6. When prompted to, load cells into the degasser or plug degas stations with grey bolt.
7. Press any key on the BET instrument when completed
8. Wait sufficient time for water to be removed from the cell (~10min)
9. Press 2 on the BET instrument (Degas Station), then press 1 on the BET instrument (Yes [unload the degasser])

10. When prompted to, unload the degasser and cover the cells with parafilm. Remember to plug the degas station with the bolt.
11. Press any key on the BET instrument when completed
12. Obtain the mass of an empty cell and place the sample into the cells using the black funnel
13. Press 2 on the BET instrument (Degas Station)
14. Press 1 on the BET instrument (Yes [load the degasser])
15. Press 1 on the BET instrument (Vacuum)
16. When prompted to, load the degasser and then press any key on the BET instrument
17. Obtain the mass of the cell including the sample

Step 3: Begin analysis using BET instrument

1. Press 1 on the BET instrument (Analysis Menu) and then press 1 again (Run)
2. When prompted to, type in the user ID and hit enter
3. When prompted to, type in load analysis stations
4. Ensure the dewar is filled to the marker (2/3 full) with liquid nitrogen
5. Press 1 on the BET instrument (Continue) and then press 1 or 2 depending on the analysis station being used. Afterwards press enter
6. Type in number for the set up being used (see white binder for set ups) and press enter
7. Type in number of cell being used (see cell or white binder for cell specs) and press enter
8. Type in number of cell being used (see white binder) and press enter
9. Type in sample ID and press enter
10. Press 1 to add notes or press 2 for no notes
11. Enter the sample mass onto the BET instrument and press enter
12. Press 1 on the BET instrument to begin analysis.

Step 4: Open Novawin software

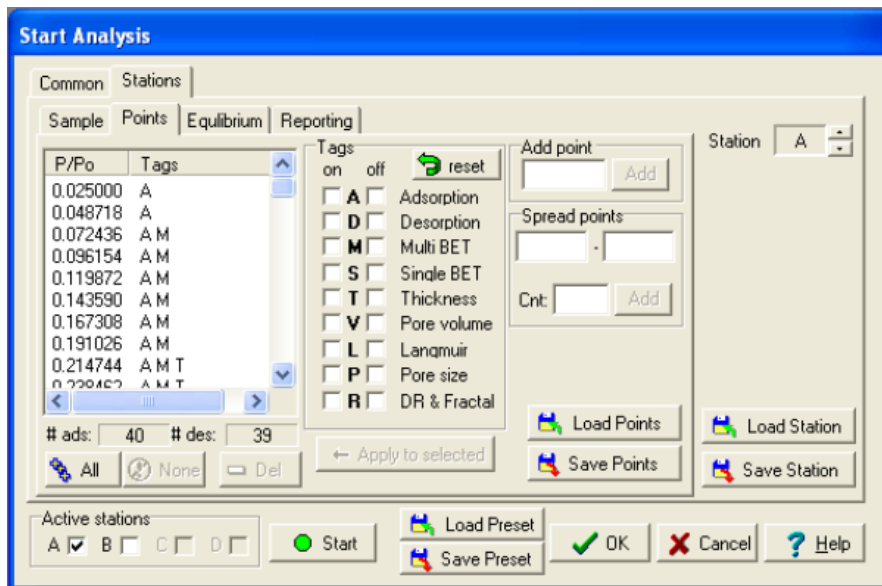
- a) Open Start analysis → Go to common bar as below and select as the following window. **If density of sample is known select calculate.**

The screenshot shows the 'Start Analysis' dialog box with the 'Common' tab selected. The 'Operator ID' is 'quantachrome' and 'Adsorbate Gas' is 'Nitrogen'. Under 'Sample Volume', the 'Calculate' radio button is selected, while 'Measure' is unselected. The 'Thermal delay (180-1200)' is set to 180 sec, and the 'Evacuation Cross-over Pressure' is 37.0 mmHg. In the 'P0 options' section, 'P0 mode' is 'Measure' and 'P0 Station' is 'A'. At the bottom, the 'Active stations' section shows 'A' checked, 'B' unchecked, 'C' unchecked, and 'D' unchecked. There are buttons for 'Start', 'Load Preset', 'Save Preset', 'OK', 'Cancel', and 'Help'.

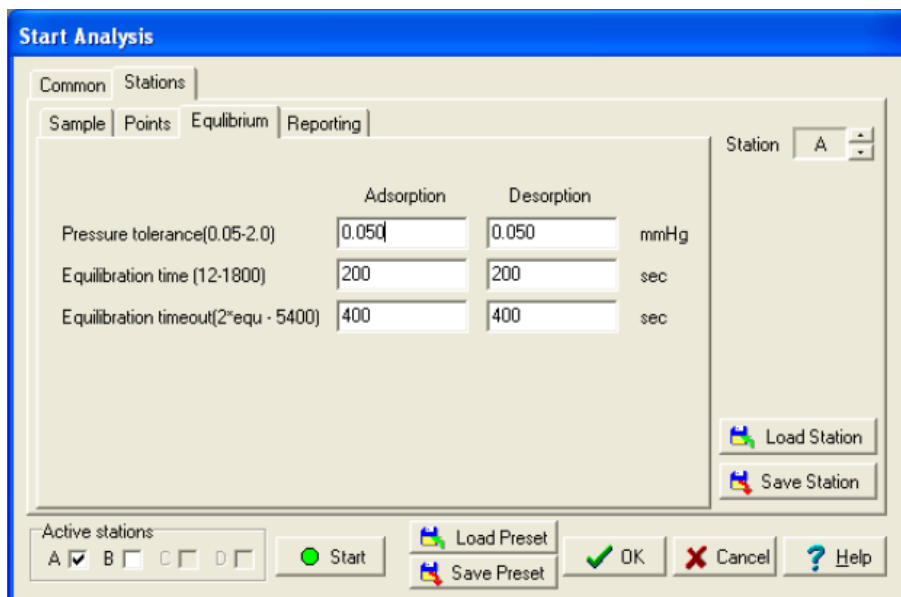
- Go to Stations → **Go to sample** as below window → Insert file name; Sample ID; Description, Weight; Density; Sample cell #; Station A or B

The screenshot shows the 'Start Analysis' dialog box with the 'Stations' tab selected. The 'Sample' sub-tab is active. The 'File Name' is 'Lab #_Aminur_Sample ID Fe-Fumarate_Date April 17th, 20'. The 'Sample ID' is 'Fe Fumarate', the 'Description' is 'With cell without bulb', the 'Weight' is 0.04000 g, and the 'Density' is 0.26000 g/mL. The 'Sample cell' is set to '4' and the 'Station' is 'A'. There are buttons for 'Load Station' and 'Save Station'. At the bottom, the 'Active stations' section shows 'A' checked, 'B' unchecked, 'C' unchecked, and 'D' unchecked. There are buttons for 'Start', 'Load Preset', 'Save Preset', 'OK', 'Cancel', and 'Help'.

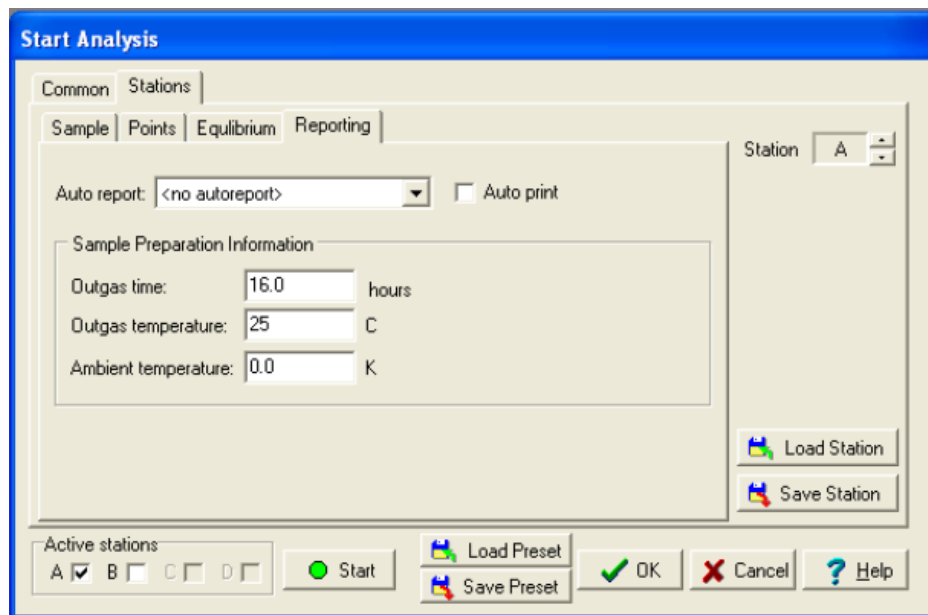
- b) **Go to points** → Insert point by **Add point** and select Tags as required (A for adsorption; D for desorption, etc)



c) **Go to Equilibrium**→ Fill up the Pressure tolerance; Equilibrium time; and Equilibrium timeout as below



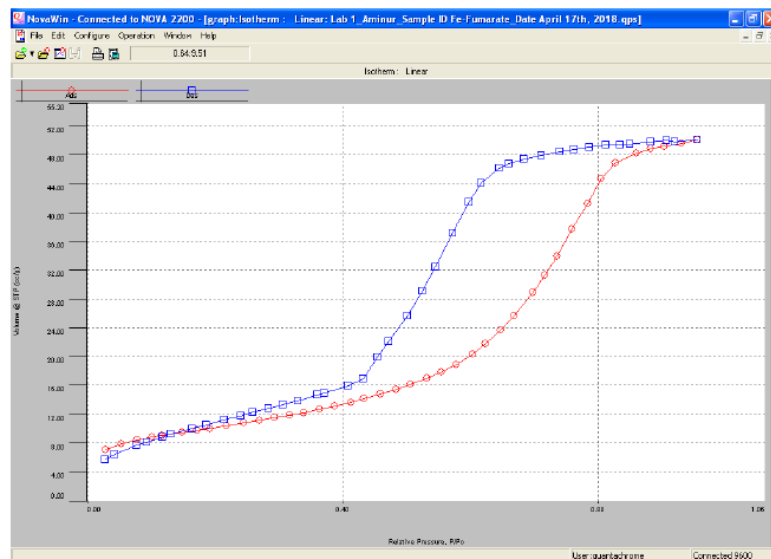
d) **Go to Reporting**→ Fill up outgas time; Outgas temperature; and ambient temperature



Then press **start** bar below the window.

Data Analysis:

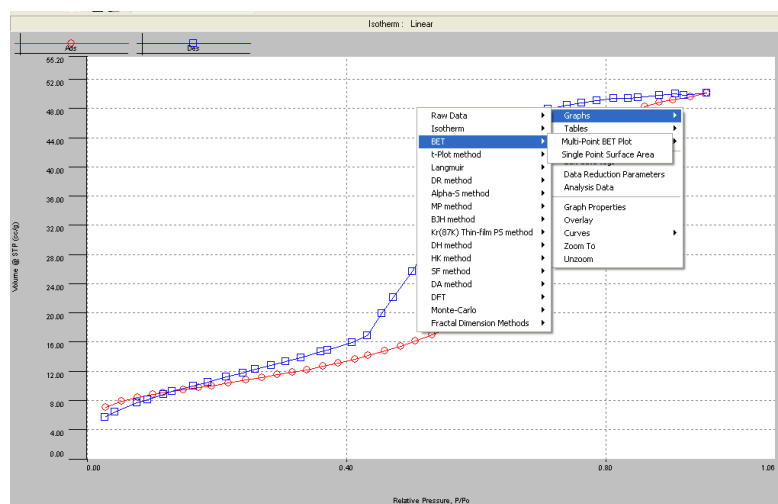
Below an example of Full adsorption (40 points) and desorption (39 points) isotherm data:



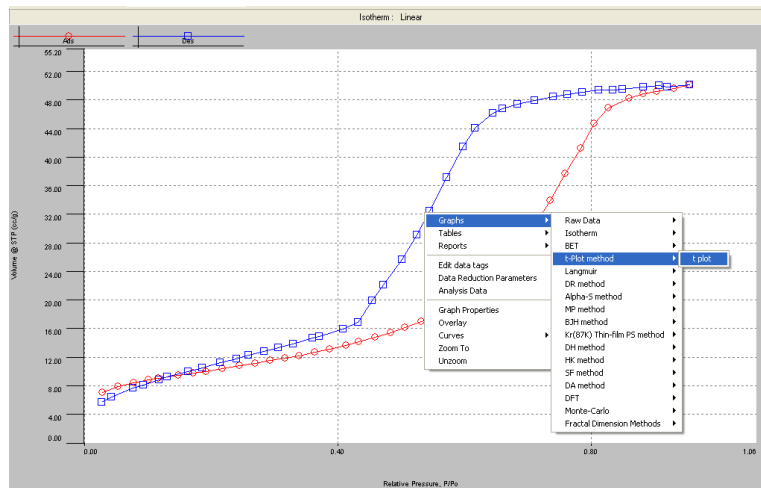
Analysis for BET (Multi and Single), V-t, BJH, DH, HK, DA methods:

Right click on the mouse on the points of adsorption curve. A window will appear with Graphs on top. Then follow the arrow that will bring another window with Raw data on top → Then click on any of the method that needs to be analysis as the following window:

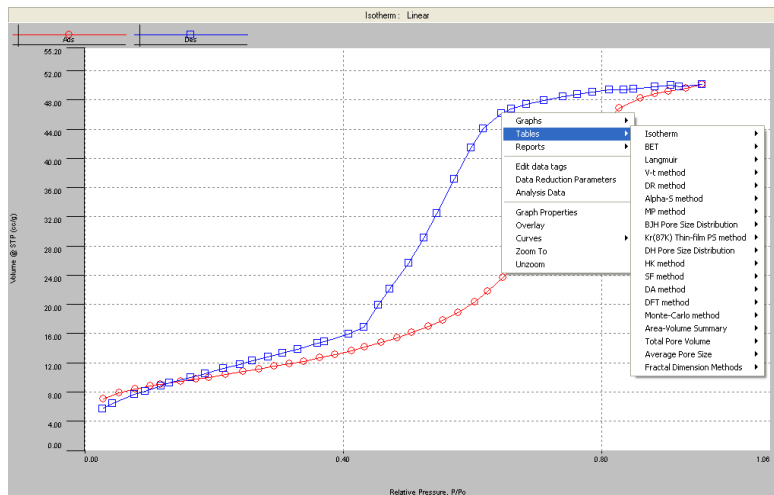
- i) For multi BET analysis



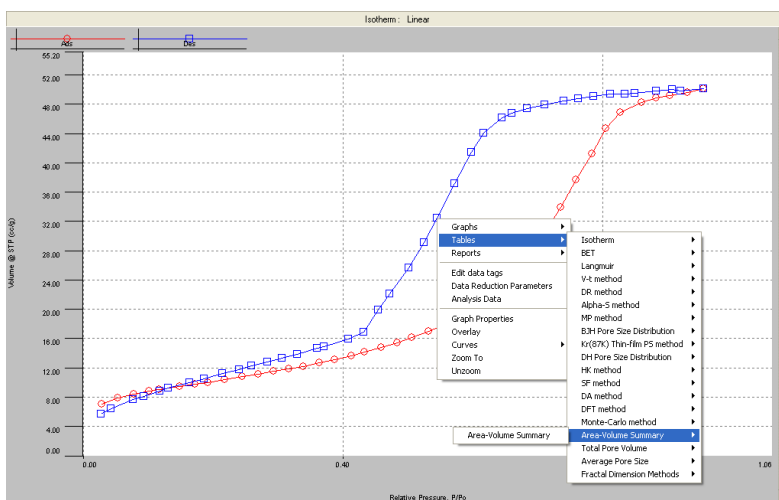
ii) v-t method analysis



iii) Table for the points analyzed for any analysis



iv) Table for the summary of all methods



Additional Important Information

Determination of Sample Cell

Stem diameter – choose the narrowest diameter that comfortably admits the sample

- Cohesive powders may be analyzed in larger stems to aid in cleaning.

Sample amount/bulb size – always choose smallest possible but full adsorption/desorption isotherms should have at least 15-20mm in the cell.

Placing Sample in the cell:

1. Determine what cell should be used for sample (smaller diameter the better). If there is a high risk of *elutriation* (see below), then use a cell with a bulb. No amount of sample can remain on the side of the cell during the degas or analysis.
2. Place the black cell funnel over the cell and carefully pour the sample into the cell
3. Using a spatula lightly tap on the cell to remove any powder from the cell walls. If this does not remove the powder a static gun may be used. If a static gun is not available a pipe cleaner may be used to physically push the sample to the base of the cell.

Elutriation:

- Loss of sample from the sample cell which is caused by the rapid flow of gas out of the cell
- Wider stems and bulbs reduce this
- Filler rods worsen the problem
- Both degas and analysis stations have a filter to prevent any sample from entering the manifold
- If this is still a problem after taking the above into account, insert a small glass wool plug into the cell stem between two halves of the filler rod. This is the ONLY time when a filler rod may be in the degas station.

Heating the Cell: The amount of heat that is required for the sample depends on the identity of the sample and its ability to tolerate heat without disrupting the samples structure. Heating must be done carefully so that water is safely removed from the sample.

Example: fumed silica heated to 300°C

- Remove the grey plug from the degas station
- Set the thermostat to 40°C but do not turn on heating mantle
- Push 3 – control panel menu
- Push 2 – degas station
- Degas the sample (WITHOUT ROD) until a good vacuum is established
- Turn on the heating station
- Wait until the temperature reaches 40°C and hold for 15min
- Increase the thermostat to 80°C, once the temperature reaches this point wait 15 min then increase to 120°C, again wait until the sample reaches this temperature hold for 15 min, and finally set the thermostat to its final temperature of 300°C and leave the sample for 3 hours.
- Return the grey plug to the degas station

To weigh sample:

1. Place sample in the cell
2. Place the cell into the degas station and degas the cell.
3. Backfill the cell with nitrogen and remove the cell from the degas station.
4. Place parafilm/septum cap over the mouth of the cell and weight the cell to the 4th decimal place (e.g. 0.0001g)
5. Remove the parafilm and replace the cell into the degas station
6. Heat the cell as needed
7. Allow the cell to cool and remove the cell from the degas station

8. Replace the parafilm/septum cap and reweight the sample

Equation for mass:

$$m_{\text{sample}} = m_{\text{cell with nitrogen}} - m_{\text{heated cell}}$$

Appendix 3

EPA, United State Environmental Protection Agency data base

Figure 6.1 shows the absorbance spectra NO, NO₂, N₂O, NH₃ and HNCO. The spectra were taken from the spectral data base of EPA, United State Environmental Protection Agency website. Transmission spectra were calculated using the HITRAN96 spectral database and a modified version of the Fast Atmospheric Spectral Code (FASCODE). These transmission spectra were degraded using triangle apodization and converted to absorbance (base 10). Pressure was set to 760 mm Hg (1 Atmosphere). These results are calculated spectra based on fundamental molecular parameters typically measured by high resolution spectroscopic techniques.²¹

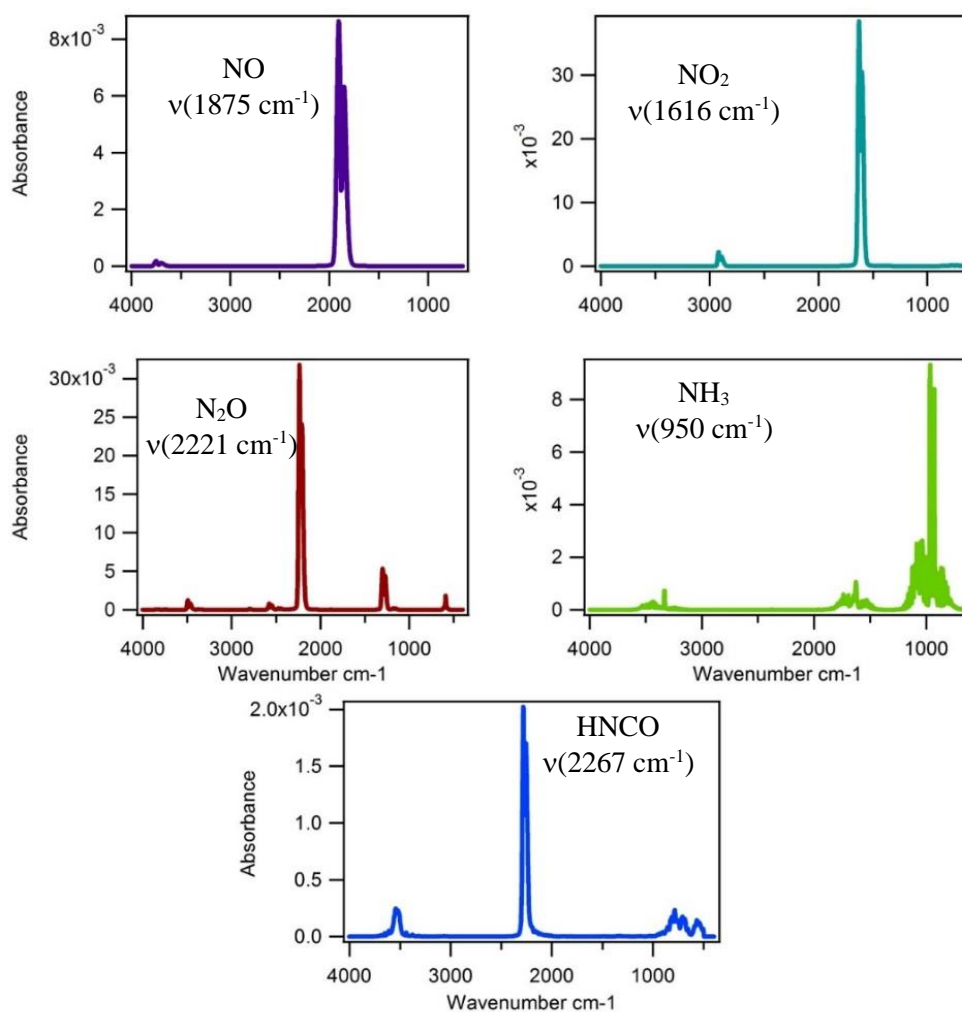


Figure 6.1

Using the peak area or peak height of each species, molar absorptivity (ϵ) $\text{ppm}^{-1}\text{cm}^{-2}$ was calculated by applying Beer's law (Table 1.2). These epsilon values were applied to quantify the concentration of each gas produced in our experiments.

Table 6.1: Molar absorptivity obtained for NO, NO₂, N₂O, NH₃ and HNCO from EPA database.

Peak area/height	Integrated peak area/Height concentration (ppm⁻¹-meter⁻¹)	Integrated peak area/Height concentration (ppm⁻¹-cm⁻¹)	Molar Absorptivity ϵ(ppm⁻¹cm⁻²)
Peak area of NO (1969-1772 cm ⁻¹) 0.66599	150	1.50 x 10 ⁴	4.44 x 10 ⁻⁵
Peak area of NO ₂ (1670-1542 cm ⁻¹) 1.7310	30	3.00 x 10 ³	5.77 x 10 ⁻⁴
Peak area of N ₂ O (1670-1542 cm ⁻¹) 1.3958	25	2.50 x 10 ³	5.58 x 10 ⁻⁴
Peak height of NH ₃ at 965 cm ⁻¹ (980-915 cm ⁻¹) 0.00907	22.5	2.25 x 10 ³	4.03 x 10 ⁻⁶
Peak height of HNCO at 2283 cm ⁻¹ (2395-2200 cm ⁻¹) 0.00202	1	1.00 x 10 ²	2.02 x 10 ⁻⁵